12

MRDC41007.24FR

TEMPERATURE COMPENSATED PIEZOELECTRIC MATERIALS

Final Report
For Period 5/15/78 through 5/14/82

September 1982

ARPA Order No.	3570
Program Code:	8D10
Name of Contractor:	Rockwell International Corporation
Effective Date of Contract:	May 15, 1978
Contract Expiration Date:	May 14, 1982
Amount of Contract Dollars:	$944,318
Contract Number:	F49620-78-C-0093
Principal Investigators:	Dr. R.R. Neurgaonkar
	(805) 498-4545, ext. 109
	Dr. L.E. Cross
	Pennsylvania State University
	(814) 865-1181

Sponsored by
Advanced Research Projects Agency (DoD)
ARPA Order No. 3570
Monitored by AFOSR Under Contract No. F49620-78-C-0093

UNCLASSIFIED

SECURITY CLASSIFICATION OF THIS PAGE (When Data Entered)

REPORT DOCUMENTATION PAGE

READ INSTRUCTIONS BEFORE COMPLETING FORM

1. REPORT NUMBER: AFOSR-TR- 82-1069	2. GOVT ACCESSION NO.: AD-A123 400
3. RECIPIENT'S CATALOG NUMBER:	
4. TITLE (and Subtitle): TEMPERATURE COMPENSATED PIEZOELECTRIC MATERIALS	5. TYPE OF REPORT & PERIOD COVERED: Final Technical Report 05/15/78 through 05/15/82
	6. PERFORMING ORG. REPORT NUMBER: MRDC41007.24FR
7. AUTHOR(s): R.R. Neurgaonkar	8. CONTRACT OR GRANT NUMBER(s): F49620-78-C-0093
9. PERFORMING ORGANIZATION NAME AND ADDRESS: Rockwell International, Microelectronics Research and Development Center, 1049 Camino Dos Rios, Thousand Oaks, CA 91360	10. PROGRAM ELEMENT, PROJECT, TASK AREA & WORK UNIT NUMBERS: ARPA Order No. 3570
11. CONTROLLING OFFICE NAME AND ADDRESS: Air Force Office of Scientific Research, Bolling Air Force Base, Washington, D.C. 20332	12. REPORT DATE: September 1982 13. NUMBER OF PAGES: 100
14. MONITORING AGENCY NAME & ADDRESS (if different from Controlling Office)	15. SECURITY CLASS. (of this report): Unclassified 15a. DECLASSIFICATION/DOWNGRADING SCHEDULE

16. DISTRIBUTION STATEMENT (of this Report)

Approved for public release; distribution unlimited.

17. DISTRIBUTION STATEMENT (of the abstract entered in Block 20, if different from Report)

18. SUPPLEMENTARY NOTES

19. KEY WORDS (Continue on reverse side if necessary and identify by block number)

Tungsten bronze ferroelectrics
Lead barium niobate
SAW temperature compensation
Strontium barium niobate
Liquid phase epitaxy
Czochralski growth technique
Gibb's energy functions
Phenomenological model
Elastic compliances

20. ABSTRACT (Continue on reverse side if necessary and identify by block number)

A full phenomenological model has been developed to predict the dielectric, piezoelectric and elastic compliances and their temperature behavior for bronze structure ferroelectrics. The model is based on an extension of the Landau-Ginsburg Devonshire phenomenology which includes the diffuse nature of the curie transition at T_C. Sixth rank electrostrictive coupling terms have been found necessary to adequately describe the paraelectric phase above the curie temperature; these terms do not appear to change markedly with cation substitution.

DD FORM 1 JAN 73 1473 EDITION OF 1 NOV 65 IS OBSOLETE

UNCLASSIFIED

SECURITY CLASSIFICATION OF THIS PAGE (When Data Entered)

High quality, 1 inch diameter SBN:60 single crystals have beer successfully grown by the Czochralski technique, and this material is currently being evaluated by several laboratories for a varicty of electro-optic, non-linear optic, millimeter wave and SAW device applications. SAW measurements on SBN:60 show that this bronze composition possesses temperature compensated orientations with results which are comparable to PKN. High quality, thin film growth of $Sr_{0.5}Ba_{0.5}Nb_2O_6$ and $Sr_2KNb_5O_{15}$ has also been demonstrated using liquid phase epitaxial (LPE) growth on a variety of orientations of SBN:60 single crystal substrates. These successful demonstrations of tungsten bronze LPE growth open up the future development of other lattice matched bronze compositions for a variety of applications in cases where large single crystal growth is not possible.

The small value of the piezoelectric coefficient d_{15} in SBN:60 crystal has been attributed in the phenomenological model to the low transverse curie temperature θ_1. Improved coupling should be found for the stuffed bronze $Ba_{2-x}Sr_xK_{1-y}Na_yNb_5O_{15}$ and tetragonal $Pb_{1-x}Ba_xNb_2O_6$, and thermodynamic analysis shows that temperature compensated SAW device orientations should be possible for $Pb_{1-x}Ba_xNb_2O_6$ compositions near the morphotropic phase boundary ($x \sim 0.4$). Good quality, medium size single crystals of PBN and BSKNN have been grown, and initial characterization of these materials show them to be very promising for continued SAW device development as well as other piezoelectric and electro-optic applications. Work is also presented on the materials development and dielectric behavior of modified PBN, $Pb_{1-2x}K_xM_xNb_2O_6$, M = La or Bi.

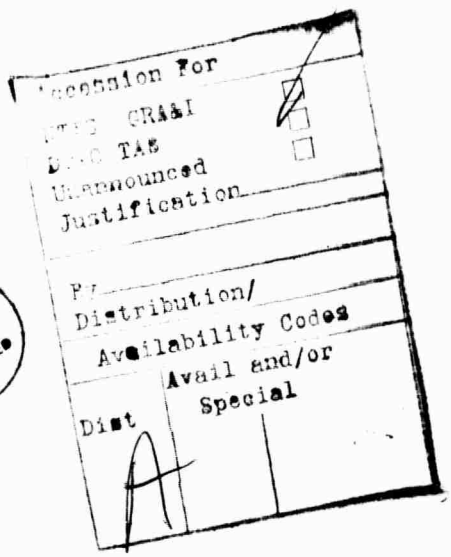

TABLE OF CONTENTS

LIST OF FIGURES

LIST OF FIGURES

LIST OF FIGURES

LIST OF TABLES

LIST OF TABLES

1.0 PROGRESS AND TECHNICAL SUMMARY

We have continued our work on the phenomenological model for the bronze $Sr_{0.6}Ba_{0.4}Nb_2O_6$ and the thermodynamic calculations for this composition have verified the applicability of this method. This work has now been extended to the tetragonal $Pb_{1-x}Ba_xNb_2O_6$ composition and to the stuffed bronze $Ba_{2-x}Sr_xK_{1-y}Na_yNb_5O_{15}$.

The objective of the modelling studies was to develop the capability to predict the dielectric, piezoelectric and elastic compliances and their temperature behavior for a wide range of bronze structure ferroelectrics. The method chosen was an extension of the Landau:Ginsburg:Devonshire phenomenology which permits the full three dimensional description of the ferroelectric single domain properties in terms of a limited family of tensor coefficients of the prototypic paraelectric high temperature phase.

The following major advances towards this ambitious goal have been accomplished over the duration of the present contract:

1) Using $(Sr_{0.61}Ba_{0.39})Nb_2O_6$ crystals as a model material with convenient low Curie temperature T_c, we were able to demonstrate unequivocally that

   a) The conventional Devonshire equations gave a precise description of the polarization P_s, the piezoelectric coefficients d_{ij} and the thermal lattice distortion α_{ij}, provided the diffuse nature of the Curie transition at T_c was taken into account by a gaussian distribution of the Curie temperature θ_3.

   b) To mod the elastic compliances it was necesasry to include higher order electrostriction constants Φ_{ijklmn} of sixth rank, leading to stiffened compliances of the form

$$s^{P}_{ijkl(P_3)} = s^{P}_{ijkl(0)} + \Phi_{33ijkl}P_3^2 \quad .$$

This equation was verified by inducing the polarization P_3 above T_c and measuring directly the shift of the stiffened s constant using resonance methods. It was confirmed that for this tetragonal bronze, the sign of Φ_{32323} is such as to lead to a stiffening of s_{44} by the temperature decay of the spontaneou polarization $P_{3(s)}$. This diagonal term in the elastic compliance matrix, together with the thermal contraction along the P_3 axis, ensures that an orientation (cut) of the crystal with temperature compensated round-trip delay is possible.

2) The piezoelectric constant values in the SBN bronze are very high for d_{33}, but low and uncomfortably small for d_{15}. The low value of this constant may be traced in the phenomenology to the very low value of the transverse Curie temperature θ_1 in this composition.

3) To improve the piezoelectric coupling it is necesary to move in the composition field of the tetragonal bronzes towards compositions with higher θ_1 values. Partial elevation of θ_1 is possible in the stuffed bronze structures in the sodium potassium substituted barium strontium bronzes, and these crystals have been grown and will be of interest for some applications.

4) A crossover between θ_1 and θ_3 is found to occur in the $Pb_{1-x}Ba_xNb_2O_6$ family, for compositions in the vicinity x = 0.4. At the $Pb_{0.6}Ba_{0.4}Nb_2O_6$ composition a morphotropic phase boundary separates tetragonal and orthorhombric ferroelectric forms.

5) The thermodynamic analysis predicts that temperature compensated cuts with very high piezoelectric coupling should be possible in the tetragonal $Pb_{1-x}Ba_xNb_2O_6$ compositions close to morphotropy,

but we have been unable to grow large enough crystals to confirm this prediction within the time frame of the contract.

It may be noted that the thermodynamic method has for the first time made it possible to predict in a semi-quantitative manner the temperature dependence of property tensors for a system where the structure is much too complicated to permit atomistic calculations. It will be important to extend these studies to other parameters such as the electro-optic r_{ijk} and g_{ijkl} constants and to confirm more fully the manner in which the prototypic constants mutate with major cation substitutions.

The growth of large diameter (1 inch) high quality SBN:60 single crystals has been successfully demonstrated, and samples of this material have been supplied to a large number of laboratories for evaluation in a variety of electro-optic, piezoelectric, acoustic and millimeter wave applications. This material has been found to have piezoelectric and electro-optic properties which are superior to any known material, and is optically superior to either $LiNbO_3$ or $LiTaO_3$.

Several compositions of the $Pb_{1-x}Ba_xNb_2O_6$ tungsten bronze have been grown by the Czochralski method and have been evaluated for their dielectric and piezoelectric properties. Electrical data for the single domain crystals confirm tht the permittivity K_1 and the piezoelectric constant d_{15} can be strongly enhanced in compositions close to the morphotropic phase boundary in the region of the $Pb_{0.6}Ba_{0.4}Nb_2O_6$ composition. Good quality, medium size single crystals of the stuffed bronze $Ba_{1.2}Sr_{0.8}K_{0.75}Na_{0.25}Nb_5O_{15}$ have also been grown, and the higher curie temperature (203°C) and good electromechanical coupling coefficients k_{15} and k_{33} indicate that this material is very promising for future SAW device and other applications.

The $Sr_{0.5}Ba_{0.5}Nb_2O_6$ and $Sr_2KNb_5O_{15}$ tungsten bronze films have been successfully grown onto $Sr_{0.6}Ba_{0.4}Nb_2O_6$-substrates by the liquid phase epitaxial (LPE) technique from BaV_2O_6 and KVO_3 solvents, respectively. The growth of these bronze compositions was studied on different crystallographically-

oriented SBN substrates and it has been shown that the growth is much faster on the (001)-plate. The quality of the films is reasonably good, and films as thick as 20-60 μm have been successfully developed for acoustical and electro-optical characterization. The hetero-epitaxial growth of $Sr_2KNb_5O_{15}$ on the SBN:60 substrate has been reported for the first time and this opens a new interest in this family for its application in a variety of areas including SAW, electro-optic, acousto-optic and non-linear optics.

For the ferroelectric films, it is important that the films be poled before they are used for characterization; this task has been accomplished successfully and we do not consider poling to be a major problem in the present work. The piezoelectric coefficients, d_{33}, d_{15}, e_{33}, and e_{15}, and the electromechanical coupling coefficients k_{33} and k_{15}, which are important in the present study, have been evaluated.

2.0 REQUESTS FOR SBN CRYSTALS

During the past four years, we have been actively involved in the growth and characterization of $Sr_{1-x}Ba_xNb_2O_6$ (SBN) single crystals grown by the Czochralski method. We have now demonstrated the ability to grow large diameter (1 inch) $Sr_{0.60}Ba_{0.40}Nb_2O_6$ (SBN:60) single crystals which show good electrical, mechanical, and optical quality for potential use in a wide variety of applications. Several examples of these crystals can be seen in Fig. 1. The SNB:60 tungsten bronze composition has been shown to have very high electro-optic and pyroelectric coefficients, higher than for any other known single crystal material. Optical evaluation at several laboratories have shown that SBN:60 single crystals have optical properties superior to those for either $LiNbO_3$ or $LiTaO_3$, although situations have been somewhat of a problem in the present crystals. Efforts are currently underway to minimize this problem through the use of higher purity starting materials and the installation of a new Czochralski crystal puller which features automatic diameter control and improved control over temperature gradients.

SBN, as well as other tungsten bronze family crystals, has shown potential for use in a wide variety of electro-optic, piezoelectric, and surface acoustic wave applications. A list of the applications which are currently being investigated is given in Table 1. Single crystal SBN:60 has shown promising results in many of these applications areas,[1-4] either by itself, or used as a host substrate for lattice-matched SBN and other tungsten bronze compositions. The work by the present investigators on the growth and characterization of high quality, large diameter SBN crystals has led to an ever increasing number of requests for this mateial over the past 2-3 years. A list of the agencies and organizations who have requested SBN single crystals from Rockwell International up to this time is found in Table 2. Table 3 lists the various applications of SBN by these requesting organizations showing the wide variety of interest in this material. Specific military applications of the tungsten bronze family of materials, including SBN, are given in Table 4 along with the

MRDC82-19260

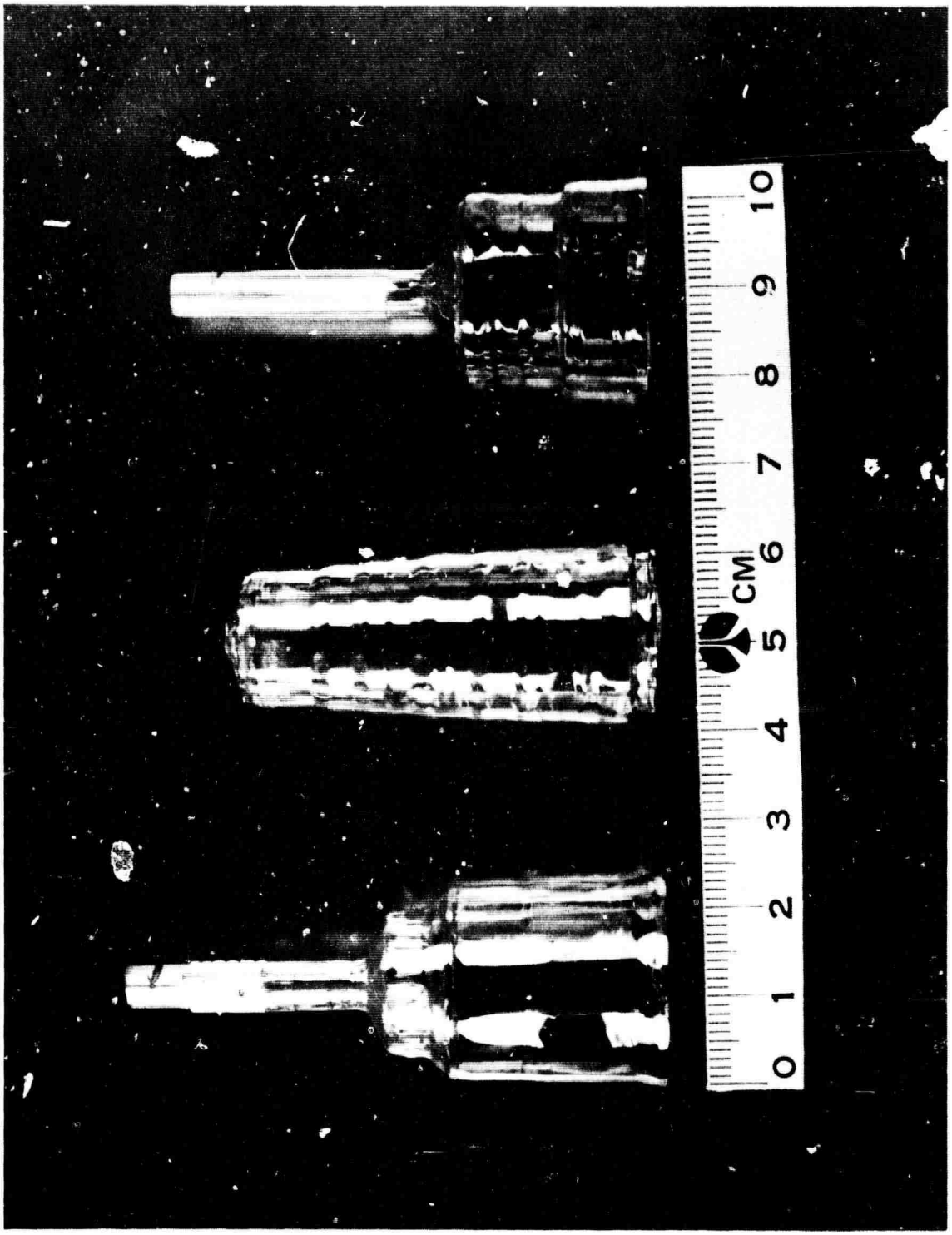

Fig. 1 SBN:60 single crystals.

Table 1

Tungsten Bronze Family Crystals for Optoelectronic Device Applications

Pyroelectric Applications:	Detectors, remote sensing, lasers: UV and IR, laser fusion, particle detection, etc.
Electro-optics Applications:	Modulators, filters, switches, beam deflectors, etc., for communication and signal processing
Mi.limeter Wave Applications:	Phase shifter, modulators, switches for radar sensing and communications
Bulk Piezoelectric Applications:	Underwater hydrophones, transducers, switches, etc.
Surface A.)ustic Wave Applications:	Filters, detectors, oscillators, etc.

Table 2

Requests for Tungsten Bronze SBN Single Crystals

Pyroelectric Device Applications	Electro-Optic Device Applications	Millimeter-Wave Device Applications	Piezoelectric Device Applications	Photo-refractive Applications
• Los Alamos Lab* (S.C. Stotlar)	• Night Vision Lab* (Bucky Freeman)	• Night Vision Lab* (R. Buser)	• Plessey Co.* (F. Ainger)	• Caltech* (A. Yariv)
• Rockwell Intl.	• Bell Labs* (A Glass)	• Harry Diamond Lab (G. Simonis)	• Marquette Unit. (Prof. Joshi)	• Rockwell (J. Tracy)
	• NRL* (H. Taylor)	• Univ. of Missouri* (Prof. Werner)		• Hanscon AFB (Dr. Ludman)
	• Rockwell Intl* (J. Tracy)			

*SBN single crystals have been supplied.

Table 3

Requests for SBN Single Crystals: Applications

Research Organization	Application	Status
Rockwell International John Tracy	Electro-optic and blue-green filters	Supplied
Bell Labs A. Glass	Electro-optic	Supplied
Naval Research Lab* Henry Taylor	Electro-optics: modulators, switches and Bragg cells	Supplied
Night Vision Lab: Electro-Optic Lab	Millimeter wave, frequency doubling and electro-optics	Supplied
Los Alamos Laboratory,* New Mexico	Pyroelectric detectors: high speed devices (in IR and UV region)	Supplied
Harry Diamond Laboratory Phil Brody	Millimeter wave, photovoltaic and ferroelectric devices	Supplied
Univ. of Missouri-Columbia Prof. S.A. Werner	Neutron-diffraction studies for soft mode studies	
Marquette University Prof. S. Joshi	Effects of external electric field on SAW properties	Supplied
Caltech Prof. A. Yariv	Photo refractive studies	Supplied

*Results of their investigations are available.

Table 4

Military Agencies Interested in Tungsten Bronze Single Crystals

ARMY:	
• Night Vision Laboratory (Bucky Freeman & R. Buser)	Millimeter wave and electro-optic device applications.
• Harry Diamond Laboratory (G. Simonis)	Millimeter wave, above 94 GHz.
• BMD/ATC (Fan King)	Millimeter wave, present interest at 35 GHz
• ARO (A. Tauber & H. Wittman)	Millimeter wave materials
NAVY:	
• ONR (R. Pohanka & R. Brandt)	Dielectrics for millimeter wave, underwater hydrophones
• NRL (H. Taylor & W. Burns)	Electro-optic applications
AIR FORCE:	
• AFOSR (H. Winsor & C. Gardner)	Surface acoustic wave applications

particular agencies involved with each application. It is evident from Tables 2 to 4 that there is substantial interest in SBN and other tungsten bronze single crystal materials for a wide variety of potential device applications. With continued work in the areas of crystal chemistry, material purity and improved growth conditions, this family of materials should find even greater levels of interest in the future.

3.0 PHENOMENOLOGICAL MODEL

3.1 Introduction

The present approach to a phenomenological description of the elasto-electric behavior of the tungsten-bronze family of ferroelectrics was predicated on the assumption that if a material has a direction of propagation for a bulk acoustic wave in which the delay time is independent of temperature, it will be of interest also for surface acoustic wave devices (SAW) and will have a high probability of also having temperature-compensated directions for SAW. This is especially true if the bulk shear modulus is temperature-compensated, and was again confirmed by the results of the present study.

The conditions which dictate the temperature coefficient of delay for a bulk wave have been given as

$$\frac{1}{\tau}\left(\frac{\partial \tau}{\partial T}\right)_P = \alpha_s - \frac{1}{2}\alpha_v - \frac{1}{2}\frac{1}{\bar{C}}\left(\frac{d\bar{C}}{dT}\right)_P \tag{1a}$$

where α_s is the linear thermal expansion coefficient in the direction of propagation, α_v is the volume expansion coefficient, and

$$\bar{C}_{ijk\ell} = C^{E}_{ihk\ell} + \frac{d_{pij}d_{qk\ell}N_pN_q}{\epsilon^{x}_{rs}N_rN_s} \tag{1b}$$

is the effective elastic constant tensor for the piezoelectric. The first term in Eq. (1b) is the adiabatic elastic constant at constant electric field. The second term is the piezoelectric stiffening term which depends not only on the piezoelectric tensor, but also on the dielectric permittivity tensor and the direction cosines of the wave vector K (the N_j's).

The elastic constant which appears in (1b) can be for a general direction, thus for an orthorhombic bronze the temperature coefficient of delay is controlled by nine elastic, five piezoelectric, and three dielectric constants

and their temperature derivatives, and three independent thermal expansion coefficients. For the tetragonal bronze the situation is only slightly easier with six elastic, three piezoelectric, two dielectric constants, and two independent expansion parameters.

It would indeed be a daunting task to measure up all of these constants and derivatives in the full family of bronze compositions which have been identified. On the other hand, because of the complexity of the bronze structure, it is not yet possible to go back to first principles and derive from atomistic models values of the parameters and derivatives which would be meaningful.

What has been accomplished on this present contract is the development of an extension to the Landau:Ginsburg:Devonshire (L.G.D.) thermodynamic phenomenology which permits for the first time the modeling of the dielectric, elastic, piezoelectric and thermoelectric properties of a simple proper ferroelectric.

In the thermodynamic phenomenological modeling the non-zero stiffnesses and coupling parameters are determined by the prototypic symmetry, and it does appear that the higher order stiffnesses which control the magnitude of P_s mutate only slowly with cationic composition in a given symmetry group, while the coupling parameters change hardly at all with composition or temperature.

3.2 Thermodynamic Phenomenology

In general, the thermodynamic function of interest to describe the isothermal, isobaric properties of a polarizable deformable insulator is the elastic Gibbs function G_1 defined by

$$G_1 = U = TS - Xx \qquad (2)$$

where U is the internal energy, S the entropy, T the temperature, X the elastic stress, and x the strain. T and S are scalar, but X and small x will be second rank tensors.

The increment of G_1, dG_1, will be made up from

$$dG_1 = -SdT - xdX + EdP \tag{3}$$

where E is the electric field, P the electric polarization, and E and P are polar vectors. Thus from the partial derivatives of G_1 we may derive the strain x as

$$\left(\frac{\partial G_1}{\partial X}\right)_{TP} = - x \tag{4}$$

the electric compliance at constant P (stiffened)

$$\left(\frac{\partial^2 G_1}{\partial X^2}\right)_{TP} = s^P \tag{5}$$

electric field E

$$\left(\frac{\partial G_1}{\partial P}\right)_{TX} = E \tag{6}$$

dielectric stiffness X

$$\left(\frac{\partial^2 G_1}{\partial P^2}\right)_{TX} = X^X \tag{7}$$

and the piezoelectric polarization constant b

$$\left(\frac{\partial^2 G_1}{\partial P\, \partial X}\right)_T = \left(\frac{\partial E}{\partial X}\right)_T = b^T \tag{8}$$

which is related to the more frequently used d constant by

$$d^T = \left(\frac{\partial P}{\partial X}\right)_T = \left(\frac{\partial E}{\partial X}\right)\left(\frac{\partial P}{\partial E}\right) = b/X^X \tag{9}$$

It is conventional in Landau:Ginsburg:Devonshire phenomenological theory to take out the elastic Gibbs energy of the unpolarized undeformed

crystal and write

$$\Delta G_1 = G_{i(\text{polarized})} - G_{1(\text{unpolarized})} = f(PXT) \tag{10}$$

and to separate the function f into three components

$$\Delta G_1 = f(PT) + f(XT) + f(XP) \quad . \tag{11}$$

Inserting now the vector nature of P and E, and the tensor form of Xx, f(PT) is expressed as a power series expansion

$$f(PT) = \alpha_{ij} P_i P_j + \alpha_{ijk} P_i P_j P_k + \ldots\ldots\ldots \tag{12}$$

where the α_{ijk} are limited by the prototype symmetry and only the α_{ij} are temperature dependent. If the ferroelectric transition is first order, it is necessary to include at least the first 6th power terms in P.

Usually only "Hookian" elastic behavior is considered and f(XT) takes the simple form

$$f(X,T) = -\frac{1}{2} s_{ijkl} X_{ij} X_{kl} \quad . \tag{13}$$

Heretofore it has been considered necessary only to include the lowest power symmetry allowed coupling terms between P and X, so that f(XP) is given by either

$$f(X,P) = - b_{ijk} P_i X_{jk} \tag{14}$$

or

$$f(X,P) = - Q_{ijkl} P_i P_j X_{kl} \tag{15}$$

where Q_{ijkl} are the symmetry permitted electrostriction constants.

For centric prototype structures of the type to be considered, all $b_{ijk} \equiv 0$, and the phase change at T_c is first order. Since 6th power terms in P are absolutely necessary it seems illogical to consider only the 4th rank coupling terms, and we propose to add terms of the form

$$- [\Phi_{ijklmn} P_i P_j X_{kl} X_{mn}] - [W_{ijklmn} P_i P_j P_l X_{mn}] \quad . \tag{16}$$

For the elastic behavior clearly the Φ terms are most important. In the unmodified LGD theory in the spontaneously polarized phase, taking second partial derivatives with respect to the X_{ij}, obviously all Q terms drop out so that

$$s^P_{klmn(polarized)} = s^P_{klmn(unpolarized)}$$

whereas if the Φ constants have significant magnitude

$$s^P_{klmn(polarized)} = s^P_{klmn(unpolarized)} + \Phi_{ijklmn} P_i P_j$$

Since the polarization components $P_i P_j$ in the simple ferroelectric have strong temperature dependence, the electrostrictive term may be most important in dictating the elastic compliances in the ferroelectric phase.

3.3 Application of the Phenomenology to Tungsten Bronze Structure Ferroelectrics

The tetragonal bronze structure ferroelectrics form a very large family with over 100 known individual ferroelectric compounds and innumerable possible solid solutions between these end members. Paraelectric prototypic point symmetry is 4/mmm and though seven ferroelectric species are theoretically possible, only two different ferroelectric forms are known: an orthorhombic form in which the spontaneous polarization is along 110, $1\bar{1}0$, $\bar{1}10$, or $\bar{1}\bar{1}0$, which is in polar mm2 symmetry, and a tetragonal form in which P_s lies along 001 or $00\bar{1}$ and which has polar tetragonal 4mm symmetry.

3.4 Symmetry Constraints

For the prototypic 4/mmm centric group the permitted dielectric stiffnesses α_{ij}, fourth order stiffnesses α_{ijkl}, electrostrictive Q_{ijkl} and elastic compliance constants s_{ijkl} are listed in Table 5. The sixth order stiffnesses α_{ijklmn} are listed in Table 6, and the sixth order electrostriction constants Φ_{ijklmn} in Table 7.

The LGD phenomenological elastic Gibbs function has the form

$$\begin{aligned}
\Delta G = {} & \alpha_1(P_1^2 + P_2^2) + \alpha_3 P_3^2 + \alpha_{11}(P_1^4 + P_2^4) + \alpha_{33} P_3^4 \\
& + \alpha_{13}(P_1^2 P_3^2 + P_2^2 P_3^2) + \alpha_{12} P_1^2 P_2^2 + \alpha_{333} P_3^6 \\
& + \alpha_{111}(P_1^6 + P_2^6) - \tfrac{1}{2} S_{11}(X_1^2 + X_2^2) - S_{12} X_1 X_2 \\
& - S_{13}(X_1 + X_2) X_3 - \tfrac{1}{2} S_{33} \times \tfrac{2}{3} - \tfrac{1}{2} S_{44}(X_4^2 + X_5^2) \\
& - \tfrac{1}{2} S_{66} X_6^2 - Q_{11}(P_1^2 X_1 + P_2^2 X_2) - Q_{12}(P_1^2 X_2 + P_2^2 X_1) \\
& - Q_{13}(P_1^2 X_3 + P_2^2 X_3) - Q_{31}(P_3^2 X_1 + P_3^2 X_2) \\
& - Q_{33} P_3^2 X_3 - Q_{44}(P_2 P_3 X_4 + P_1 P_3 X_5) \\
& - Q_{66} P_1 P_2 X_6 \quad .
\end{aligned} \tag{17}$$

Table 5

Symmetry Permitted Second and Fourth Rank Polar Tensor for Point Symmetry 4/mmm

α_{ij} dielectric stiffnesses at constant stress
α_{ijkl} fourth order stiffnesses at constant stress
Q_{ijkl} Quadratic electrostriction in polarization notation
s_{ijkl} elastic compliances at constant P

NYE's Matrix Notation		Full Tensor Notation		
Term	Symmetry Equivalent Terms	Term	Symmetry Equivalent Terms	Number of Equivalent Terms
α_1	α_2	α_{11}	α_{22}	2
α_3		α_{33}		1
α_{11}	α_{22}	α_{1111}	α_{2222}	2
α_{12}	α_{21}, α_{66}	α_{1122}	α_{1212}, α_{1221}, α_{2112}, α_{2121}, α_{2211}	
α_{13}	α_{31}, α_{23}, α_{32}, α_{44}, α_{55} ($\alpha_{44} = 4\alpha_{2323}$)	α_{1133}	α_{3311}, α_{2233}, α_{3322}, α_{1313} α_{1331}, α_{3113}, α_{3131}, α_{2323}, α_{2332}, α_{3223}, α_{3232}	12
α_{33}		α_{3333}		1
Q_{11}	Q_{22}	Q_{1111}	Q_{2222}	2
Q_{12}	Q_{21}	Q_{1122}	Q_{2211}	2
Q_{13}	Q_{23}	Q_{1133}	Q_{2233}	2
Q_{31}	Q_{32}	Q_{3311}	Q_{3322}	2
Q_{33}		Q_{3333}		1
Q_{44}	Q_{55}	Q_{2323}	Q_{2332}, Q_{3223}, Q_{3232}, Q_{1313}, Q_{1331}, Q_{3113}, Q_{3131}	8
Q_{66}		Q_{1212}	Q_{1221}, Q_{2112}, Q_{2121}	4
S_{11}	S_{22}	S_{1111}	S_{2222}	2
S_{12}	S_{21}	S_{1122}	S_{2211}	2
S_{13}	S, S_{23}, S_{32}	S_{1133}	S_{3311}, S_{2233}, S_{3322}	4
S_{33}		S_{3333}		1
S_{44}	S_{55}	S_{2323}	S_{2332}, S_{3223}, S_{3232}, S_{1313}, S_{1331}, S_{3113}, S_{3131}	8
S_{66}		S_{1212}	S_{1221}, S_{2112}, S_{2121}	4

Table 6

Symmetry Permitted Sixth Rank Dielectric Stiffness Components α_{ijklmn} for Point Symmetry 4/mmm

Term	Symmetry Related Terms	Number of Equivalent Terms
1. α_{11}	222	2
2. α_{112}	166, 121, 616, 661, 211, 221, 266,	30
3. α_{113}	155, 131, 515, 551, 331, 223, 244, 232, 424, 442, 322	30
4. α_{123}	144, 132, 525, 645, 546, 636, 663, 564, 654, 552, 621, 441, 231, 465 366, 255, 456, 213, 414, 312	90
5. α_{133}	535, 553, 331, 355, 313, 233, 434, 443, 332, 344, 323	30
6. α_{333}		1

Table 7

Sixth Order Electrostriction Constants Φ_{ijklmn} for Point Symmetry 4/mmm

Term	Symmetry Related Terms	Number of Equivalent Terms
1. Φ_{112}	222	2
2. Φ_{112}	121, 221, 212	4
3. Φ_{113}	131, 223, 232	4
4. Φ_{166}	266	8
5. Φ_{244}	155	8
6. Φ_{122}	211	2
7. Φ_{123}	132, 213, 231	4
8. Φ_{144}	255	8
9. Φ_{133}	233	2
10. Φ_{616}	661, 626, 662	2
11. Φ_{636}	663	8
12. Φ_{645}	654	16
13. Φ_{424}	442, 515, 551	16
14. Φ_{456}	465, 546, 564	32
15. Φ_{414}	441, 525, 552	16
16. Φ_{434}	443, 535, 553	16
17. Φ_{311}	322	2
18. Φ_{312}	321	2
19. Φ_{313}	331, 323, 332	4
20. Φ_{366}		4
21. Φ_{344}	355	8
22. Φ_{333}		1

The first partial derivatives with respect to the polarization give field components

$$\frac{\partial \Delta G}{\partial P_1} = E_1 = 2\alpha_1 P_1 + 4\alpha_{11} P_1^3 + 2\alpha_{13} P_1 P_3^2 + 2\alpha_{12} P_1 P_2^2 + 6\alpha_{111} P_1^5 - 2Q_{11} P_1 X_1$$

$$- 2Q_{12} P_1 X_2 - Q_{13} P_1 X_3 - Q_{44} P_3 X_5 - Q_{66} P_2 X_6$$

$$\frac{\partial \Delta G}{\partial P_2} = E_2 = 2\alpha_1 P_2 + 4\alpha_{11} P_2^3 + 2\alpha_{13} P_2 P_3^2 + 2\alpha_{12} P_2 P_1^2 + 6\alpha_{111} P_2^5 - 2Q_{11} P_2 X_2$$

$$- 2Q_{12} P_2 X_1 - 2Q_{13} P_2 X_3 - Q_{44} P_3 X_4 - Q_{66} P_1 X_6 \qquad (18)$$

$$\frac{\partial \Delta G}{\partial P_3} = E_3 = 2\alpha_3 P_3 + 4\alpha_{33} P_3^3 + 2\alpha_{13}(P_1^2 + P_2^2) P_3 + 6\alpha_{333} P_3^5 - 2Q_{31} P_3 (X_1 + X_2)$$

$$- 2Q_{33} P_3 X_3 - Q_{44}(P_2 X_4 + P_1 X_5) \quad .$$

It is the solutions of these equations with $E_i \equiv 0$ which determine the ferroelectric states. For the tetragonal case, the dielectric data in the paraelectric phase indicate that α_3 is a linearly decreasing function of T passing through zero near T_c, that is

$$\alpha_3 = \alpha_{30} (T - \theta_3) \qquad (19)$$

where θ_3 is close to T_c, whereas α_1 also has the same form

$$\alpha_1 = \alpha_{10}(T - \theta_1) \qquad (20)$$

where θ_1 is very much below T_c.

For temperatures less than the ferroelectric Curie point T_c in this case, the spontaneous polarization along the tetrad axis is given by the solution of

$$0 = 2\alpha_{30}(T - \theta_3) + 4\alpha_{33} P_3^2 + 6\alpha_{333} P_3^4 \qquad (21)$$

and

$$P_1 = P_2 = 0 \quad . \tag{22}$$

The isothermal dielectric stiffnesses are

$$\begin{aligned} X_{11}^T &= 2\alpha_1 + 2\alpha_{13}P_3^2 \\ X_{22}^T &= 2\alpha_1 + 2\alpha_{13}P_3^2 \\ X_{33}^T &= 2\alpha_3 + 12\alpha_{33}P_3^2 + 30\alpha_{333}P_3^4 \\ X_{12}^T &= X_{13}^T = X_{23}^T = 0 \quad . \end{aligned} \tag{23}$$

The tetragonal spontaneous strains are given by

$$\begin{aligned} x_1 &= Q_{31}P_3^2 \quad x_4 = x_5 + x_6 = 0 \\ x_2 &= Q_{31}P_3^2 \\ x_3 &= Q_{33}P_3^2 \end{aligned} \tag{24}$$

and the piezoelectric b coefficients by

$$\begin{array}{lll} b_{11} = 0 & b_{21} = 0 & b_{31} = 2Q_{31}P_3 \\ b_{12} = 0 & b_{22} = 0 & b_{32} = 2Q_{31}P_3 \\ b_{13} = 0 & b_{23} = 0 & b_{33} = 2Q_{33}P_3 \\ b_{14} = 0 & b_{24} = Q_{44}P_3 & b_{34} = 0 \\ b_{15} = Q_{44}P_3 & b_{25} = 0 & b_{35} = 0 \\ b_{16} = 0 & b_{26} = 0 & b_{36} = 0 \end{array} \tag{25}$$

If the sixth order ϕ terms are added to Eq. (17), then the second derivatives with respect to the stress give the stiffened elastic compliances s^P_{ij} which take the form

$$
\begin{aligned}
S^P_{11}(P) &= S^P_{22}(P) = S^P_{11}(0) + \Phi_{311}P_3^2 \\
S^P_{12}(P) &= S^P_{12}(0) + \Phi_{312}P_3^2 \\
S^P_{13}(P) &= S^P_{23} = S^P_{13}(0) + \Phi_{313}P_3^2 \\
S^P_{33}(P) &= S^P_{33}(0) + \Phi_{333}P_3^2 \\
S^P_{44}(P) &= S^P_{55}(P) = S^P_{44}(0) + \Phi_{344}P_3^2 \\
S^P_{66}(P) &= S^P_{66}(0) + \Phi_{366}P_3^2
\end{aligned}
\qquad (26)
$$

where the suffix (P) indicates the S value at polarization level P and the suffix (0) the prototypic value when P = 0.

3.5 Derivation of the Thermodynamic Constants for $Sr_{0.61}Ba_{0.39}Nb_2O_6$ Bronze

The most important initial consideration was to determine whether the Φ constants that are symmetry permitted have magnitudes which make a significant contribution to the s^P_{ijkl} and thus are of importance in determining the elastic response and its temperature behavior in the polarized ferroelectric phase.

Fortunately because of the very high polarizability along the 4-fold axis for temperatures above T_c where $P_s = 0$ it is possible to determine the Φ_{3ij} constants by a very simple direct experimental test. If a suitable bar-shaped sample of SBN (Fig. 2) is subjected to a DC field E_3 at a temperature above T_c, a high non-zero P_3 may be induced in the bar, which induces through Eq. (2) non-zero values of the piezoelectric constants. If the electrical impedance of the bar is now explored with a low level probing field, the resonance and antiresonance frequencies corresponding to the different modes of elastic vibration of

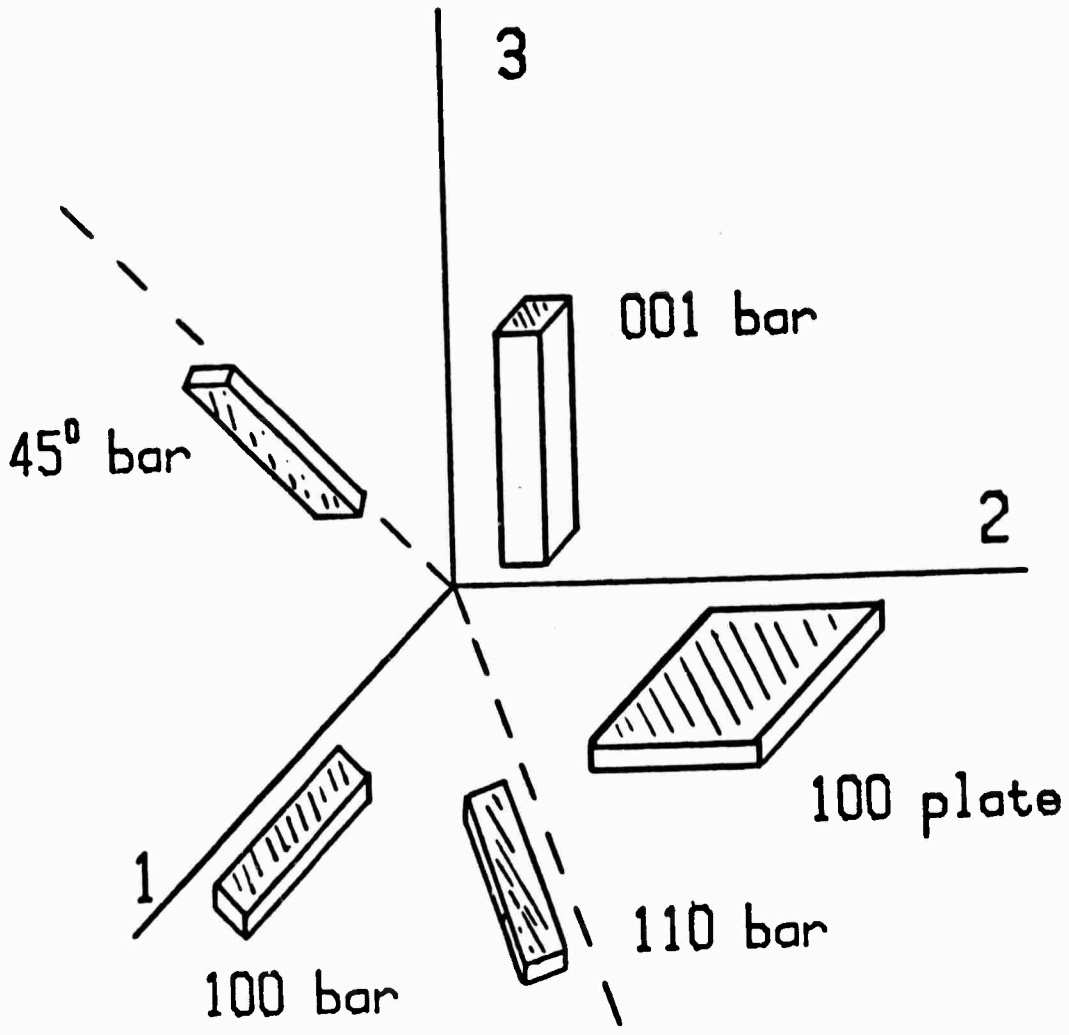

Fig. 2 Shapes and orientations of test specimens.

the bar may be excited (Fig. 3), and the elastic parameters s^E_{ij}, s^P_{ij} deduced from the resonance frequencies and the dimensions and density of the bar.

Be repeating the measurement at a sequence of different E field levels, different values of P may be induced and the relationships expected in Eq. (26) explored. It may be noted that in these extremely polarizable crystals the dielectric properties exhibit significant nonlinearity at quite low E_3 levels so that it is necessary to measure the P_3 value for each field level using a slow sweep Sawyer and Tower method.

Typical measurements of S^E_{11} and S^P_{11} as a function of $P_3{}^2$ taken from resonance data from an x-cut bar at 121°C (well above T_c) are shown in Fig. 4, and of $S^{E'}_{11}$ and $S^{P'}_{11}$ for a rotated cut at 121°C in Fig. 5. Clearly both S^P_{11} and $S^{P'}_{11}$ are linear functions of $P_3{}^2$ and the magnitude of the appropriate Φ_{3ij} can be deduced from the slope of the S^P_{ij} lines.

From repeated measurements of the field induced polarization dependence of the resonance for different cuts at a sequence of temperatures above T_c, the expected near temperature independence of the Φ_{3ij} constants is demonstrated in Fig. 6, yielding the values of the Φ constants given in Table 8. Thus the importance of the sixth order electrostriction constant for the elastic behavior in the bronze crystal is clearly established.

The next question that must be addressed is whether the values of the Φ_{ijklmn} constants measured under induced polarization in the paraelectric phase can be used, as would be suggested by Eq. (26), to describe the changes in elastic behavior associated with the onset of spontaneous polarization in the ferroelectric phase. To make this next step, however, a special feature of ferroelectricity in the bronze structure materials must first be recognized. For many of these materials including the SBN bronze, it has been determined that the phase change at T_c is not abrupt, but is diffuse. Thus over a limited range of temperatures close to T_c paraelectric and ferroelectric phases coexist. The thermodynamic description which has been given above is appropriate for a completely homogeneous crystal which has an abrupt phase change T_c. It may be used, however, also in good approximation to describe a crystal with diffuse transition if the transition temperature T_c is presumed to be distributed.

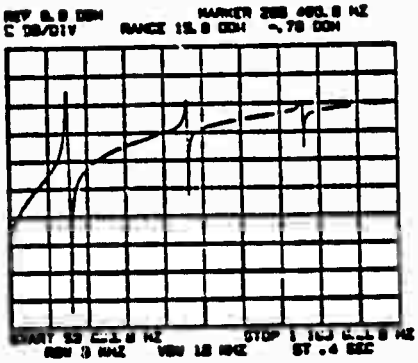

Fig. 3 Typical resonance spectrum for an SBN bar under DC bias above the Curie temperature T_c.

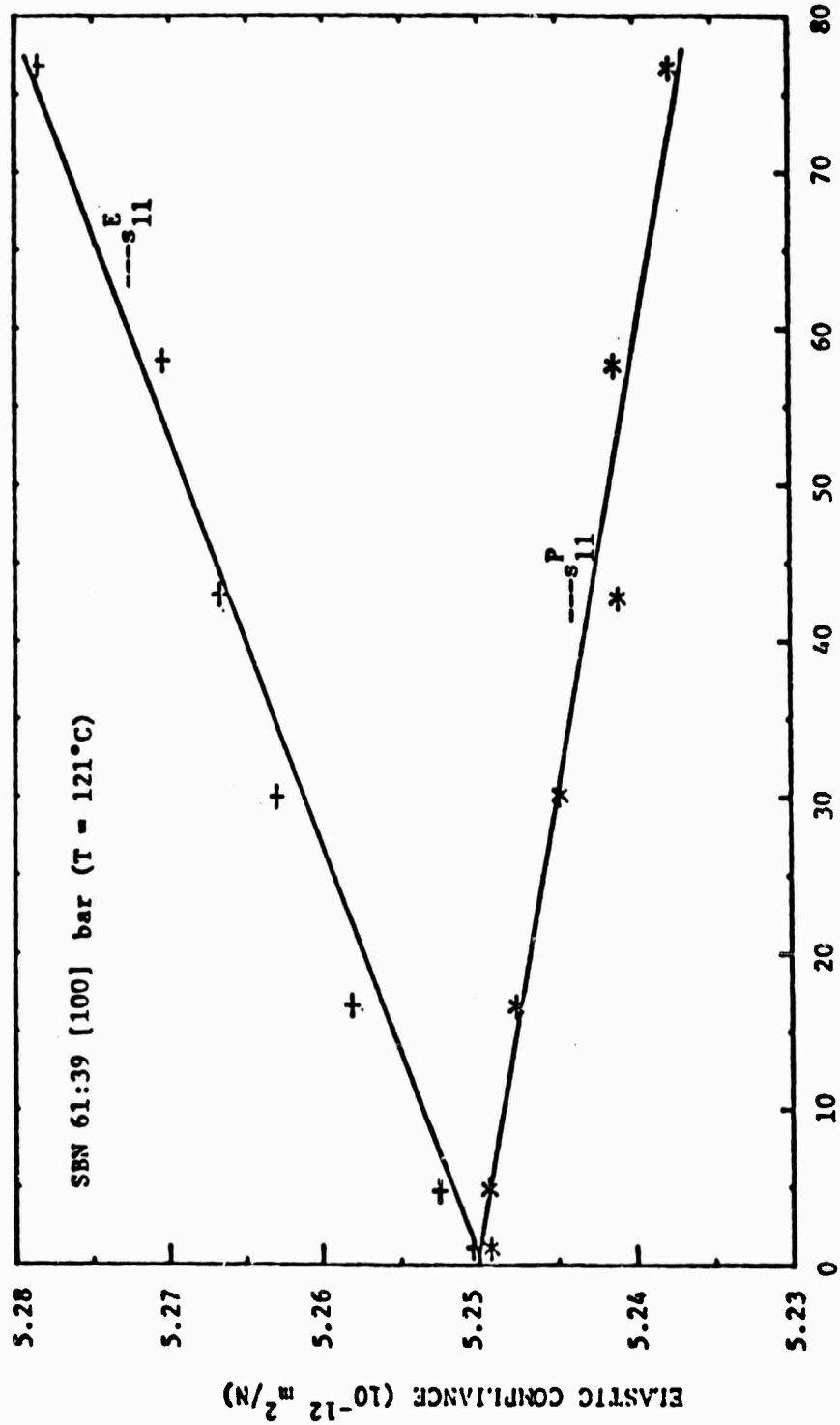

Fig. 4 Elastic compliances S_{11}^E and S_{11}^P as a function of induced polarization in SBN 61:39 measured at 121°C.

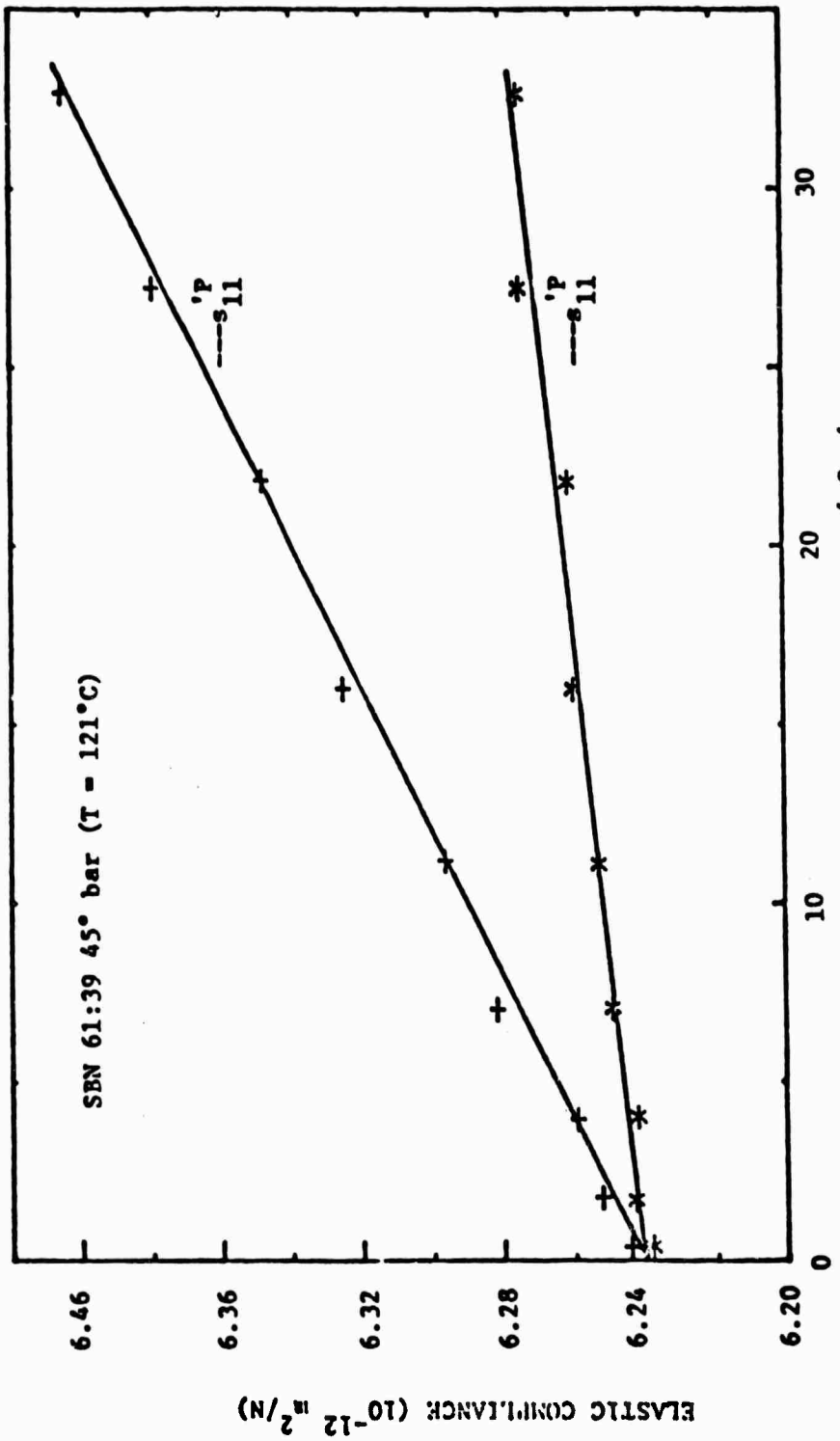

Fig. 5 Elastic compliances $s_{11}^{'E}$ and $s_{11}^{'P}$ as a function of induced polarization in SBN 61:39 measured at 121°C.

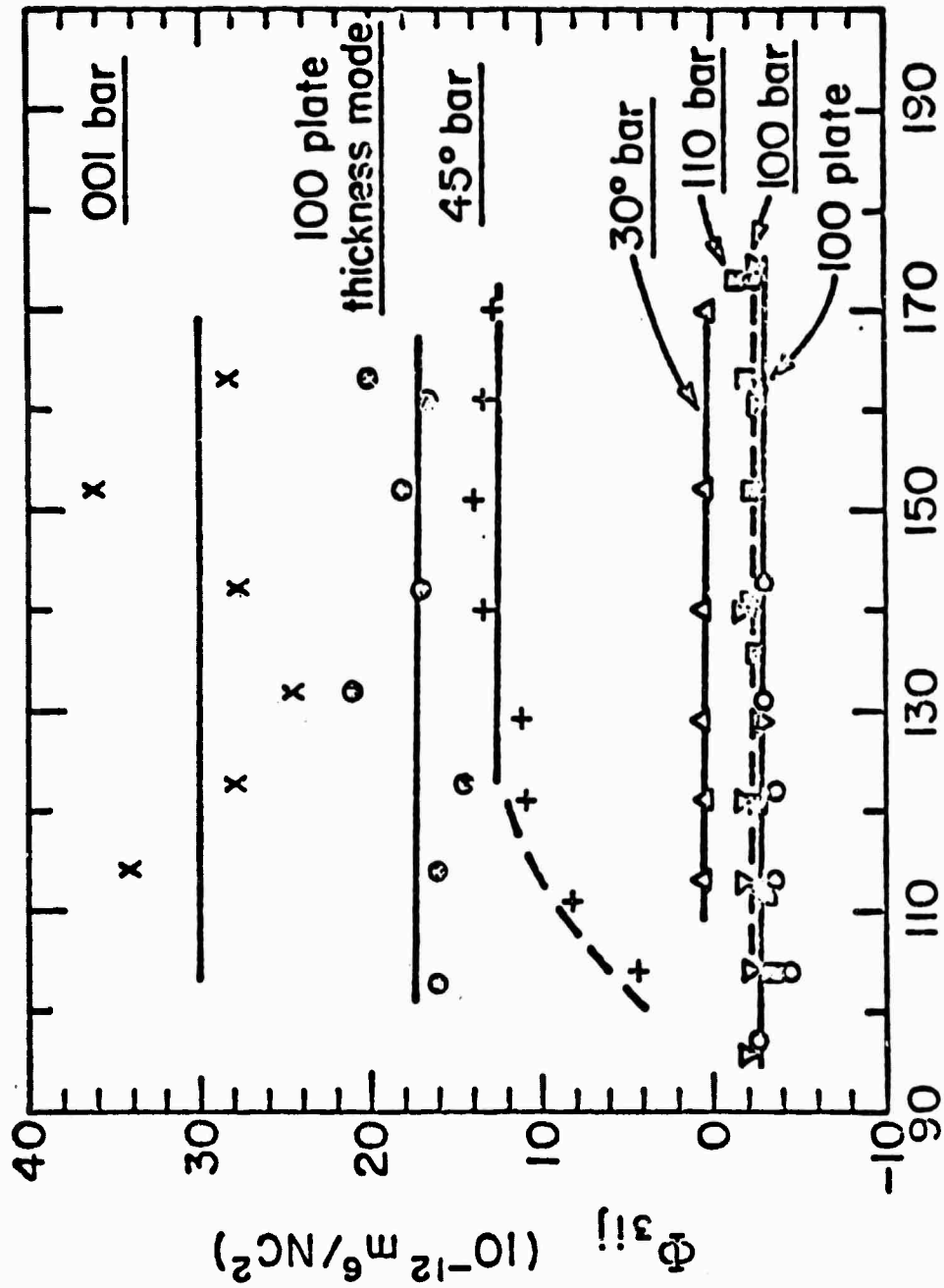

Fig. 6 Measured sixth order electrostriction Φ_{3ij} values of rotated and unrotated cuts over a range of temperature above T_c.

Table 8

Higher Order Electrostriction Constants Φ_{3ij}

Φ_{311}	-2.2×10^{-12} $m^6/N\text{-}coul^2$
Φ_{312}	-3
Φ_{313}	-5
Φ_{333}	+28
Φ_{334}	+35 *+(16)
Φ_{366}	-3

*The higher order Φ_{334} constant determined from the 30° bar. Believed to be the truer value, since less dependent on possible "anomalous" behavior found in the (001) polar direction.

Table 9

Determined Thermodynamic Parameters

α_{10} =	$7.44 \times 10^{-6}/°C \cdot \varepsilon_o$	Q_{31}	-0.71×10^{-2} $m^4/coul^2$
α_{30}	$5.04 \times 10^{-6}/°C \cdot \varepsilon_o$	Q_{33}	3.0 *(3.4)
θ_1	-379°C	Q_{44}	1.38
θ_3	73°C	Φ_{311}	-2.2×10^{-12} $m^6/N\text{-}coul^2$
T_c	77°C	Φ_{312}	-3
α_{13}	2.1×10^{-3} MKS	Φ_{313}	-5
α_{133}	2.11×10^{-2}	Φ_{333}	+28
α_{1333}	2.49×10^{-2}	Φ_{334}	+35 †(16)
α_{33}	-7.0×10^{-4}	Φ_{366}	-3
α_{333}	1.2×10^{-2}		

*The electrostriction constant (Q_{33}) as determined from the strain P_s data.
†The higher order Φ_{334} constant determined from the 30° bar. Believed to be the truer value, since less dependent on possible "anomalous" behavior found in the (001) polar direction.

The choice of the distribution function and the stiffness parameters is rigorously limited by the need to fit the observed dielectric permittivity and spontaneous electric polarization data. For the 61:39 SBN the chosen parameters are given in Table 9. The distribution of the Curie points is gaussian with a halfwidth ΔT = 8K.

For these parameters, measured and calculated polarization P_s is shown in Fig. 7, and the measured and calculated dielectric permittivity K_3 in Fig. 8 and the dielectric permittivity K_1 in Fig. 9.

Using precise x-ray diffraction measurements, the spontaneous elastic strain can be determined, and for a Q_{33} value of 0.34 m^4/c^2 the calculated strain is shown in Fig. 10, and thus the ferroelectric contribution to α_ℓ, the linear thermal expansion along "c", in Fig. 11.

If the resonance and antiresonance measurements are carried on down into the ferroelectric phase below $\bar{T}_c$, the same crystal cuts may be used to measure S^P_{ij} and S^E_{ij} in the single domain ferroelectric species. A crucial test of the predictive capability of the extended LGD method may then be made by comparing calculated S_{ij} constants derived using the measured high temperature Φ_{3ij} values and known P_s and the experimentally determined constants. Such comparisons for S^P_{11}, S^P_{12}, and S^P_{44} are shown in Fig. 12.

The agreement for S^P_{44} is excellent. For S^P_{11} and S^P_{12} however, there are clear compliance maxima near $\bar{T}_c$ which are not predicted. This breakdown of the simple theory is not, however, completely unexpected. Since the LGD phenomenology neglects all thermal fluctuations, and such fluctuations must become large close to a near 2nd order phase change, it is evident that $\overline{P^2}$ will not be zero just above $\bar{T}_c$ and an elastic softening through the normal electrostrictive effect is to be expected.

If this contribution due to fluctuations is assumed to be symmetrical about $\bar{T}_c$ then its effect can be removed and the agreement between theory and experiment for temperatures close to T_c is correspondingly improved.

Measurements of S^P_{33} show a very large compliance peak at T_c and the effect of fluctuations here is much too large to correct by the simple subtraction procedure.

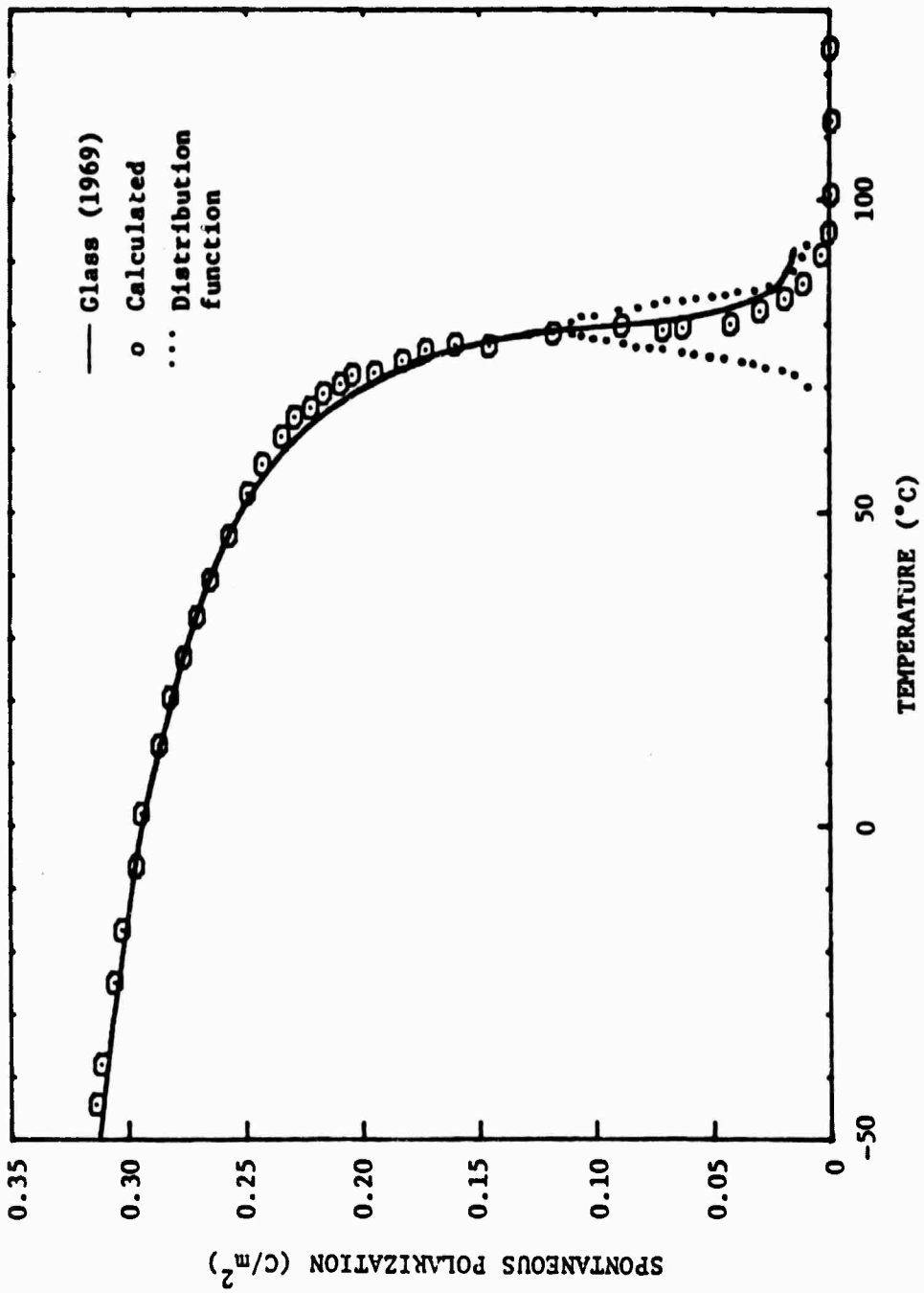

Fig. 7 The calculated plot of spontaneous polarization vs temperature for SBN 61:39 along with values reported for SBN 60:40 by Glass (1969).(6)

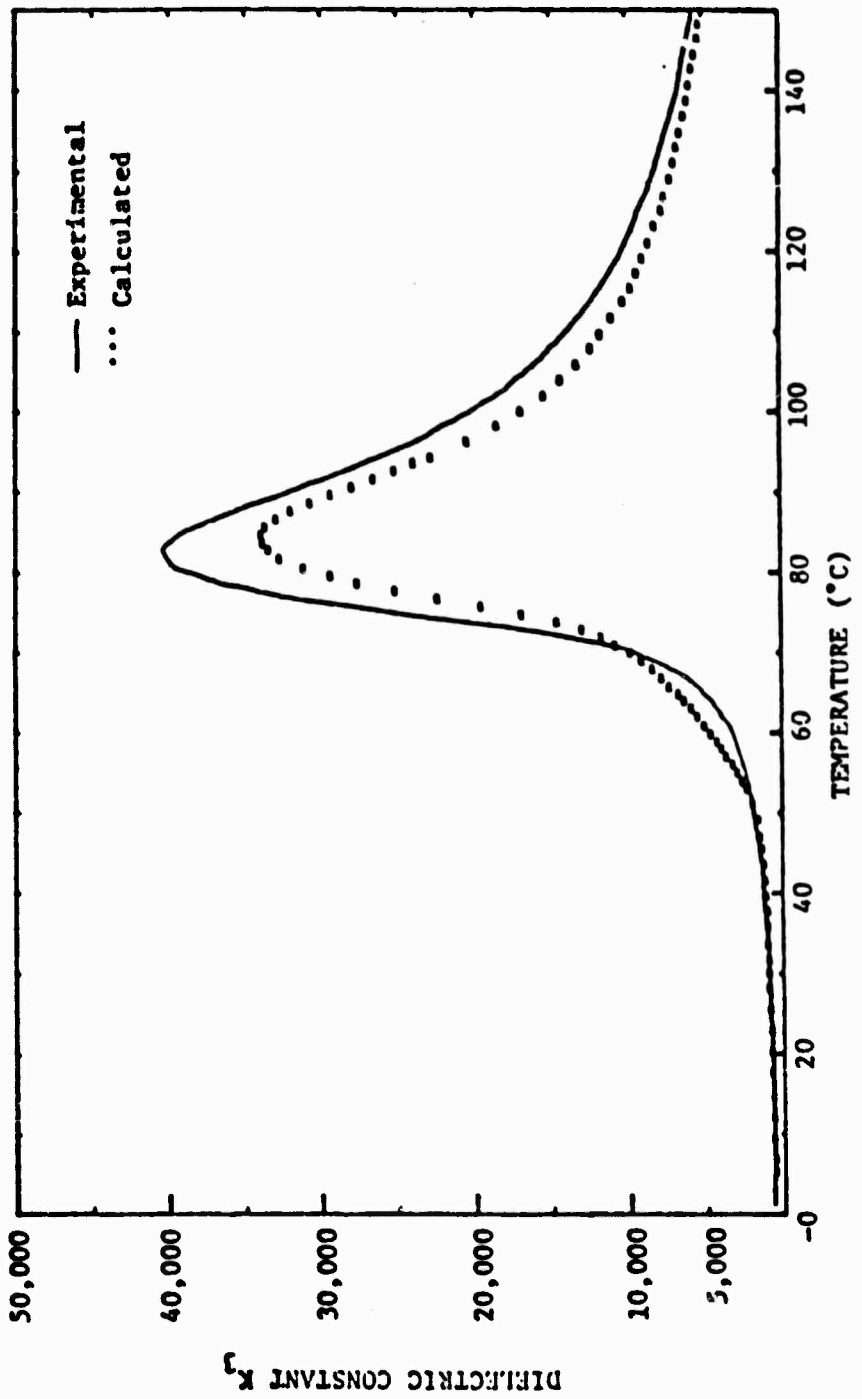

Fig. 8 The measured dielectric constant K_3 compared to the calculated using the distributed LGD model.

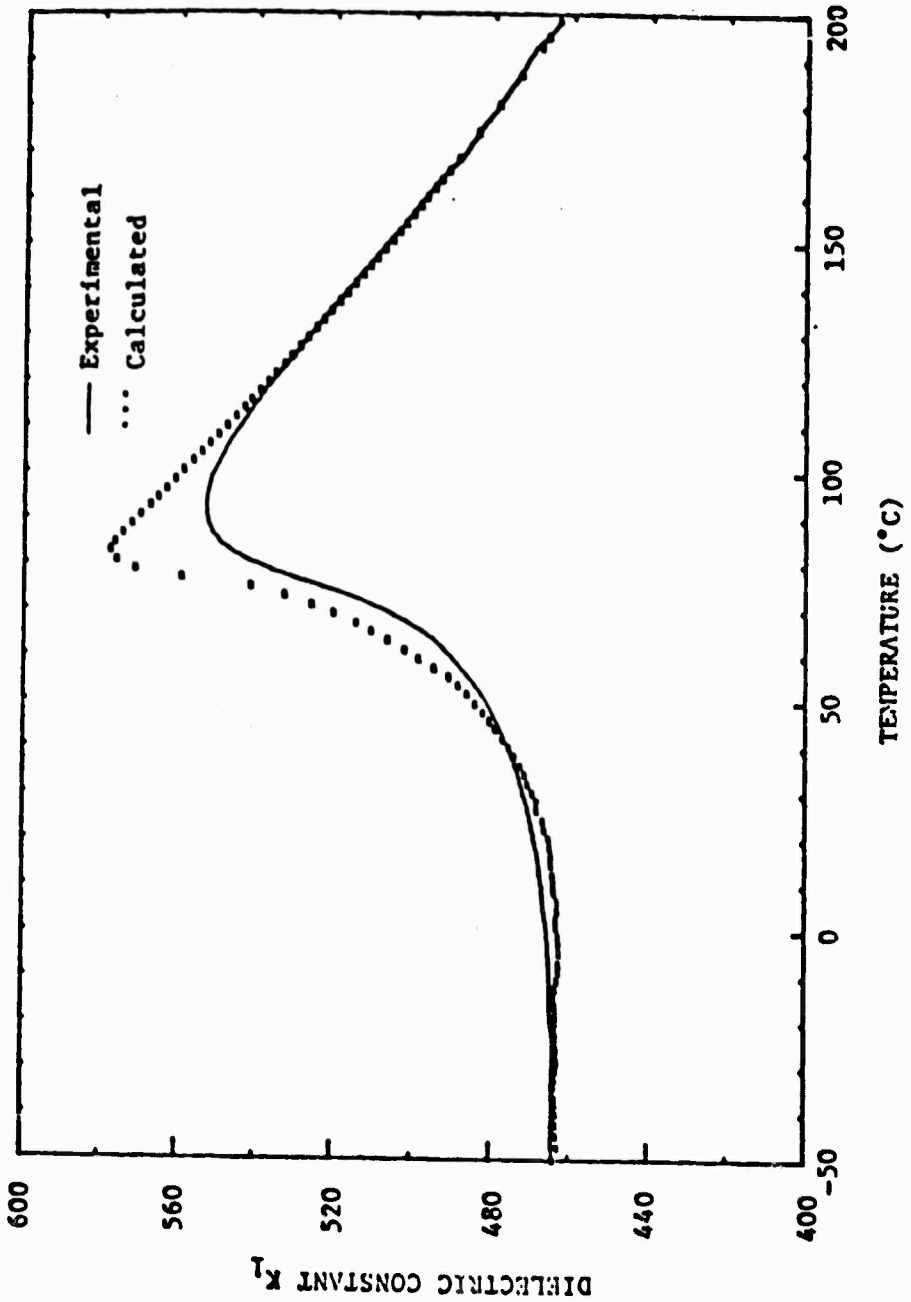

Fig. 9 The measured dielectric constant K_1 compared to the calculated using the distributed LGD model.

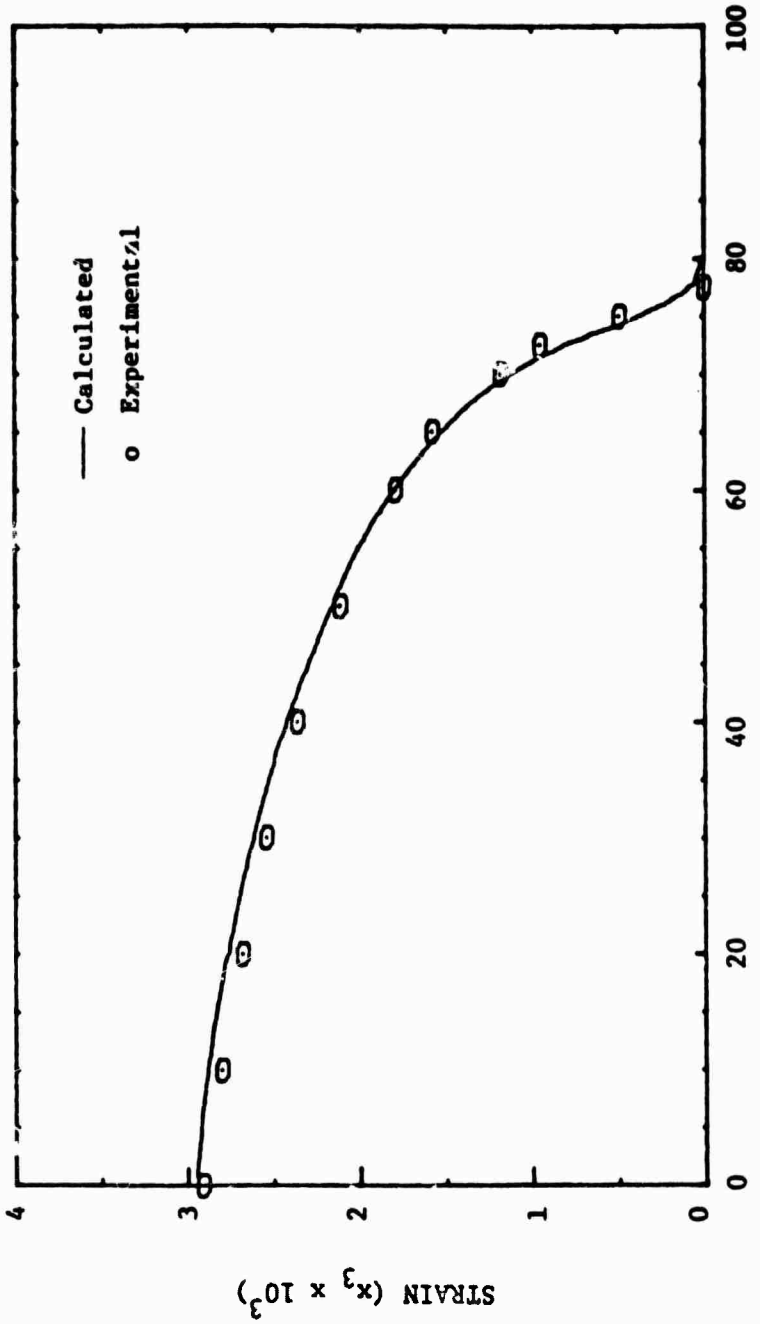

Fig. 10 Measured and derived strain x_3.

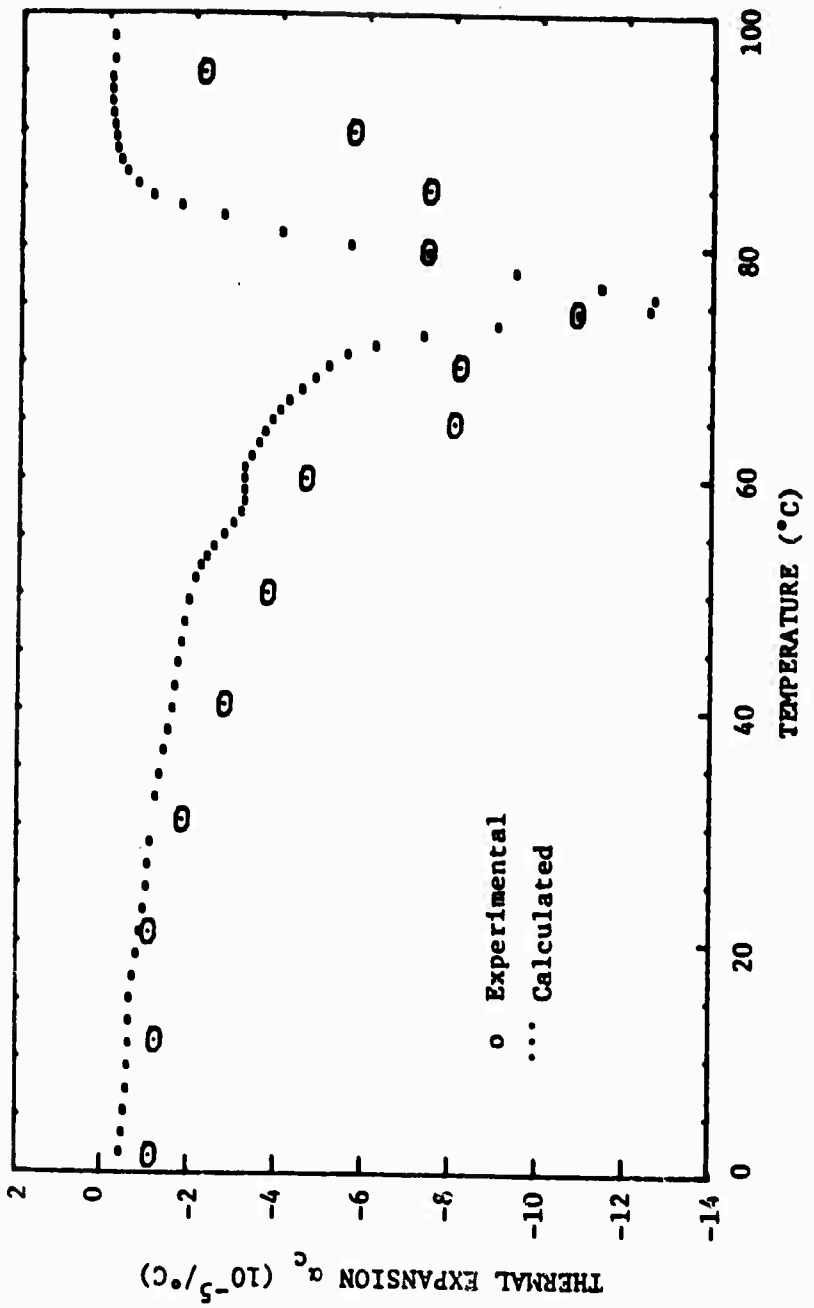

Fig. 11 Measured and derived thermal expansion α_c.

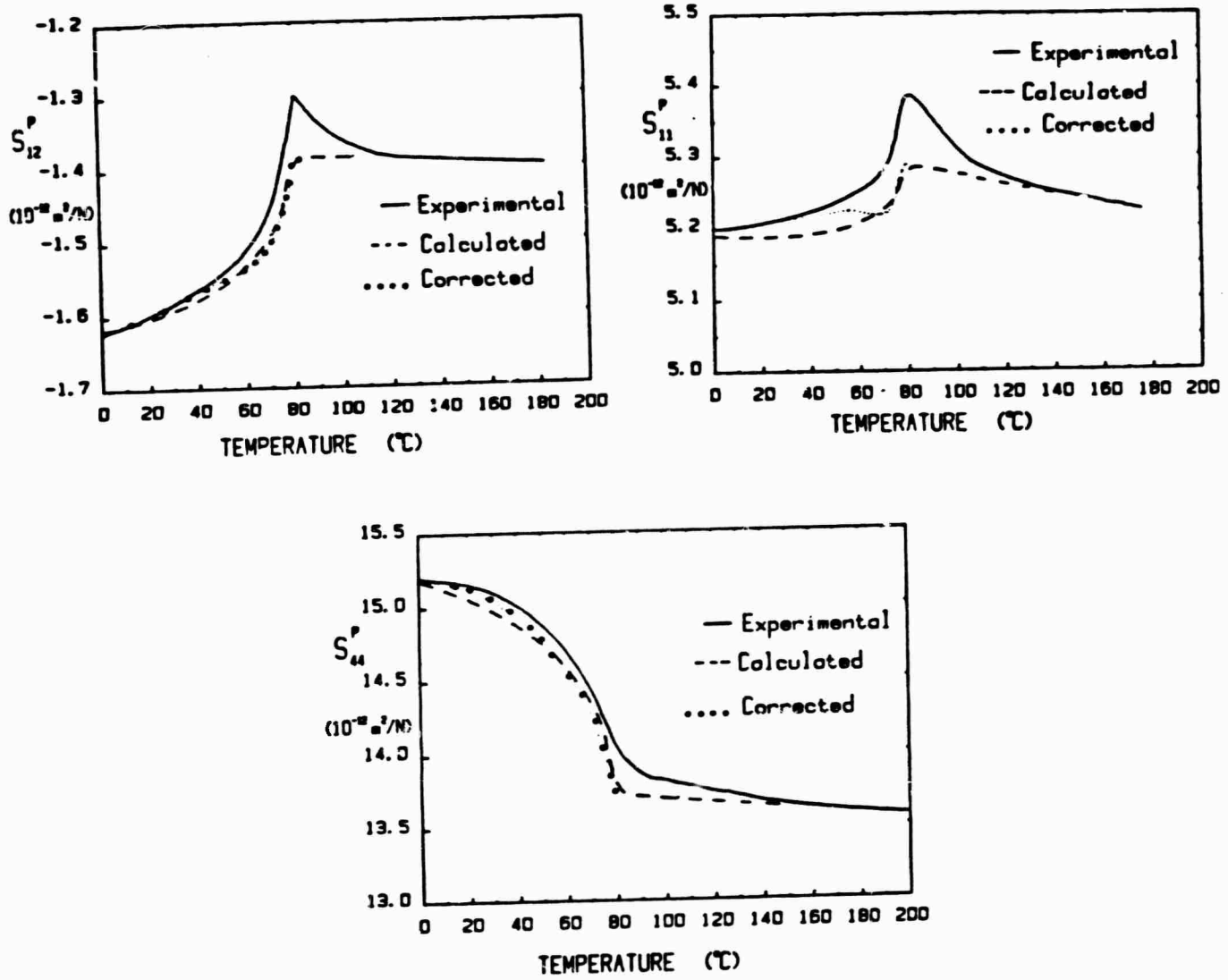

Fig. 12 S_{ij}^P measured from piezoelectric response data compared to S_{ij} derived using Φ_{3ij} values determined in the paraelectdric phase.

The complete set of electro-acoustic constants for the 61:39 SBN composition are summarized in Table 10 and the room temperature coefficients are also given in Table 10. Except for the measured S_{33}^{P}, calculated and predicted constants are in good agreement.

Table 10

Physical Constants of SBN at Room Temperature

$\varepsilon_{11}^{X}/\varepsilon_0$	470	$*\varepsilon_{11}^{x}/\varepsilon_0$	562	$T_{S_{11}}{}^{P}$	-1.2×10^{-4}/°C
$\varepsilon_{33}^{X}/\varepsilon_0$	880	$*\varepsilon_{33}^{x}/\varepsilon_0$	633	$T_{S_{12}}{}^{P}$	-9.2
$S_{11}{}^{E}$	$5.32 \times 10^{-12} m^2/N$	$S_{11}{}^{P}$	$5.21 \times 10^{-12} m^2/N$	$T_{S_{13}}{}^{P}$	-0.63
$S_{12}{}^{E}$	-1.46	$S_{12}{}^{P}$	-1.56	$T_{S_{33}}{}^{P}$	-5.0
$S_{13}{}^{E}$	-1.73	$S_{13}{}^{P}$	-2.21	$T_{S_{44}}{}^{P}$	+2.3
$S_{33}{}^{E}$	10.10	$S_{33}{}^{P}$	7.82	$T_{S_{66}}{}^{P}$	-0.80
$S_{44}{}^{E}$	15.48	$S_{44}{}^{P}$	15.22	$T_{\varepsilon_{11}}{}^{x}$	-4.8×10^{-3}/°C
$S_{66}{}^{E}$	14.4	$S_{66}{}^{P}$	14.4	$T_{\varepsilon_{31}}{}^{x}$	-0.20
d_{15}	31×10^{-12} C/N	k_{15}	0.13	$T_{d_{15}}$	-0.08×10^{-2}/°C
d_{31}	-30	k_{31}	0.14	$T_{d_{31}}$	-1.07
d_{33}	130	k_{33}	0.475	$T_{d_{33}}$	-1.23
†'1	8×10^{-6}/°C	k_t(thickness)	0.44	$T_{k_{15}}$	$-0.0\text{-}2 \times 10^{-3}$/°C
'3	-8	k_p(planar)	0.21	$T_{k_{31}}$	-0.99
				$T_{k_{33}}$	-1.36

*Dielectric permittivities at constant strain (x) were measured using a model 419JA RF impedance analyzer at a frequency greater than 50 MHz.

†Note: The thermal expansion coefficient $\underline{\alpha}$ not to be confused with the LGO α's as in Eq. (6).

3.6 Extension of the Model Studies to Other Bronzes

The thermodynamic model calculations for the $Sr_{0.61}Ba_{0.39}Nb_2O_6$ bronze give confidence in the applicability of the method, and of the importance of the higher order electrostriction in controlling the temperature dependence of compliances in the ferroelectric self-polarized phase. Our most urgent task is to extend the model calculations to at least two other bronze compositions so as to determine if the higher order constants are largely independent of cation make-up in the bronze. This verification will enable us to go ahead with confidence to calculate the full gamut of elasto-dielectric properties available in the whole complex bronze structure family.

Unfortunately under the time constraints of the contract, it became clear that it would not be possible to grow additional crystals just for model parameters, but rather that we must attempt to extrapolate quickly to a near optimum composition.

Two shortcomings of the SBN crystal at the 61:39 composition should be addressed:

(1) The low value of T_c which makes the crystal vulnerable to depoling.

(2) The small value of d_{15} which reduces coupling for the desirable compensated cuts.

Parameters which are available for a range of bronze compositions are the Curie-Weiss temperatures θ_1 and θ_2. Keeping all other constants as for SBN 61:39 but continuously raising θ_1, it is clear that the permittivity K_1 and the piezoelectric constant d_{15} can be raised substantially by increasing θ_1.

Based on the requirement to be able to control θ_1 and θ_3, and to verify model parameters, two new composition families were chosen: $Pb_{1-x}Ba_xNb_2O_6$ and $(Na_x\ K_{1-x})_2(Sr_{1-y}Ba_y)_4Nb_{10}O_{30}$.

The reasoning behind the selection of the two bronze families for new model studies were as follows:

1. In the $Pb_{1-x}Ba_xNb_2O_6$ family

   a. The morphotropic boundary occurring at compositions near x = 0.4 (next section) suggests that the relative stability of ferroelectric ordering along and orthogonal to the 4-fold axis is sensitive to the x value.

   b. If θ_1 is a continuously changing function of (1-x), then it should be possible to find crystals with very high ε_{11} and d_{15} in this family.

   c. By combining compositions in the two families, we should be able to design materials in which we can choose the values of θ_1 and θ_3, the most important parameters in the Gibbs function.

2. In the $(Na_xK_{1-x})_2(Sr_{1-y}Ba_y)_4NB_{10}O_{30}$ family

   a. At the 2/4 ratio chosen, the valence is such that all the larger A_1 and A_2 sites must be filled. Thus, the ratios x and y may be modified without changing fractional occupation of A_1 or A_2.

   b. There is some evidence that fully stuffed structures of this type may have lower dielectric and elastic losses.

   c. The domain structure in this crystal can now be readily revealed by etching.

A discussion of the growth and characterization of these materials can be found in Section 4.0 of this report.

3.7 Summary

The objective of the modelling studies was to develop the capability to predict the dielectric, piezoelectric and elastic compliances and their temperature behavior for a wide range of bronze structure ferroelectrics. The method chosen was an extension of the Landau:Ginsburg:Devonshire phenomenology which permits the full three dimensional description of the ferroelectric single domain properties in terms of a limited family of tensor coefficients of the prototypic paraelectric high temperature phase.

The thermodynamic method has for the first time made it possible to predict in a semi-quantitative manner the temperature dependence of property tensors for a system where the structure is much too complicated to permit atomistic calculations. It will be important to extend these studies in the future to other parameters such as the electro-optic r_{ijk} and g_{ijkl} constants and confirm more fully the manner in which the prototypic constants mutate with major cation substitutions.

4.0 BULK SINGLE CRYSTAL GROWTH AND CHARACTERIZATION

4.1 Single Crystal Growth of $Sr_{0.61}Ba_{0.39}Nb_2O_6$ Composition

The Czochralski single crystal growth technique has been successfully developed to produce large size single crystals of the ferroelectric composition $Sr_{0.61}Ba_{0.39}Nb_2O_6$. Although both the end members $SrNb_2O_6$ and $BaNb_2O_6$ do not belong to the tungsten bronze family, the solid solution, $Sr_{1-x}Ba_xNb_2O_6$, where $0.25 < x < 0.75$, crystallized in the tetragonal tunsten bronze structure. Figure 13 shows the limit of solid solution range for the three different phases, e.g., $SrNb_2O_6$, $BaNb_2O_6$ and $Sr_{1-x}Ba_xNb_2O_6$ and variation of the ferroic transition temperture for the trunsten bronze solid solution. The tungsten bronze solid solution has been found to be very useful for several device applications since it exhibits the largest electro-optic[5] and pyroelectric[6] coefficients of any well behaved materials. According to the theoretical work by Cross, the $Sr_{1-x}Ba_xNb_2O_6$ solid solution possesses temperature compensated orientations.

Most recent work by Megumi et al.[7] indicates that the composition $Sr_{0.61}Ba_{0.39}Nb_2O_6$ is the only congruently melting composition of the entire series. Figure 14 shows the composition shifts from melt to crystal for the various compositions in the $SrNb_2O_6$-$BaNb_2O_6$ binary system. It is clear from this diagram that the composition $Sr_{0.61}Ba_{0.39}Nb_2O_6$ should be suitable for the production of striation free single crystals of SBN. The composition $Sr_{0.61}Ba_{0.39}Nb_2O_6$ was selected in the present work and the growth parameters have been established. Reports in the literature have described a spattering problem when initially adding starting materials to the crucible for melting. This problem has been essentially eliminated by pre-heating the starting material just below the melting temperature. The $Sr_{0.61}Ba_{0.39}Nb_2O_6$ composition melts around 1510°C and one can use either platinum or iridium crucibles for the crystal growth work. A schematic diagram of a typical Czochralski crystal growth apparatus is shown in Fig. 15.

Although this process is now well established, the growth of multicomponent bronze systems is, in general, difficult, and success depends

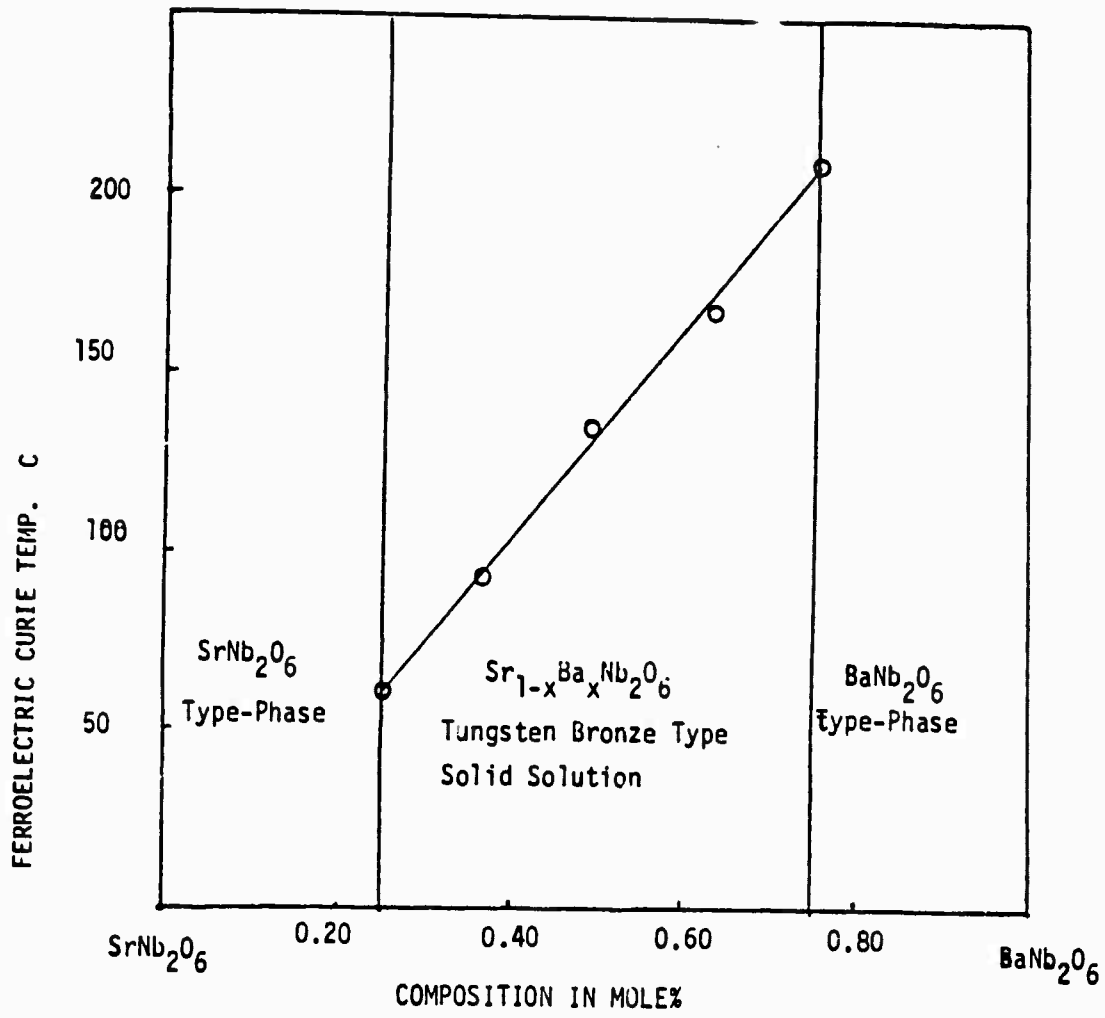

Fig. 13 Phase boundary and Curie temperature vs composition for $Sr_{1-x}Ba_xNb_2O_6$.

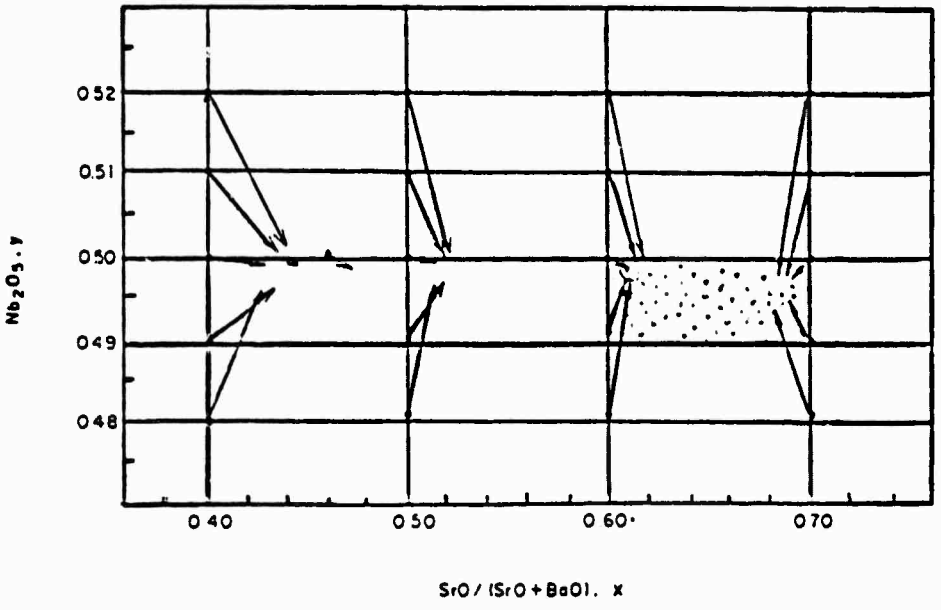

Fig. 14 Composition shift from melts to crystals. Dotted area: area containing congruent melting composition of SBN.

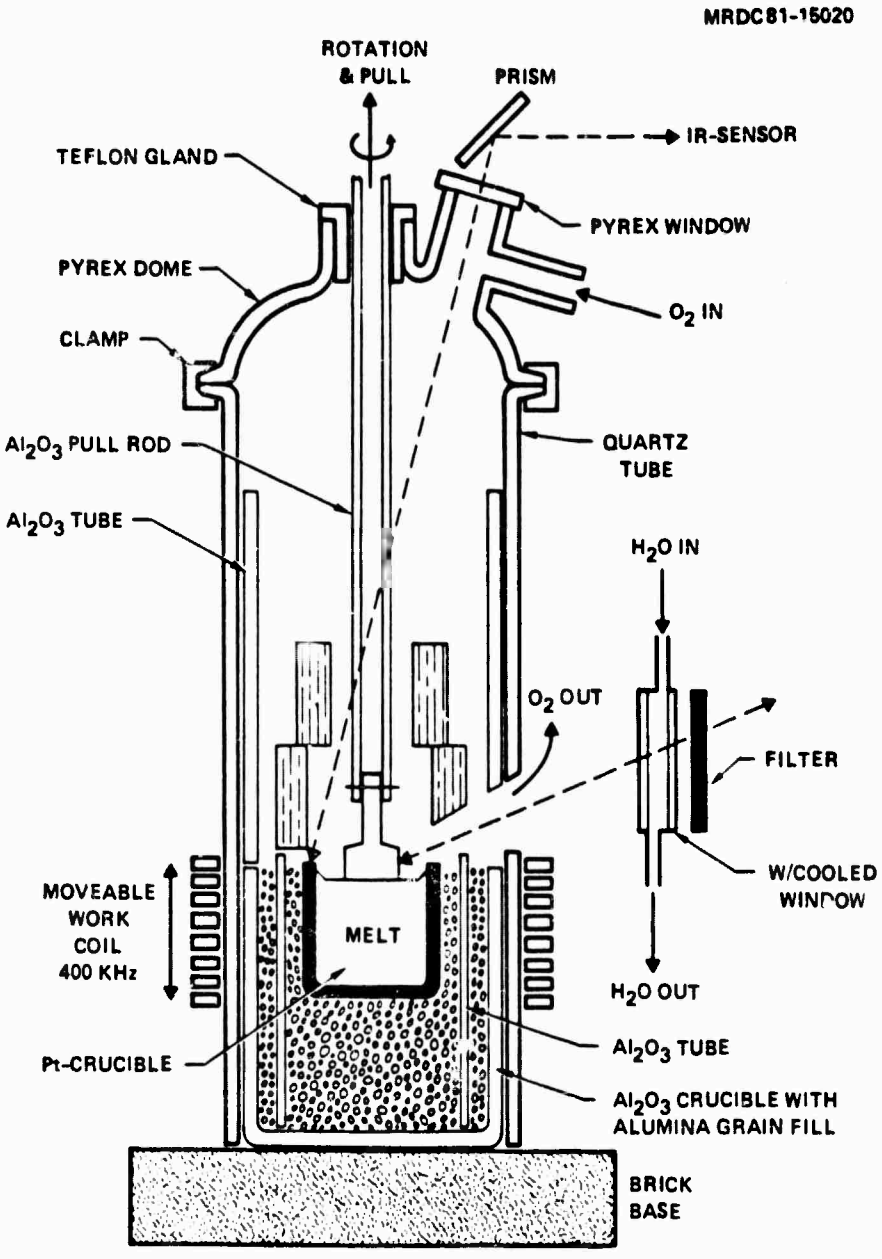

Fig. 15 A schematic diagram of a typical Czochralski crystal growth apparatus.

strongly on the ability to control the diameter of crystal and the thermal gradient in the crystal near the solid-liquid interface. During the past six months, considerable effort has been made to increase the diameter of SBN single crystals, and it was found possible to grow single crystals of one inch in diameter. Beyond this limit, however, growth was found to be difficult and the crystals tended to crack because of stiff thermal gradients in the crystals. Optimum growth conditions used for one inch diameter crystals are as follows:

Pulling Rate	8 - 10 mm/hr
Rotation Rate	20 - 30 rpm
Growth Direction	Along the c-axis
Growth Temperature	1500 - 1510°C
Atmosphere	Oxygen for platinum crucible

Fracture free and optically good quality single crystals, approximately one inch in diameter and two inches long, have been produced. Crystals are pale yellow color, but become deep yellow when the crystal diameter is greater than 1.5 cm. Crystals were also pulled along other directions and under different experimental conditions. However, it was found difficult to obtain large crystals in the other directions. Crystals pulled along the c-axis are of excellent quality and have facets with clearly defined faces. As shown in Fig. 16, SBN single crystals show 24 faces of four prisms: (110), (120), (100), and (130). Faces of the (100) and (110) forms are best developed on crystals with high strontium content. Using these two forms, the SBN single crystals can be oriented with a minimum of difficulty. Optically, the $Sr_{0.61}Ba_{0.39}Nb_2O_6$ single crystals appear to be of good quality and are clear and transparent. These crystals show a room temperature tungsten bronze tetragonal structure and, according to the structural refinements for $Sr_{0.75}Ba_{0.25}Nb_2O_6$ crystals, this solid solution belongs to the point group 4 mm. Lattice parameter measurements for ceramic and single crystal samples of the $Sr_{0.61}Ba_{0.39}Nb_2O_6$ composition give values of a = 12.451Å and c = 3.938Å, which are in close agreement with the values a = 12.461Å and c = 3.936Å reported by Megumi et al.[7] for the same composition.

ERC80-9419

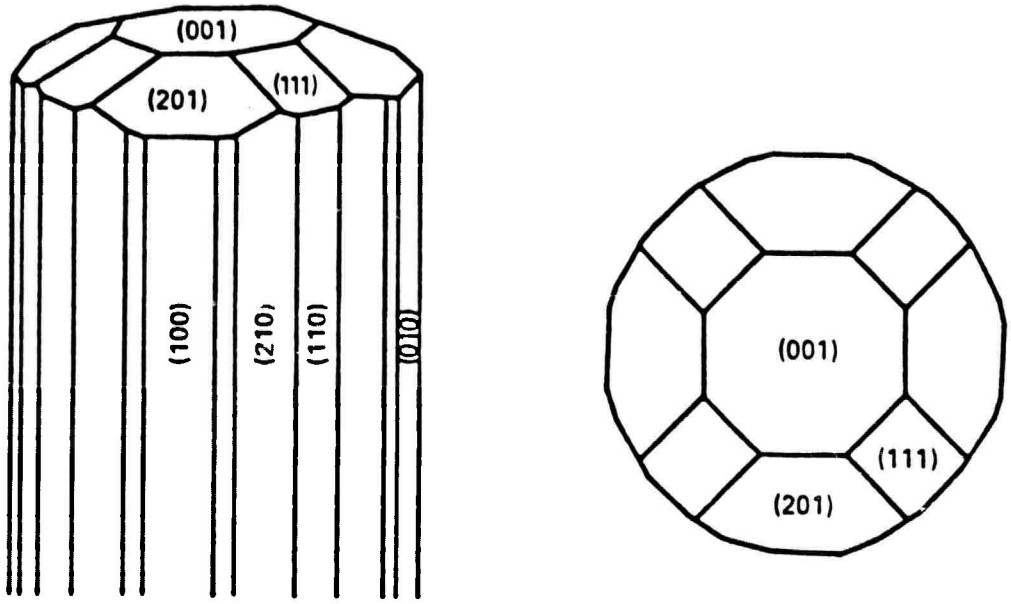

Fig. 16 Idealized form of SBN single crystals.

4.2 SBN Characteristics

The purpose of the present investigation is to develop suitable temperature-compensated tetragonal tungsten bronze compositions that possess a high SAW electromechanical coupling coefficient (K^2) with a sufficiently low temperature coefficient of SAW velocity. Since the tungsten bronze structural family embraces some 100 or more known compounds and several solid solution systems, the possibility of developing a suitable composition for SAW application is very significant. Bronze compositions such as $PbKNb_5O_{15}$ (PKN), $Ba_2NaNb_5O_{15}$ (BNN), etc., have been proven to possess very attractive characteristics for SAW device applications, but these compositions have not found commercial use due to the extreme difficulty in obtaining suitable size single crystals. It is then natural to trade-off some of the properties for crystals which can easily be grown and modified according to device requirements. The tetragonal bronze $Sr_{1-x}Ba_xNb_2O_6$ solid solution was selected for this study because its piezoelectric properties and Curie temperature can be changed in the desired range. Although the values k_{15} (electromechanical coupling) and d_{15} (piezoelectric constant) for SBN are much smaller than those attainable in the best bronze compositions, SBN provides a model system for studying the composition dependence of the key quantities, and for verifying the predictive power of the phenomenological Devonshire theory for these systems. The present SBN:60 single crystals not only have provided such information, but these crystals can also be used as substrate material for other SBN and bronze compositions. This is a unique advantage in the present work and makes it possible to develop other interesting and desired bronze compositions for SAW device applications. Based on our phenomenological model, other bronze compositions such as $PB_{1-x}Ba_xNb_2O_6$ and $Ba_{2-x}Sr_xK_{1-y}Na_yNb_5O_{15}$ are potentially important since they exhibit high electromechanical coupling coefficients k_{15} and piezoelectric constants d_{15} similar to PKN.

Considerable effort has been made in evaluating the piezoelectric and acoustical characteristics of SBN:60 single crystals. As summarized in Table 11, surface acoustical measurements were performed on three different cuts, namely (100), (110) and (001) of the SBN:60 crystal. For the X and (110)

Table 11

Acoustical Characteristics of SBN:60 Single Crystals

Crystal Composition	SAW Electromechanical Coupling Constant (K^2)	SAW Velocity m/sec	Acoustical Losses†		Temp. Coeff. of SAW-Velocity, at Room Temperature
			Insertion	Attenuation	
SBN:60-(001) Plate Propagating along the 100 direction	180×10^{-4}	3300	17.4 dB	5.3 dB/cm	-50 to -140 ppm
SBN:60-(100) Plate* Propagating along the 001 direction	55×10^{-4}	3193	25.4 dB	0.8 dB/cm	
SBN:60-(110) Plate	60×10^{-4}	3173	23.7 dB	8.5 dB/cm	-18 ppm

*A zero temperature coefficient of SAW velocity was observed for this cut at + 10°C.
†All acoustical measurements were performed at 30.5 MHz.

cuts, propagation was along the (001) direction; for the Z-cut, propagation was along the (100) direction. Fifteen finger pair transducers were used, and periodicity was 104.4 μm. Transducer electrodes were photolithographically fabricated from aluminum films, approximately 1000A thick, by conventional wet etching techniques. Results of this work show that the tetragonal tungsten bronze composition SBN:60 possesses temperature-compensated orientations and it appears to be suitable for SAW device applications with some minor modifications in its present acoustical characteristics. The SAW electromechanical coupling (K^2) for three different cuts, (100), (110), and (001), of SBN:60 bulk single crystal has been established. This constant has been shown to be larger for the (001) plate propagating along the (100) direction and, as summarized in Table 11, its value is measured to be 180×10^{-4}. This value is much smaller than the best known piezoelectric Y-Z cut $LiNbO_3$ bulk single crystal (480×10^{-4}), but it is similar to the best known bronze composition $Pb_2KNb_5O_{15}$ (188×10^{-4}). The measurements on the other cuts such as (100) and (110) plates and propagating along the (001) direction were 55×10^{-4} and 60×10^{-4}, respectively. The

temperature coefficient of SAW velocity and acoustical losses for this composition have also been determined; these are also given in Table 11. It is interesting to note that both the orthorhombic PKN and the tetragonal SBN crystals exhibit similar acoustical characteristics, even though their piezoelectric properties are different; specifically, the coupling constant k_{15} = 0.69 and the piezoelectric constant d_{15} = 470 are substantially larger for PKN than for SBN or any other bronze composition. The PKN crystal also shows anomalous elastic constant temperature coefficients, which lead to the existance of ZTCD-cuts for SAWs. These cuts possess values of K^2 up to 188 × 10^{-4}, while their time-bandwidth products are 0.6 × 10^{-4} sm^{-1}, which are similar to those given for $LiNbO_3$. This makes PKN very promising for SAW device applications; however, this crystal has not found commercial use because of extreme difficulty in obtaining suitable size crystals for such applications. On the other hand, the bulk single crystal growth of the temperature compensated SBN:60 composition (one inch in diameter) has successfully been shown by the present authors, and as such, there is possibility that this composition can be used with some modification or it can be used as substrate material for other suitable compositions which exhibit desired acoustical characteristics. The latter approach, LPE, has already proven successful not only for the SBN:60 composition, but for other compositions such as $Sr_2KNb_5O_{15}$ (hetero-epitaxial growth).

As summarized in Table 11, the insertion and attenuation losses for the SBN:60 single crystal have also been established, and they appear to be substantially higher than for other important piezoelectric materials such as $LiNbO_3$, $LiTaO_3$, PKN, etc. Similar SAW measurements or the other bronze compositions SBN:50 and SBN:75 within the $Sr_{1-x}Ba_xNb_2O_6$ solid solution system have been made by Uchica et al.,[8] and their results show that these losses (for SBN:50, insertion loss 5 dB, attenuation loss 0.2 dB/cm) for the other two compositions are considerably lower order than the SBN:60 crystals. Since the SBN:60 composition is located between the other two compositions in the $SrNb_2O_6$-$BaNb_2O_6$ binary system, it was expected that thse losses should be of the same order for the SBN:60 composition. In order to establish this result more conclusively,

efforts have been made to improve the materials characteristics and growth conditions. Since the SBN:60 composition melts congruently in the binary system $SrNb_2O_6$-$BaNb_2O_6$, it is expected that the quality of the SBN:60 crystal should be better than any other composition within the $Sr_{1-x}Ba_xNb_2O_6$ solid solution range. We have now developed the SBN:60 single crystals from the melt containing ultrapure starting materials which produce crystals of high quality.

4.3 Other Bronze Compositions: PBN and BSKNN

In addition to the work on SBN, piezoelectric measurements on the other important temperture compensated bronze compositions such as $Sr_{0.5}Ba_{0.5}Nb_2O_6$, $Sr_2KNb_5O_{15}$, $Pb_{1-x}Ba_xNb_2O_6$, $Ba_{2-x}Sr_xK_{1-y}Na_yNb_5O_{15}$, etc. have also been performed. As summarized in Table 12, the coupling constant k_{15} and the piezoelectric constant d_{15} are significantly higher, specifically for the $Pb_{1-x}Ba_xNb_2O_6$ and $Ba_{2-x}Sr_xK_{1-y}Na_yNb_5O_{15}$ solid solution systems, and based on our phenomenological model developed for this tungsten bronze family such compositions should exhibit good acosutical properties with minimum insertion and attenuation losses. The preliminary bulk single crystal growth work on these compositions (at Rockwell and Penn State) has already shown that small to medium size crystals, approximately 5-15 mm in diameter, can be grown for piezoelectric characterization.

Earlier studies have shown that to improve the piezoelectric coupling, particularly d_{15} and k_{15}, it would be desirable to move into a composition field in the bronze structure where the transverse Curie temperature θ_1 could be enhanced so as to improve ε_{11} and consequently d_{15} and k_{15}.

It has been shown from earlier ceramic studies that in the solid solution family $(Pb_{1-x}Ba_x)Nb_2O_6$ there is a morphotropic phase boundary occurring between a ferroelectric orthorhombic (mm2) and a ferroelectric tetragonal (4 mm) structure near the composition $Pb_{0.6}Ba_{0.4}Nb_2O_6$. From the phase diagram (Fig. 17) it is evident that in $PbNb_2O_6$ the transverse Curie point θ_1 is greater than θ_3. With introduction of Ba^{2+} in the solid solution the value of θ_1 decreases, until it crosses over with θ_3 near the 60:40 composition. Extrapolating θ_1 into the

Table 12
Important Piezoelectric Tungsten Bronze Compositions for SAW Applications

Property	$Pb_2KNb_5O_{15}$ (PKN)	$Ba_2NaNb_5O_{15}$ (BNN)	$Sr_{0.6}Ba_{0.4}Nb_2O_6$ (SBN)	$K_3Li_2Nb_5O_{15}$ (KLN)	$Sr_2KNb_5O_{15}$ (SKN)	$Pb_{1-x}Ba_xNb_2O_6$ (PBN)	$Ba_{1.2}Sr_{0.8}K_{0.75}Na_{0.25}Nb_5O_{15}$ (BSKNN)
Electromechanical Coupling	--						
Constant k_{33}	--	0.45	0.45	0.52	0.45	--	0.47
k_{15}	0.69	0.12	0.24	0.34	0.30	--	0.28
k_{24}	0.73	0.25	--	--	--	--	--
Piezoelectric Constant							
(10^{-12} C/N) d_{33}	62	32	130	57	--	110	--
d_{15}	470	45	31	68	--	250	--
d_{24}	470	--	--	--	--	--	--
SAW-Electromechanical Coupling Constant (K^2)	188×10^{-4}	--	180×10^{-4}	--	--	--	--
Temperature Coefficient of SAW Velocity	Y-cut, +24 ppm Z-cut, -30 ppm	Close to α-quartz	Z-cut, -50 ppm (110), -18 ppm	--	--	--	--
Crystal size†	Small	Small	Large	Small	Medium	Medium	Medium
Curie Temperature (°C)	460	560	72	405	156	345	203
Crystal Symmetry	Ortho T.B.*	Ortho T.B.	Tetra T.B.	Tetra T.B.	Tetra T.B.	Tetra T.B.	Tetra T.B.
References (by No.)	9-10	11		12			13

*T.B. - Tungsten Bronze Structure
†Small - ≤ 1 cm.
Medium - ~ 1 to 1.5 cm
Large - 2 to 3 cm.

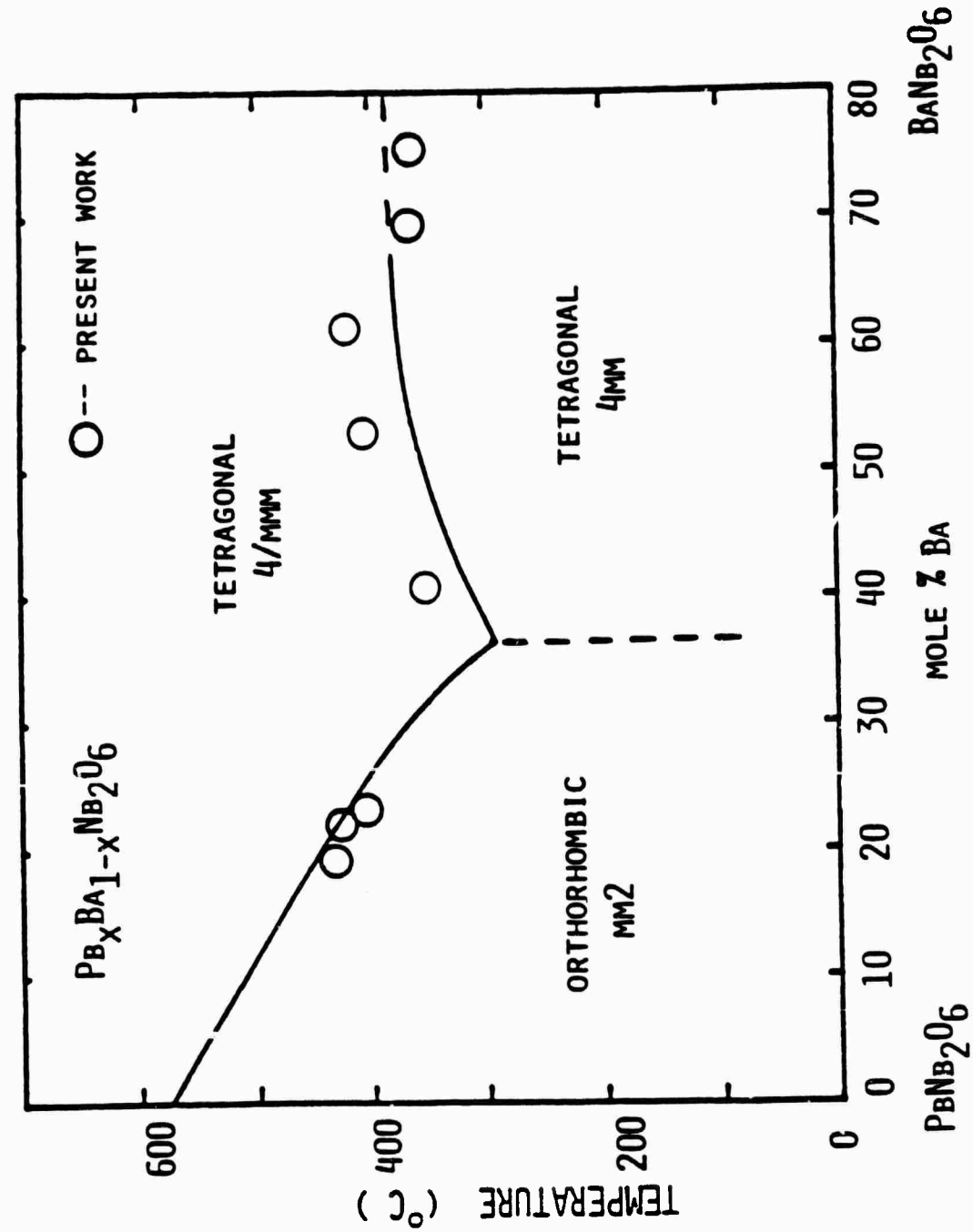

Fig. 17 Phase diagram for ferroelectricity in the solid solution system $Pb_xBa_{1-x}Nb_2O_6$.

composition beyond 40% barium niobate there should be a regimen close to the morphotropic composition in which the tetragonal form is the stable phase, but in which θ_1 is large and therefore the transverse mode of polarization soft.

To confirm the expected behavior we have grown single crystals of $Pb_xBa_{1-x}Nb_2O_6$ at the compositions indicated by open circles in Fig. 17 and in Table 1. Growth was by the Czochralski method and the initial aim was to obtain crystals of a sufficient size to characterize dielectric and piezoelectric properties. To obtain suitable samples it was necessary to enhance the PbO content of the melt, and in each case the final composition was determined by chemical analysis from the tip and the base of the boule. For each composition, density was measured by picnometer method, lattice spacing by powder x-ray methods. The Curie temperatures were determined from a dielectric measurement at 1 kHz. These parameters are listed in Table 13.

For electrical characterization, plate shaped samples with major surfaces normal to the a and c axes of the tetragonal prototype were cut from crystals with $x > 0.4$. Electrodes of chrome-gold were evaporated onto the major surfaces, and the 'c' plates poled using a field of 10 kv/cm at room temperature. For the compositions in the ferroelectric rhombohedral field the samples were cut with major faces normal to c, but for a and b cuts, with major faces making an angle of 45° to the tetragonal a axes. To achieve poling in the orthorhombic phase it was necessary to apply mechanical pressure to the major faces so as to reorient the ferroelastic twin structure. After poling to a single domain state dielectric permittivities were measured as a function of temperature under heating conditions.

Principal permittivities measured at 1 kHz for the orthorhombic bronze $Pb_{0.87}Ba_{0.20}Nb_{1.97}O_6$ are shown in Fig. 18. The high and increasing value of K_c confirms the tendency to stabilize the tetragonal Curie temperature θ_3.

In the tetragonal field at the composition $Pb_{0.6}Ba_{0.42}Nb_{1.99}O_6$, the temperature dependence of the weak field permittivity is given in Fig. 19. It may be noted that in this case K_A is large and increasing towards low temperature expressing, as expected, the enhanced value of θ_1 for this composition.

Table 13

Properties of $Pb_xBa_{1-x}Nb_2O_6$ Crystals

Composition	Density p(g/cc)	Lattice Parameters (Å) a	b	c	T_c (°C)	Dielectric Constants K_a	K_b	K_c	Piezo Coeff. (x 10^{-12} C/N) d_{33}	d_{15}	Pyroelectric Coeff. (x 10^{-4} c/m²°C) p
1. $Pb_{0.33}Ba_{0.7}Nb_2O_6$	5.65	12.447		3.995	350	360		140	60	50	1.7
2. $Pb_{0.24}Ba_{0.69}Nb_{2.03}O_6$		12.509		3.975	350	360		140	60	50	1.7
3. $Pb_{0.48}Ba_{0.44}Nb_{2.03}O_6$	5.93	12.493		3.478	407						
4. $Pb_{0.37}Ba_{0.53}Nb_{2.05}O_6$		12.486		3.98	425	630		70			
5. $Pb_{0.6}Ba_{0.42}Nb_{1.99}3O_6$	6.00	12.495		3.989	345	1600		200	110	250	0.9
6. $Pb_{0.87}Ba_{0.20}Nb_{1.97}O_6$	6.3	17.67	17.92	3.89	430	1200	225	1900	70	500	2.2

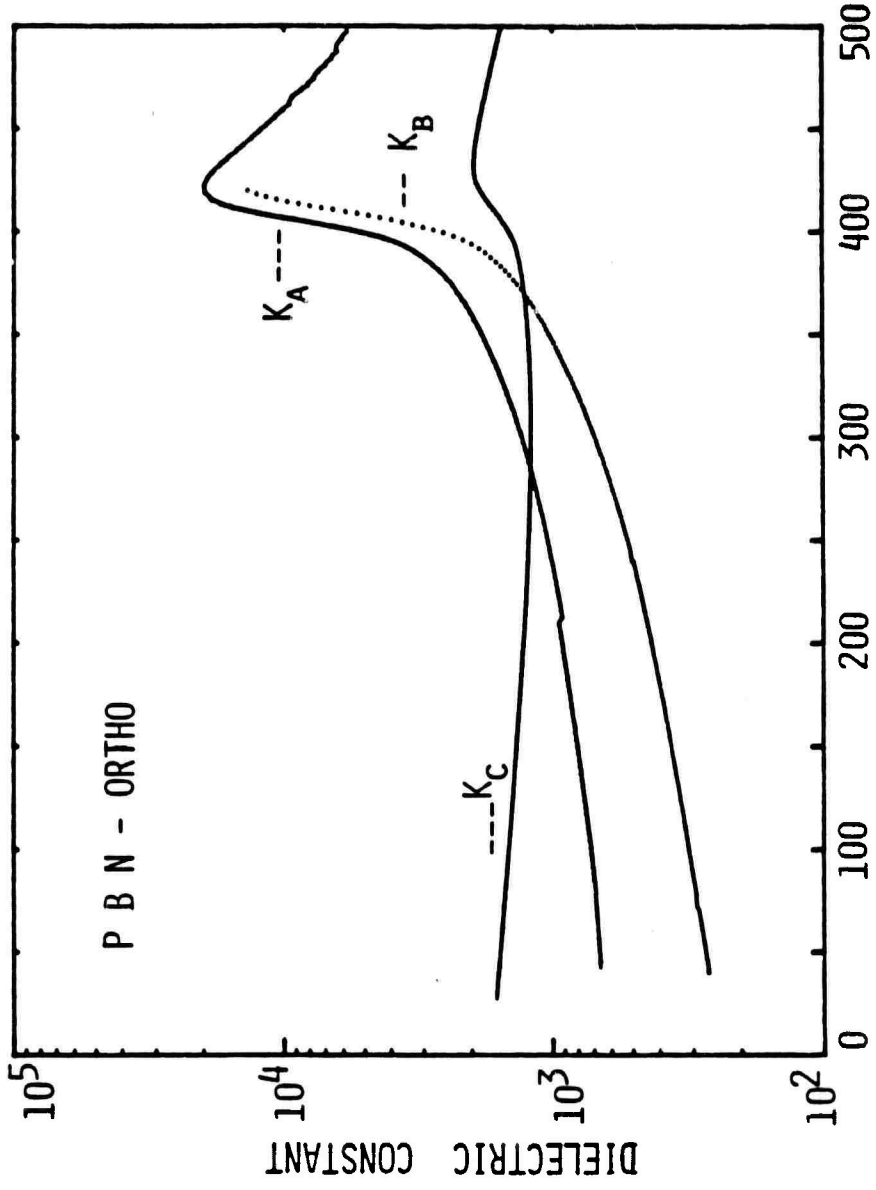

Fig. 18 Weak field dielectric permittivity as a function of temperature in $Pb_{0.87}Ba_{0.2}Nb_{1.97}O_6$.

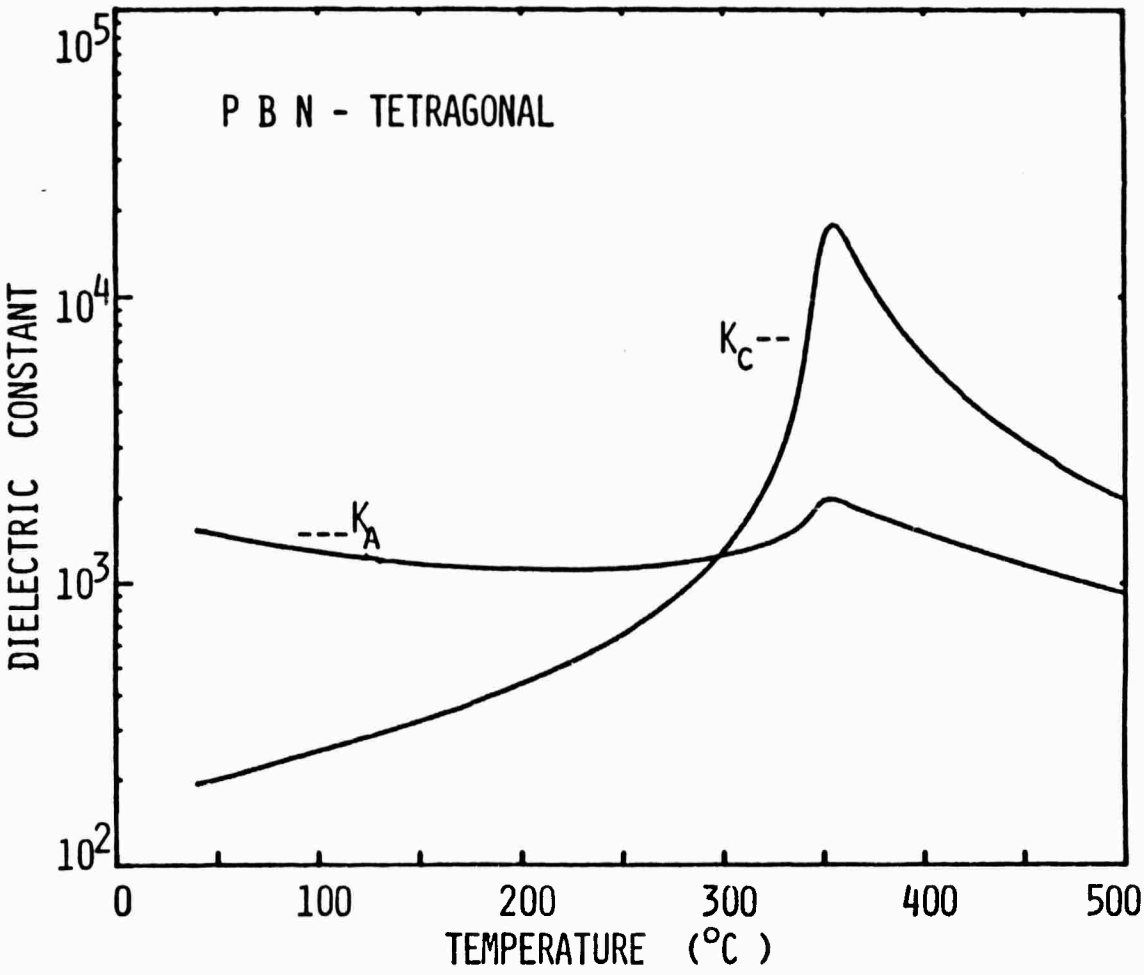

Fig. 19 Weak field permittivity as a function of temperature in a single domain $Pb_{0.6}Ba_{0.42}Nb_{1.99}O_6$ crystal.

To confirm the expected effects from the enhanced dielectric responses, the piezoelectric coefficients d_{33} and d_{15} were measured by resonance methods (Fig. 20). As predicted from the phenomenology, d_{15} rises sharply as the composition approaches the morphotropic boundary. For completion of the electrical data the pyroelectric coefficient p_3 was also measured (Fig. 21).

These electrical data for single domain single crystals in the $Pb_xBa_{1-x}Nb_2O_6$ solid solution system confirm that the permittivity K_1 and the piezoelectric constant d_{15} can be strongly enhanced in compositions close to the morphotropic phase boundary in the region of the $Pb_{0.6}Ba_{0.4}Nb_2O_6$ composition.

In addition to the work on PBN, results on the tungsten bronze composition $Ba_{1.2}Sr_{0.8}K_{0.75}Na_{0.25}Nb_5O_{15}$ also look very promising. As can be seen in Fig. 22 we have been able to grow medium size crystals of BSKNN which have good electrical and optical properties, although further refinement in the crystal growth needs to be done to minimize crystal strain and cracking. The higher transverse Curie temperature for this composition (203°C) as compared to SBN indicates a larger value of the piezoelectric constant d_{15}, and therefore improved piezoelectric coupling. Crystal samples of this material have been successfully poled in air while cooling slowly from just above T_c with fields up to 7.5 kv/cm. The results for the electromechanical coupling constants k_{15} and k_{33} are given in Table 12 and look very encouraging. We will be continuing our efforts in the area of BSKNN crystal growth, and we anticipate further improvement in the crystal quality and the electromechanical, dielectric, and piezoelectric properties of this material.

In addition to the materials already discussed, Rockwell International and Penn State University are also actively involved in the growth and evaluation of other tungsten bronze and perovskite materials for a wide variety of applications. A list of presently available materials is given in Table 14.

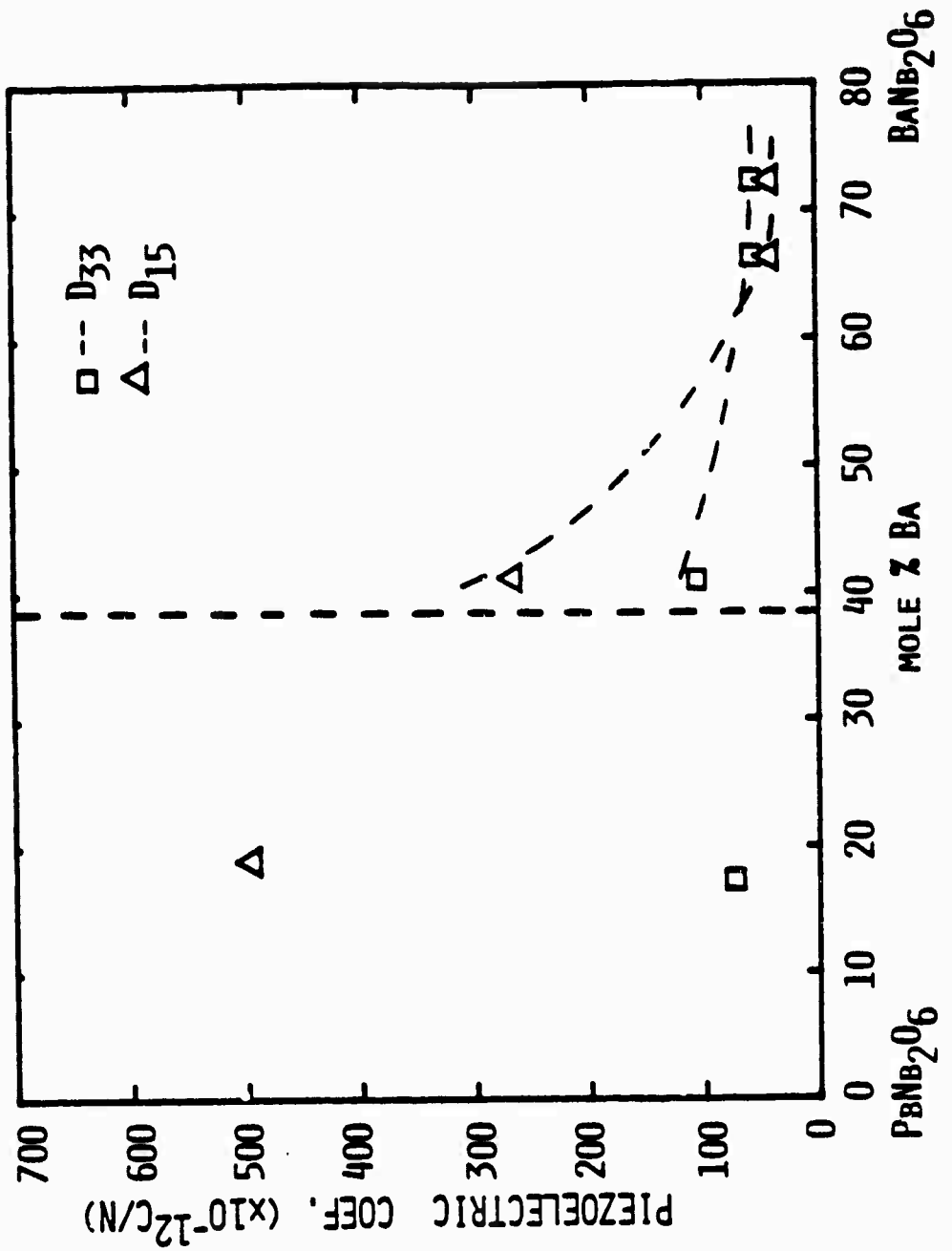

Fig. 20 Piezoelectric constants at room temperature as a function of composition in $Pb_xBa_{1-x}Nb_2O_6$ solid solutions.

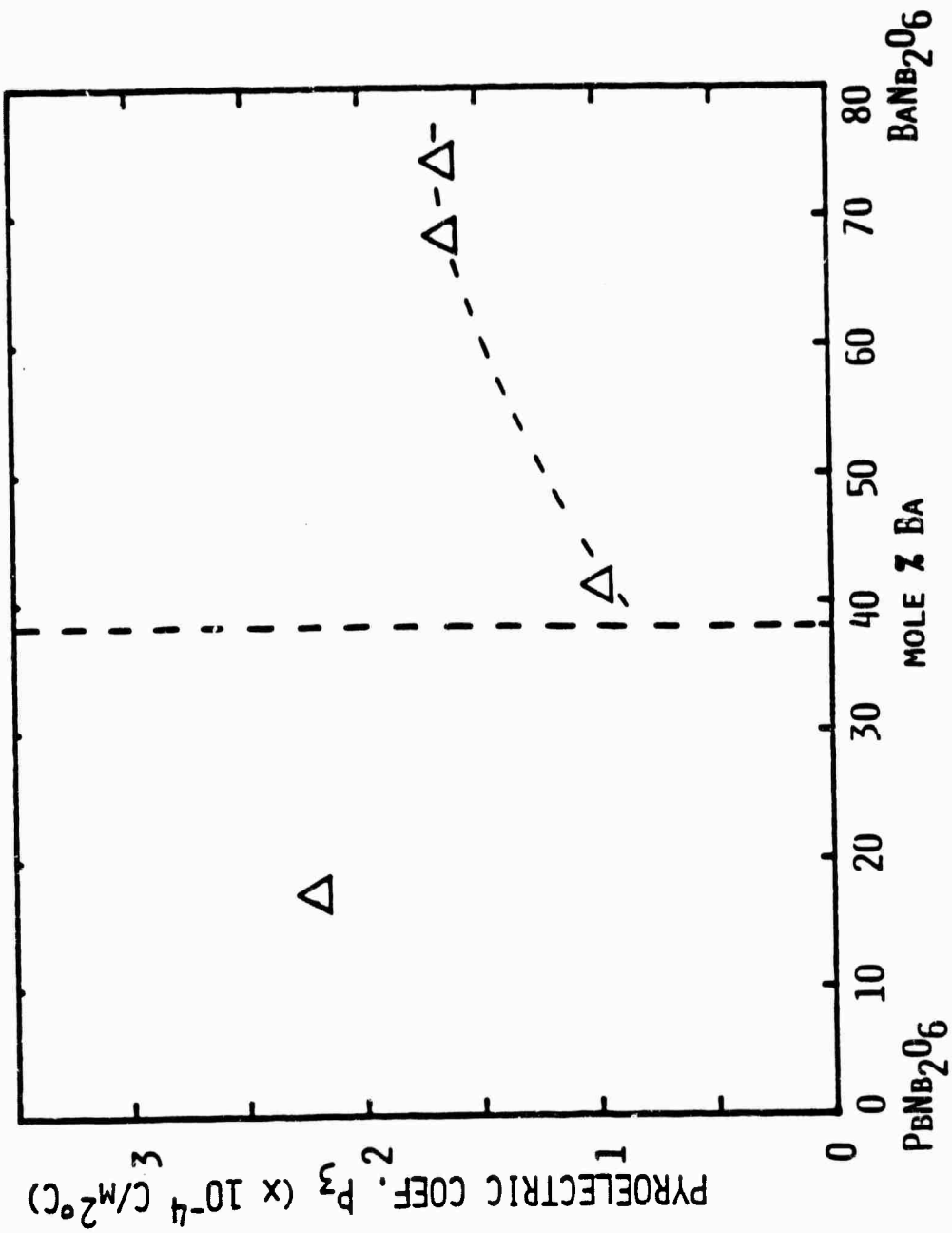

Fig. 21 Pyroelectric constants at room temperature as a function of composition in $Pb_xBa_{1-x}Nb_2O_6$.

MRDC78-3045

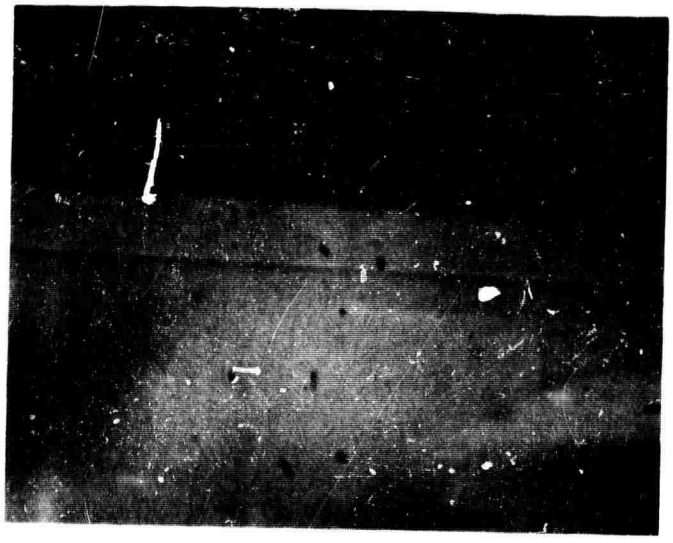

Fig. 22 Czochralski grown $Ba_{1.2}Sr_{0.8}K_{0.75}Na_{0.25}Nb_5O_{15}$ single crystals.

Table 14

List of Available Materials

1.	TUNGSTEN BRONZE FAMILY COMPOSITIONS		
	• $Sr_{1-x}Ba_xNb_2O_6$, x = 0.60, 0.50, and 0.75		DARPA Sponsorship
	• $K_3Li_2Nb_5O_{15}$		AFOSR-DARPA Sponsorship
	• $Sr_2KNb_5O_{15}$		ONR-DARPA Sponsorship
	• $Pb_{1-x}Ba_xNb_2O_6$		DARPA Sponsorship (Penn State)
	• $Ba_{2-x}Sr_xK_{1-y}Na_yNb_5O_{15}$		DARPA Sponsorship (Penn State)
2.	PEROVSKITE STRUCTURAL FAMILY COMPOSITIONS		
	• $KTa_{1-x}Nb_xO_3$ (KTN)	Single crystal & hot pressed ceramics	Rockwell and Penn State
	• Pb_2ScNbO_6	Hot pressed ceramics	Penn State
3.	OTHER IMPORTANT COMPOSITION		
	• SbSI	Single crystal & hot pressed samples	Penn State

5.0 LIQUID PHASE EPITAXIAL GROWTH OF TUNGSTEN BRONZE FAMILY COMPOSITIONS

The purpose of the liquid phase epitaxial (LPE) growth work is to develop and modify suitable tungsten bronze compositions that possess high SAW electromechanical coupling constants (K^2) with sufficient low temperature coefficient of SAW velocity. The ability of LPE to obtain a wide variety of films in a relatively short time, compared with the time required to achieve suitable quality in bulk single crystals, has enabled us to greatly expand our knowledge of obtainable properties in this class of materials. Since large size single crystals of bronze compositions $Sr_{1-x}Ba_xNb_2O_6$, where x = 0.60 and 0.50, are now available from our current work and, secondly, since the LPE growth of $Sr_{0.5}Ba_{0.5}Nb_2O_6$ has been shown to be successful, this approach seems to be most exciting for the further development of either simple or complex bronze compositions for SAW device applications. It is interesting to note that the bronze single crystals $Sr_{0.60}Ba_{0.40}Nb_2O_6$ have already been shown to be temperature-compensated, with great promise for device applications. Although these results are encouraging, it is important to continue to improve the quality and properties by improving the material characteristics. This can be achieved through further development of LPE layers of different compositions, and thereby obtain optimum compositions for SAW device applications. Based on our phenomenological model developed for the bronze family, the piezoelectric d_{33} and d_{15} (or e_{33} and e_{15}) and electromechanical coupling constants k_{33} and k_{15} play important roles, and their values should be large to achieve better temperature compensation in piezoelectric material. The bronze compositions bsed on the tetragonal solid solution $Pb_{1-x}Ba_xNb_2O_6$, $KNbO_3$-$SrNb_2O_6$ (e.g., $Sr_2KNb_5O_{15}$), etc. exhibit excellent piezoelectric characteristics and appear to be promising candidates for SAW device applications.

5.1 Growth of $Sr_{0.5}Ba_{0.5}Nb_2O_6$ Thin Films

The LPE growth technique has succesfsully been developed for the bronze composition $Sr_{0.5}Ba_{0.5}Nb_2O_6$ by using the BaV_2O_6 solvent The system BaV_2O_6-$Sr_{1-x}Ba_xNb_2O_6$ has been studied in great detail and, as shown in Fig. 23, the

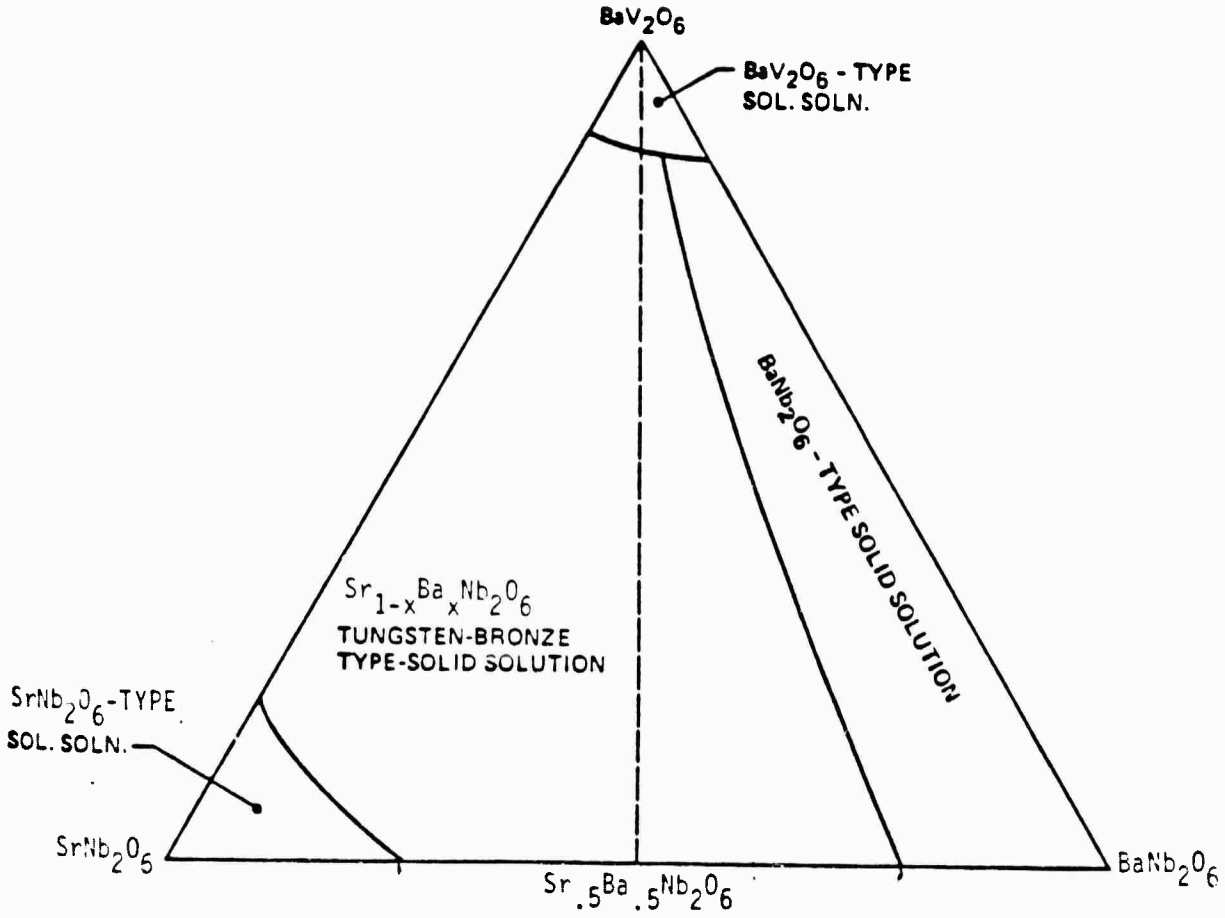

Fig. 23 The system BaV_2O_4-$SrNb_2O_6$-$BaNb_2O_6$ in air at 1200°C.

tungsten bronze SBN composition extends over a wide compositional region. The composition represented along the binary join BaV_2O_6-$Sr_{0.5}Ba_{0.5}Nb_2O_6$ has been used for LPE growth and has proven useful for developing films of composition $Sr_{0.46}Ba_{0.54}Nb_2O_6$.

Table 15 summarizes the results of the LPE growth experiments for the $Sr_{0.5}Ba_{0.5}Nb_2O_6$ thin films grown onto the $Sr_{0.6}Ba_{0.4}Nb_2O_6$ substrates. The films thus grown, specifically onto the (100)- and (110)-plates, are of excellent quality and are quite smooth. Although the surface quality is acceptable, continuous efforts are being made to improve the quality of the films. This task is being accomplished either by dipping the substrate at relatively higher temperatures (10°C) or by polishing the surfaces of the grown films. Both approaches seem to be suitable, and it is therefore anticipated that surface quality will not be a major problem in the future.

5.2 Growth of $Sr_2KNb_5O_{15}$ Thin Films

$SrKNb_5O_{15}$ (SKN) belongs to the tetragonal tungsten bronze structural family; it is ferroelectric, with Curie temperature (T_c) around 160°C. The crystal of this composition exhibits excellent dielectric, piezoelectric and electro-optic properties, which suggests possible applications for surface acoustic wave and electro-optic device applications. The single crystal growth of this composition is known and reported by various workers including the present authors. Although single crystal growth of the SKN composition is possible, the technique is confined to producing relatively small size crystals, approximately 5 - 6 mm in diameter. The growth of tungsten bronze compositions, in general, is difficult and success depends strongly on the ability to control the diameter of the crystal and the thermal gradient in the crystal near the solid-liquid interface. An alternative approach to this problem is LPE-grown thin films for SAW application, since the lattice mismatch between the SBN and SKN compositions is minimal and SBN single crystals of one inch in diameter are now available for such study. Table 16 summarizes the physical characteristics of SBN and SKN compositions.

Table 15

Epitaxial Growth Conditions for the Tungsten Bronze $Sr_{0.5}Ba_{0.5}Nb_2O_6$ Composition

Composition	Solvent	Substrate Orientation	Film Thickness (μm)	Quality	Problems
$Sr_{0.5}Ba_{0.5}Nb_2O_6$	BaV_2O_6	SBN:60, (001)	20 - 60	Good	Slight mismatch
$Sr_{0.5}Ba_{0.5}Nb_2O_6$	BaV_2O_6	SBN:60, (100)	15 - 35	Excellent	None
$Sr_{0.5}Ba_{0.5}Nb_2O_6$	BaV_2O_6	SBN:60, (110)	15 - 35	Excellent	None
$Sr_{0.5}Ba_{0.5}Nb_2O_6$	BaB_8O_{13}	SBN:60, (001)	10 - 15	Moderate	Flux-problem*
$Sr_{0.5}Ba_{0.5}Nb_2O_6$	BaB_8O_{13}	SBN:60, (100)	10 - 215	Good	Flux-problem

*Flux stays on substrate after growth, however, it can be washed away in dil. acids.
SBN:60 corresponds to $Sr_{0.6}Ba_{0.4}Nb_2O_6$ - composition.

Table 16

Physical Properties of the $Sr_{1-x}Ba_xNb_2O_6$ and $Sr_2KNb_5O_{15}$ Compositions

Physical Constants	$Sr_{0.6}Ba_{0.4}Nb_2O_6$	$Sr_{0.5}Ba_{0.5}Nb_2O_6$	$Sr_2KNb_5O_{15}$
Structural Family	Tungsten Bronze	Tungsten Bronze	Tungsten Bronze
Symmetry	Tetragonal	Tetragonal	Tetragonal
Point Group	4 mm	4 mm	4 mm
Lattice Constants	a = 12.462 Å c = 3.938 Å	12.480 Å 3.952 Å	12.470 Å 3.942 Å
Curie Temperture (°C)	72	125	156
Dielectric Constant K_{33} at room temperature	880	500	1200
Electromechanical Coupling Coefficients	k_{33} = 0.47 k_{31} = 0.14 k_{15} = 0.24	k_{33} = 0.48 k_{31} = 0.137 k_{15} = ---	k_{33} = 0.44 k_{31} = --- K_{15} = 0.26

Crucial to the success of this isothermal LPE-growth of SKN is an ability to supercool the solution without the occurrence of spontaneous nucleation. It is therefore necessary, before LPE can be performed, to find a suitable flux system (solvent) for the SKN composition. Based on our research work in this area, a large number of solvents such as KVO_3, $K_2B_2O_4$d, SrV_2O_6, SrB_8O_{13}, etc. have been identified for this composition, but the preferred choice is the solvent KVO_3. Since the V^{5+} cation has strong preference for the 4-fold coordinated site, the inclusion of V^{5+} in the SKN is ruled out. Further, the KVO_3 solvent melts at very low temperatures (540°C) and growth should therefore be possible at low temperature. The phase equilibria study for the system based on composition $K_5V_5V_{15}$-$SrKNb_5O_{15}$ has been established by the DTA technique. Figure 24 shows a partial phase diagram for this system. Although it is difficult to obtain a complete phase relation for such multicomponent systems, the information obtained from this diagram is adequate to initiate the LPE growth of SKN composition.

The mixture containing 75 mole % $K_5V_5O_{15}$ and 25 mole % $Sr_2KNb_5O_{15}$ has been selected, since this mixture melts at relatively low temperatures (1000°C) and has been found to be suitable to develop thin films of the composition $Sr_2KNb_5O_{15}$. The mixture was first calcined at 650°C for about 10 - 15 hr and then melted in a 100 cc platinum crucible. The crucible was then placed in the growth furnace. As shown in Fig. 25, the growth apparatus consists of a vertical furnace which can be controlled with an accuracy of ± 1/2 C. The mixture was kept heated overnight at 1250°C and, after achieving complete homogeneity, the molten solution was slowly cooled to the growth temperature, around 1000°C, at the rate of 10°C/hr. The (100), (110), or (001) oriented $Sr_{0.6}Ba_{0.4}Nb_2O_6$ substrate, positioned slightly above the melt in order to equilibriate with the solution temperature, was dipped into melt. An appropriate dipping temperature was around 1000°C. After the required time for the growth had elapsed, the sample was withdrawn from the melt and cooled very slowly to room temperature. The adhering flux was removed by dipping the substrate in dilute hydrochloric acid. The results of this investigation are similar to those observed for the growth of $Sr_{0.5}Ba_{0.5}Nb_2O_6$ composition on SBN substrates. In the present case, the growth was also much faster on the (001) plate, compared to the other

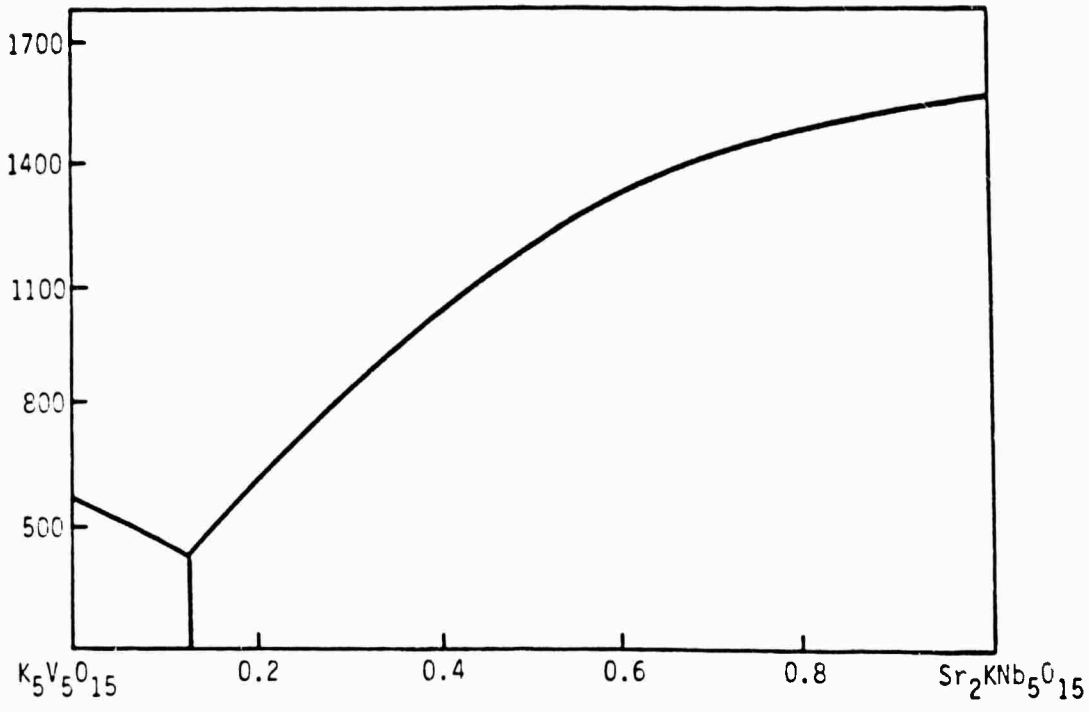

Fig. 24 Pseudo-binary phase diagram for the $K_5V_5O_{15}$-$Sr_2KNb_5O_{15}$ system.

MRDC81-15547

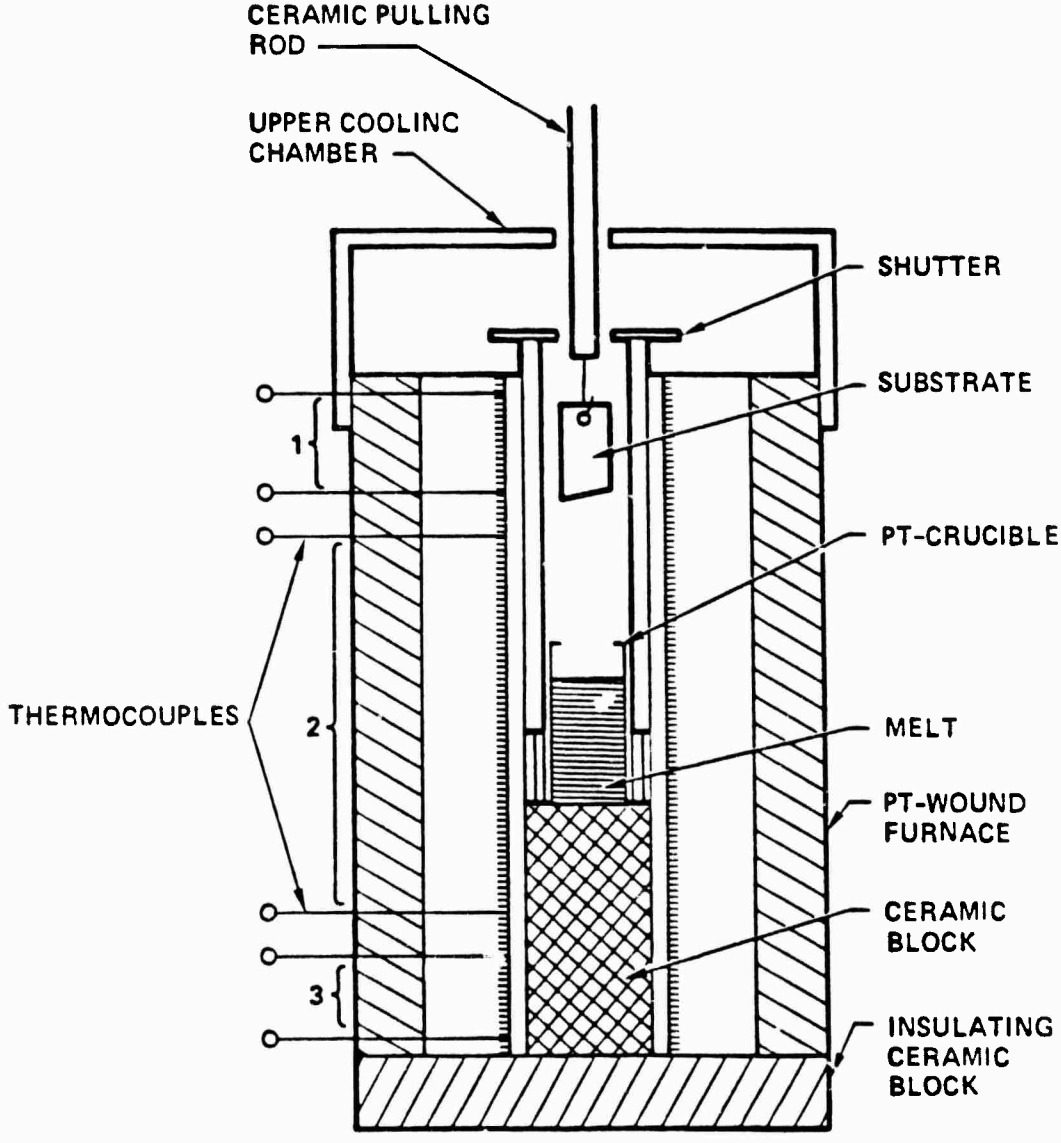

Fig. 25 LPE thin film growth furnace.

orientations. This is consistent with our observations on the bulk single crystal growth of the $Sr_2KNb_5O_{15}$ composition, where growth was only possible along the (001) direction. Figure 26 shows a typical cross-section of the SKN film grown onto the (001) plane; thickness of the film is approximately 20 μm. By using this technique, it was possible to grow films as thick as 25 - 30 μm, which is a significant accomplishment in the present work.

The films grown from KVO_3 flux are dark amber to yellow in color, depending on the film thickness, and the surface is smooth and clear. Microscopic examination at high magnification showed a slightly rougher aspect in the case of the thicker films. The crystallinity and film growth have been established by the x-ray diffraction technique. A typical intensity vs film thickness plot is given for the reflection (002) in Fig. 27. Two peaks corresponding to CuK α_1 and K α_2 represent the $Sr_{0.6}Ba_{0.4}Nb_2O_6$ substrates, while the SKN film position is denoted by CuK' α_1 and K' α_2. The intensity of film reflection was significantly stronger than that of the substrate, indicating the high degree of crystallinity as well as confirmation of the growth of the SKN layer on the SBN substrate.

Recently Adachi et al.[12] also demonstrated the successful heteroepitaxial growth of another bronze composition $K_3Li_2Nb_5O_{15}$ on the bronze $K_2BiNb_5O_{15}$ substrate material by the rf sputtering and LPE techniques. The $K_3Li_2Nb_5O_{15}$ films thus grown were shown to be of excellent quality and thickness was approximately 3 - 4 μm. Although this work is similar to our present work, the growth rate of the SKN composition is much faster and we have successfully grown SKN films as thick as 25 - 30 μm. The quality of our films is excellent, which is considered a major accomplishment in the present work. This opens a new interest for this family and its application not only for SAW devices, but also in other areas such as electro-optics and acousto-optics. As summarized in Table 17, there are a number of other important bronze compositions that possess excellent dielectric, piezoelectric, and optical properties, but these are extremely difficult to grow in the form of bulk single crystals. Since the lattice mismatch between the selected compositions and the substrate materials such

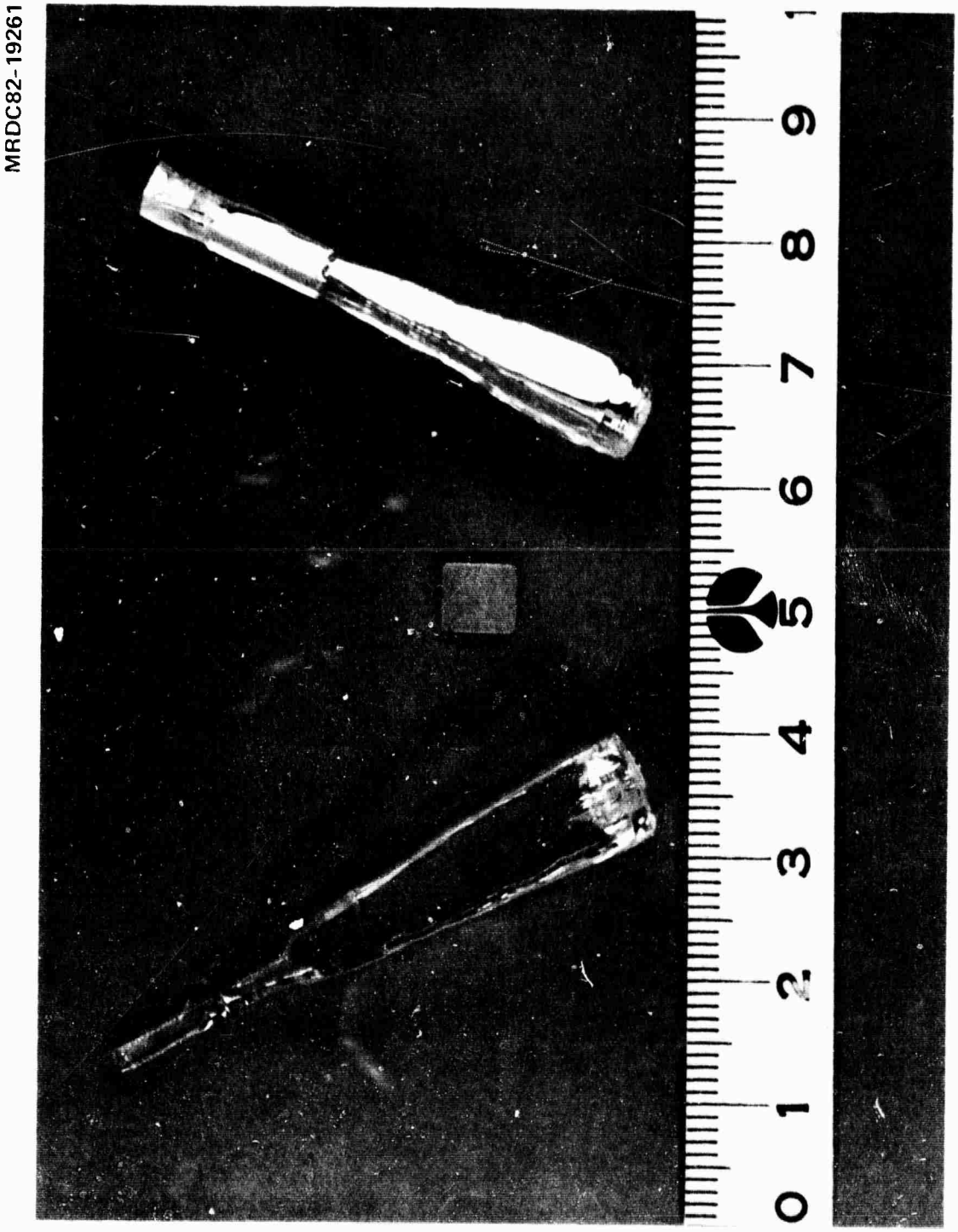

Fig. 26 A typical cross-section of the $Sr_2KNb_5O_{15}$ film on the (001)-cut SBN:60 substrate.

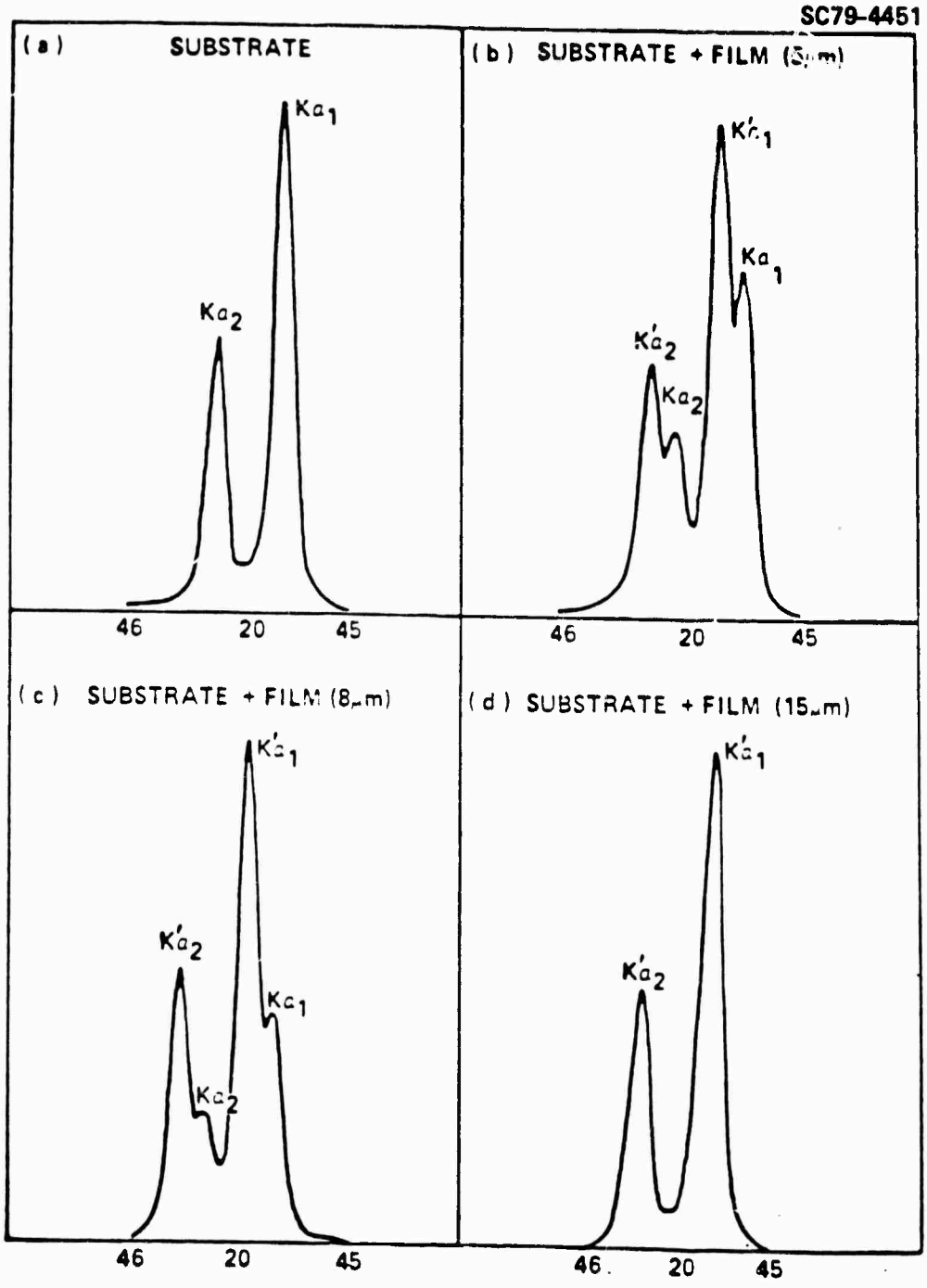

Fig. 27 X-ray diffraction peaks taken for substrate/film.

Table 17

Selected Bronze Compositions for Epitaxial Growth

Composition	Solvent	Melting Temp. (°C)	Supercooling* Range (°C)	Crystallization Range	Lattice Constants a_A	Lattice Constants c_A
$Sr_{1-x}Ba_xNb_2O_6$†	BaV_2O_6	700	40 - 60	Long and useful	12.435 to 12.495	3.923 to 3.975
	SrV_2O_6	740	40	Short and useful		
$Sr_2KNb_5O_{15}$	KVO_3	540	30 - 40	Long and useful	12.473	3.942
$Ba_2Na_3YNb_{10}O_{30}$	BaV_2O_6	700	---	Long and useful	12.440	3.933
$Ba_{2-x}Sr_xK_{1-y}Na_yNb_5O_{15}$	KVO_3	540	---	-----	12.483	3.955
	$NaVO_3$	650	---	-----		
$Ba_2SrTiNb_4O_{15}$	BaV_2O_6	700	---	Long and useful	12.445	3.940
$Ba_2K_{1-y}Na_yNb_5O_{15}$	KVO_3	540	---	-----		
$Pb_{1-x}Ba_xNb_2O_6$	$Pb_2V_2O_{17}$	680	---	Useful	12.472	3.955

*Supercooling range for these systems was established by the DTA technique.
†Lattice constants are given for the tetragonal tungsten bronze solid solution.

as $Sr_{1-x}Ba_xNb_2O_6$, x = 0.50 and 0.60, and $Sr_{0.8}Ba_{1.2}K_{0.75}Na_{0.25}Nb_5O_{15}$, is minimal, it will be possible to continue to develop some of these compositions for a wide variety of applications. The successful growth of good quality LPE layers on SBN substrates is a significant achievement in the present work, and this technological advance will open up new avenues for the development of other tungsten bronze compositions such as those listed in Table 17. Continued work in the future on the epitaxial growth of these compositions will permit tailored material design for specific electro-optic, acousto-optic, non-linear optic and millimeter wave applications, as well as for SAW devices.

6.0 STRUCTURAL AND FERROELECTRIC PROPERTIES OF THE PHASE $Pb_{1-2x}K_xM_x^{3+}Nb_2O_6$, M = La OR Bi

6.1 Introduction

Lead metaniobate, $PbNb_2O_6$, was first studied and reported ferroelectric by Goodman in 1953;[14,15] since then, this material has been the subject of several investigations. Although the Curie temperature was much higher than that of any known ferroelectric, the material did not find immediate application because of the difficulty in preparing good nonporous ceramics and the associated problem of poling them. By analogy with previous work on barium titanate and other ferroelectric hosts, the effect of replacing part of the Pb^{2+} by other divalent and trivalent ions or Nb^{5+} by tetravalent or hexavalent ions was studied, with the objective of improving the sintering and general ferroelectric properties of ceramics.[16-20] It was observed that the Curie temperature decreased, and although this would be a disadvantage, this made it possible to pole the material more effectively and successfully enhance the dielectric and piezoelectric properties.

Since our current interest is in a variety of SAW, electro-optic, and millimeter wave device applications, the search for suitable ferroelectric material having high dielectric and piezoelectric properties is constantly being made. The present work reports the structural, dielectic and piezoelectric properties of the solid solutions based on the $PbNb_2O_6$ phase, i.e., $Pb_{1-2x}K_xM_x^{3+}Nb_2O_6$, where M = La or Bi.

6.2 Experimental Procedure

PbO, K_2CO_3 (Baker Analyzed Grade), Bi_2O_3 (Fisher Scientific Co.), La_2O_3 (American Potach and Chem. Corp.), and Nb_2O_5 (Atomergic Co.) were used as the starting materials. The ceramic specimens were prepared by the conventional technique of milling, prefiring, crushing, pressing and firing. The specimens were prepared in the form of disks 1.3 cm in diameter and 0.3 cm thick. The final sintering was for 2-3 hr, and the temperature, which depended on composition, was between 1250° - 1300°C.

Preparation of pure $PbNb_2O_6$ is complicated by the existence of ferroelectric and nonferroelectric modifications. The transition between these modifications is reversible, although it is accompanied by considerable temperature hysterisis. The high-temperature ferroelectric form was prepared by heating to 1320°C for 30 minutes and then cooling rapidly. X-ray powder diffraction data was obtained with a Norelco diffractometer, using CuK radiation and a graphite monochromator operating at 35 kV and 28 ma. Measurements were made from strip charts produced by scanning 1/4 2θ/min on acetone smear-mounted powders. The measurements are believed to be accurate to ± 0.02 2θ. Instrumental error was corrected through the use of an internal silicon standard. Least-squares analysis of the data for refined cell constants was performed on a Harris Model 1660 computer.

The fired disks were metallized on the major surfaces by using either platinum paste or a vacuum-deposted layer of platinum. Disks required to be poled were heated in silicon oil, and a static field of 20 kV per cm was applied at temperatures as near as possible to 150 to 170°C, the field being maintained while the disks were allowed to cool.

6.3 Crystalline Solubility and Structural Transitions

The work on $K_{0.5}La_{0.5}Nb_2O_6$ by Sobolera et al.[21] and our work on $K_{0.5}Bi_{0.5}Nb_2O_6$ show that these two phases crystallize in the tetragonal crystal symmetry and are isostructural with high temperature tetragonal modification of $PbTa_2O_6$. At room temperature, the ferroelectric $PbTa_2O_6$ phase has an orthorhombic symmetry and is isostructural with the tungsten bronze $PbNb_2O_6$ phase. This suggests that all the systems considered in this work are structurally related and should form a continuous solid solution in the pseudo-binary systems $PbNb_2O_6$-$K_{0.5}La_{0.5}Nb_2O_6$ and $PbNb_2O_6$-$K_{0.5}Bi_{0.5}Nb_2O_6$. The results of x-ray diffraction powder work are in good agreement, and a complete solid solution has been identified in both of the systems. Three structural related phases, namely, the orthorhombic and the tetragonal tungsten bronze type phases and the tetragonal $K_{0.5}La_{0.5}Nb_2O_6$ have been established for the $Pb_{1-2x}K_xM^{3+}_xNb_2O_6$, M = La or Bi, solid solution system. Figure 28 shows x-ray diffraction powder patterns for the three phases.

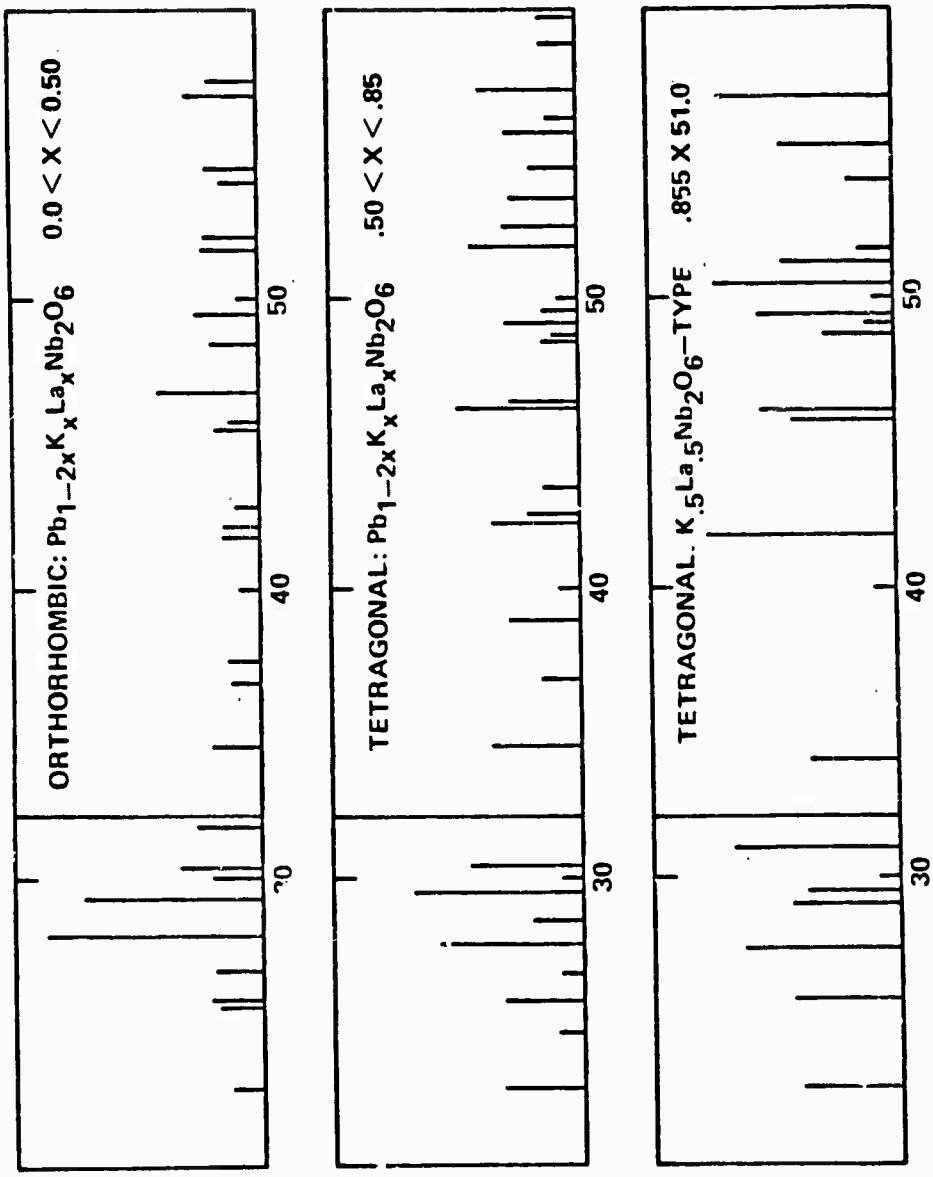

Fig. 28 X-ray diffraction powder patterns for $Pb_{1-2x}K_xM_xNb_2O_6$ solid solution, where M = La or Bi.

The results of x-ray measurements at room temperature show a homogeneity range of the orthorhombic tungsten bronze phase to x = 0.47, while the tetragonal tungsten bronze phase is present in the composition range $0.48 < x < 0.85$. At the other end, the crystalline solid solubility of $PbNb_2O_6$ in the $K_{0.5}M^{3+}_{0.5}Nb_2O_6$ phase is limited and is estimated to be in the composition range $0.86 < x < 1.0$. At composition x = 0.47, both the orthorhombic and tetragonal tungsten bronze phases coexist. This type of morphotropic condition has also been reported on the $Pb_{1-x}Ba_xNb_2O_6$ system. The variation of lattice parameters as a function of composition for the system $Pb_{1-2x}K_xLa_xNb_2O_6$ is shown in Fig. 29. The a and c parameters increased only slightly, while the b parameter decreased considerably with increasing concentration of $K_{0.5}M^{3+}_{0.5}Nb_2O_6$ in the $PbNb_2O_6$ phase. The decrease in the b parameter was substantial compared to the a parameter, so that the ratio b/a becomes close to unity for values $x > 0.50$.

6.4 Ferroelectric Data

The Curie temperature, T_c, is known to be one of the fundamental characteristics of ferro- and antiferroelectrics. This measurement gives the origin of the spontaneous polarized state and is considered important for characterizing piezoelectric materials. In the present work, T_c for the different solid solution systems has been obtained by measuring the dielectric properties as a function of temperature. The technique is relatively simple, and the measurements have been routinely made by using a capacitance bridge (HP 4270A). The test specimens (disks) used for the dielectric measurements are approximately 1.3 cm in diameter and 0.3 cm thick, and are coated on each side with platinum by the standard vacuum evaporation technique.

A typical plot of the dielectric constant vs temperature is given in Fig. 30 for a few compositions on the $Pb_{1-2x}K_xLa_xNb_2O_6$ system. It can be seen that the dielectric constant decreases and broadens whereas the room temperature dielectric constant increases with increasing K^+ and La^{3+} or Bi^{3+} up to x = 0.40. Furthermore, the ferrorelectric phase transition temperature T_c is shifted towards a lower temperature with increasing amounts of $K_{0.5}La_{0.5}Nb_2O_6$ in $PbNb_2O_6$. T_c for the pure $PbNb_2O_6$ has been recorded at 560°C, and this temperature drops with the addition of K^+ and La^{3+} or Bi^{3+} in both the orthorhombic and the

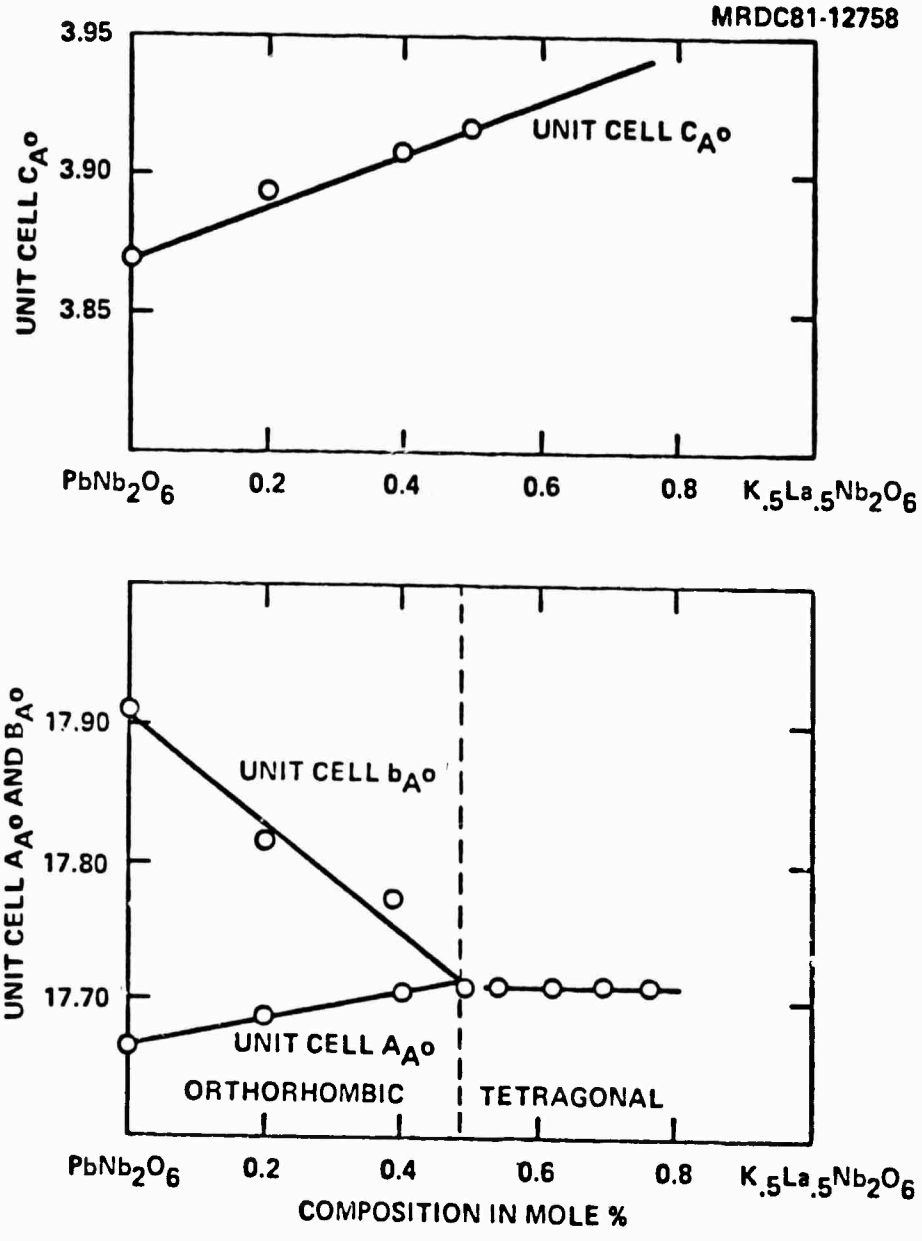

Fig. 29 Variation of lattice parameters for the $Pb_{1-2x}K_xLa_xNb_2O_6$ solid solution.

MRDC82-17598

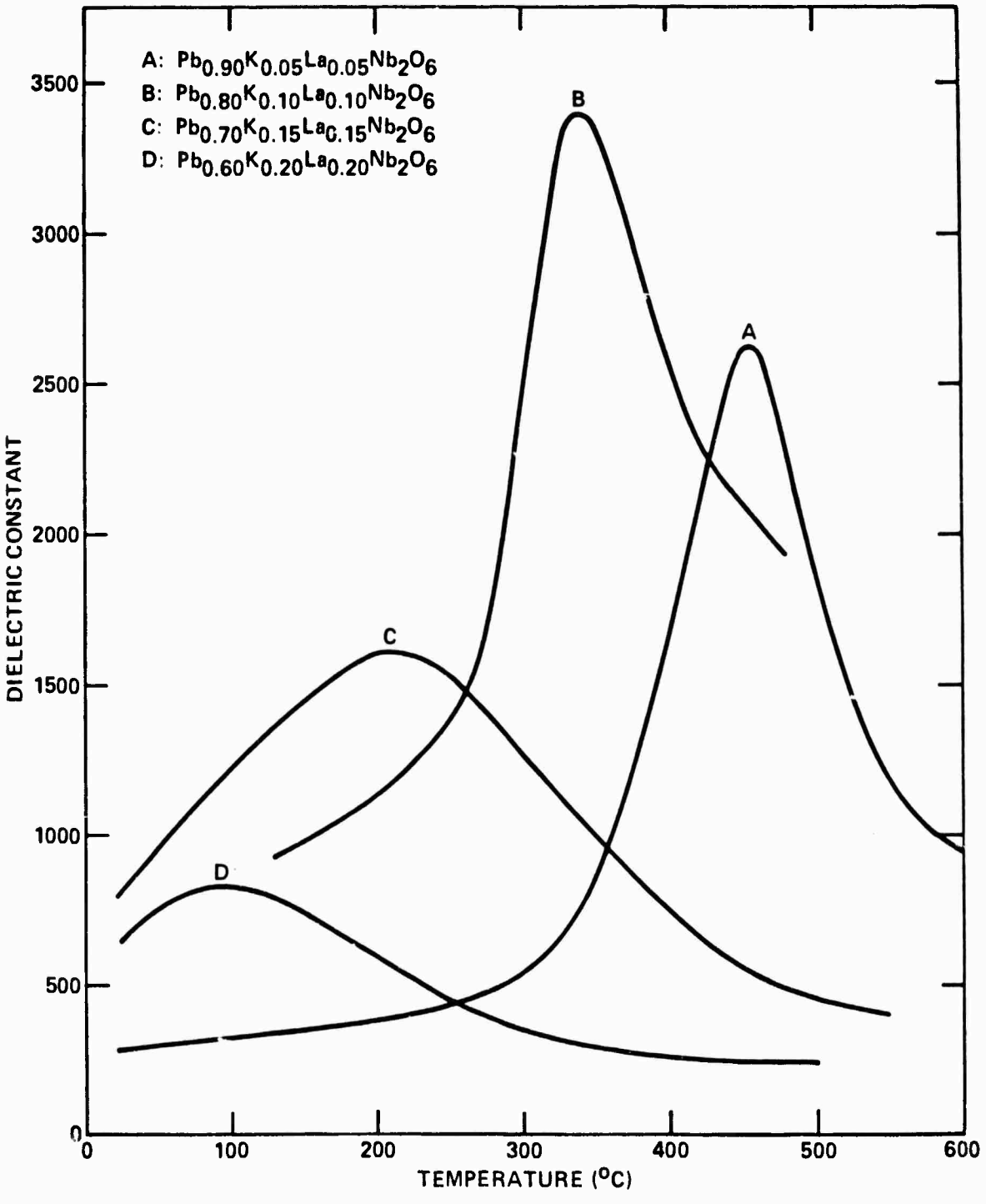

Fig. 30 Dielectric constant vs temperature of $Pb_{1-2x}K_xLa_xNb_2O_6$.

tetragonal tungsten bronze phases. By using this peak position, the transition temperature for each system has been determined. Figure 31 shows the variation of T_c as a function of composition for the $Pb_{1-2x}K_xLa_xNb_2O_6$ and $Pb_{1-2x}K_xBi_xNb_2O_6$ systems. Variation of T_c with composition is linear in both systems and is approximately of the same order. Lowering of T_c has also been reported for several other systems based on $PbNb_2O_6$ solid solutions.

Table 18 summarizes the physical constants for the $Pb_{1-2x}K_xLa_xNb_2O_6$ and $Pb_{1-2x}K_xBi_xNb_2O_6$ systems. As can be seen from this data, the dielectric constant has increased significantly with the addition of K^+ and La^{3+} or Bi^{3+} in the orthorhombic tungsten bronze phase with the compositions $Pb_{0.8}K_{0.1}La_{0.1}Nb_2O_6$ and $Pb_{0.7}K_{0.15}Bi_{0.15}Nb_2O_6$ exhibiting the optimum dielectric constant for each system. The piezoelectric strain coefficient (d_{33}) measurements on various samples were performed using the Berlincourt d_{33}- meter and the results of this study indicate that the composition $Pb_{0.8}K_{0.1}La_{0.1}Nb_2O_6$ again shows the optimum d_{33} coefficient for these systems. We believe these values may increase substantially if the poling is achieved at higher temperatures. In the present case, poling was accomplished in a silicon oil bath at approximately 150°C, which is a very low temperature compared to the respective Curie temperatures. It is anticipated that by improving the poling technique for these ceramic samples it will be possible to better establish the d_{33} coefficient. In any case, the present piezoelectric strain coefficient value obtained for the $Pb_{0.8}K_{0.1}La_{0.1}Nb_2O_6$ sample is much higher than that reported for the $PbNb_2O_6$ crystal, indicating that these compositions can find use for piezoelectric transducer and high frequency dielectric applications.

The effect of a variety of different substituent ions, such as Ba^{2+}, Sr^{2+}, Ca^{2+}, Cd^{2+} and Bi^{3+} for Pb in the $PbNb_2O_6$ phase, has been studied and reported in literature. Except for Ba^{2+}, all other ions are smaller than Pb^{2+},

Table 18

Physical Constants for Modified $PbNb_2O_6$

Composition	Symmetry	Curie Temperature T_c, °C	Dielectric Constant, K R.T.	Dielectric Constant, K T_c	Piezoelectric Strain Coeff., d_{33} c/n
$PbNb_2O_6$	Orthorhombic	560			100×10^{-12}
$Pb_{0.90}K_{0.05}La_{0.05}Nb_2O_6$	Orthorhombic	455	280	2610	----
$Pb_{0.80}K_{0.10}La_{0.10}Nb_2O_6$	Orthorhombic	339	72	3390	130×10^{-12}
$Pb_{0.70}K_{0.15}La_{0.15}Nb_2O_6$	Orthorhombic	201	790	1600	106×10^{-12}
$Pb_{0.60}K_{0.20}La_{0.20}Nb_2O_6$	Orthorhombic	98	650	830	----
$Pb_{0.80}K_{0.10}Bi_{0.10}Nb_2O_6$	Orthorhombic	342	280	2310	30×10^{-12}
$Pb_{0.70}K_{0.15}Bi_{0.15}Nb_2O_6$	Orthorhombic	211	750	2840	35×10^{-12}
$Pb_{0.60}K_{0.20}Bi_{0.20}Nb_2O_6$	Orthorhombic	105	1390	2380	----

and their addition did not alter the orthorhombic crystal symmetry. However, in the case of the $Pb_{1-x}Ba_xNb_2O_6$ solid solution system, the substitution of Ba^{2+} (1.50Å) for Pb^{2+} (1.32Å) first decreases the orthorhombic distortion, and then induces a tetragonal structure with the polar axis along the c rather than along the b axis. Further, the interesting feature in this system is that T_c first decreases in the orthorhombic tungsten bronze phase and then increases in the tetragonal tungsten bronze phase. This is the unique case in the $PbNb_2O_6$ based solid solutions; also, since the average ionic size of $K^+ + La^{3+}$ (1.355Å) and $K^+ + Bi^{3+}$ (1.34Å) is bigger than Pb^{2+}, and since both systems, $Pb_{1-2x}K_xM^{3+}_xNb_2O_6$, M = La or Bi, and $Pb_{1-x}Ba_xNb_2O_6$, are structurally similar, it was expected that the addition of K^+ with La^{3+} or Bi^{3+} would produce similar results, i.e., first a decrease and then an increase in T_c. The results of this investigation (Fig. 31) indicate that a continuously decreasing Curie temperature occurs with increasing amounts of $K^+ + La^{3+}$ or $K^+ + Bi^{3+}$ in both the orthorhombic and tetragonal tungsten bronze phases, indicating that T_c is not only controlled by the size of substituent ions, but its location in the structure is equally important. Since the coordination of Pb^{2+} is 15- and 12-fold in the tungsten bronze structure, there exists three possibilities for each ion in this structure, namely in the 15 or 12, or in both the sites. Neither the work reported in the literature nor the results of this investigation are sufficient to establish the site preference or their distribution over the two crystallographic sites. Further work in this direction is of significant interest in the present study in order to establish the site preference for different ions and their influence over the T_c behavior and the ferroelectric properties.

6.5 Conclusions

Structural data indicate that a complete solid solution exists in the system $PbNb_2O_6$-$K_{0.5}M^{3+}_{0.5}Nb_2O_6$, where M = La or Bi, and three structurally related phases have been reported for these solid solution systems. The addition of K^+ and La^{3+} or Bi^{3+} has enhanced the dielectric and piezoelectric properties for these systems and specifically the compositions, $Pb_{0.9}K_{0.5}La_{0.5}Nb_2O_6$, $Pb_{0.8}K_{0.1}La_{0.1}Nb_2O_6$ and $Pb_{0.7}K_{0.15}La_{0.15}Nb_2O_6$ appear to be of interest for piezoelectric transducer and high frequency dielectric studies. These

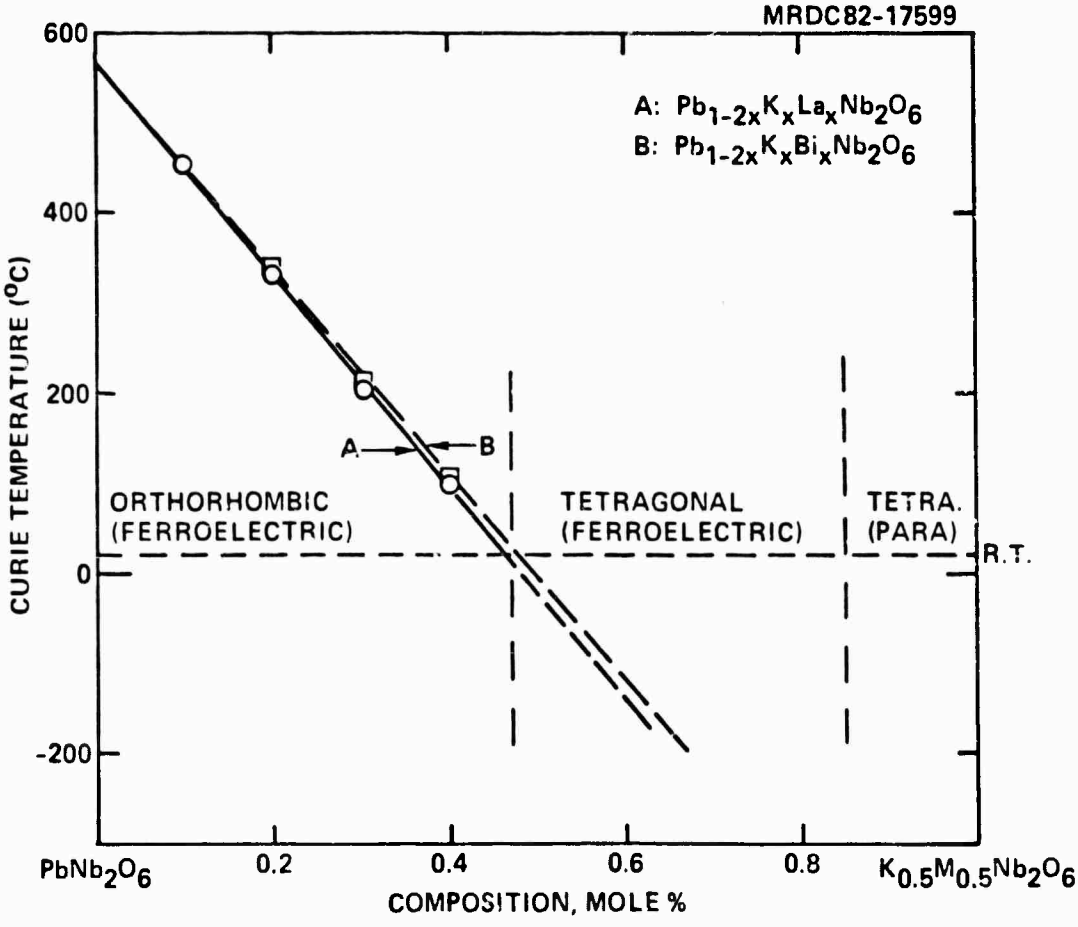

Fig. 31 Variation of ferroelectric transition temperature for $Pb_{1-2x}K_xM_xNb_2O_6$, M = La or Bi.

particular orthorhombic compositions show congruent melting and have very good dielectric and piezoelectric properties. As such, they show great promise for bulk single crystal growth development as well as for future use in ceramic form. Work is currently under way to determine the effects of various processing parameters on the piezoelectric, dielectric, and optical properties of these compositions. These materials are similar in many ways to $Pb_{1-x}Ba_xNb_2O_6$, and are thus expected to be useful in several electro-optic, pyroelectric, millimeter wave, piezoelectric and SAW device applications.

7.0 PHOTOREFRACTIVE PROPERTIES OF SBN SINGLE CRYSTALS

An increasing amount of the research in phase conjugate optics has been directed recently to the study of photorefractive crystals such as $Bi_{12}SiO_{20}$ and more recently, $BaTiO_3$.[22,23] This is due mostly to the fact that these materials hold, at the moment, the best prospect for real-time image processing, such as convolution and correlation, edge enhancement, and image amplification at moderate cw power levels.

Using $BaTiO_3$ with its large mixing efficiency led to the demonstration of phase conjugate reflectivity exceeding unity and continuous wave phase conjugate resonators as well as to new optical oscillator configurations including unidirectional ring oscillators. Until recently, the only photorefractive crystal demonstrated to be efficient enough for use in a high reflectivity phase conjugate mirror was $BaTiO_3$, with samples produced by a single source in the world.

We report here the first use of $Sr_{1-x}Ba_xNb_2O_6$ (SBN) as an efficient photorefractive four-wave mixing medium. We have observed phase conjugate reflectivities exceeding unity in a crystal with $x = 0.4$ and constructed a phase conjugate resonator in which an oscillation beam was seen to build up between the phase conjugate mirror of Fig. 32 and an ordinary plane mirror facing it. The crystal was pumped by an argon laser delivering milliwatts at 476.5 nm. It measured 7 × 5 × 5 mm, and was poled into a single domain so that the c axis was parallel to the 7-mm side.

The early history of SBN, like that of $BaTiO_3$, includes its use as a holographic storage medium.[24] In attempts to optimize the holographic sensitivity of photorefractive crystals in general, and SBN in particular, studies have been made of the effects of applied electric fields and crystal doping.[25] An electric field E_0, parallel to the k vector of the grating modifies the charge carrier transport behavior so as to enhance the recording sensitivity. Crystal doping increases the pool of charge carriers, since the wavelength of the writing beams is generally longer than that of the intrinsic band gap of the

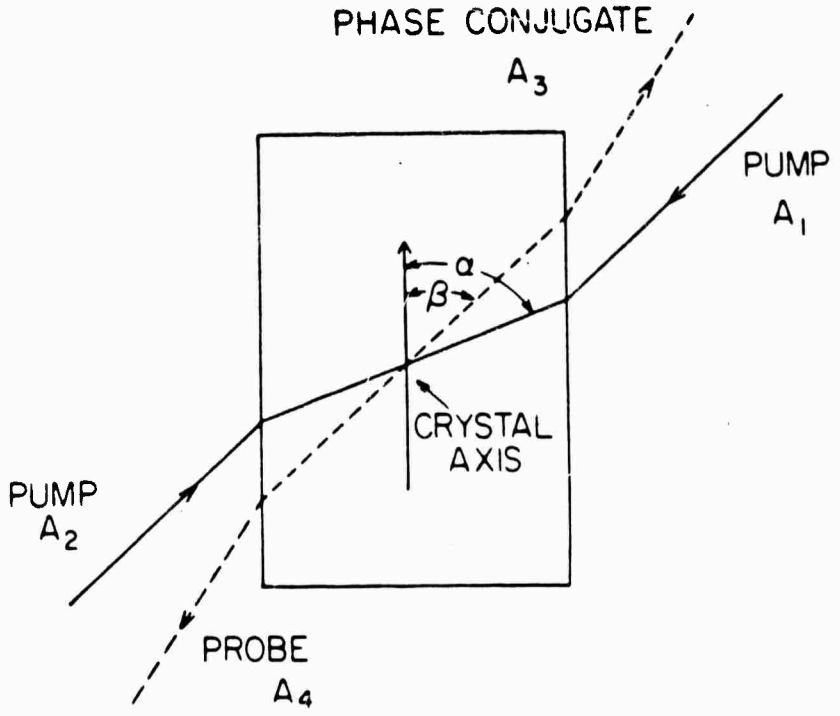

Fig. 32 Four-wave mixing arrangement appropriate to a phase conjugate mirror, showing the pump beams (solid) and probe and phase conjugate beams (dashed), as well as the relative orientation of the c axis of the crystal.

material. By choosing crystals with large electro-optic coefficients, the link between space charge and refractive index grating can be made stronger.

Now it is exactly these refractive index gratings which are responsible for four-wave mixing in photorefractive crystals, and it is with the electro-optic tensor and doping, or impurities, in the crystal in mind that we selected SBN as a likely candidate for efficient four-wave mixing and phase conjugation. A recent work[26] examined the steady-state phase conjugate reflectivity R of a photorefractive phase conjugate mirror (Fig. 32) which, in the undepleted pumps and single grating approximations, is given by

$$R = \left| \frac{\sinh (\gamma \ell/2)}{\cosh \left(\frac{1}{2} \gamma \ell + \frac{1}{2} \ln r\right)} \right|^2 , \tag{27}$$

where ℓ is the length of the crystal (Fig. 32), r is the ratio of the intensities of the two pumping beams, and

$$\gamma = i\omega n e^{i\phi}/2c \cos \theta , \tag{28}$$

where $\theta = 90 - \beta$ is the angle between the probe and the normal to the crystal (Fig. 32) and ϕ is phase shift between the grating and the light interference pattern. The parameter n is proportional to the effective electro-optic coefficient r_{eff}. Since both $BaTiO_3$ and SBN belong to the point group 4 mm, this effective electro-optic coefficient is given by

$$r_{eff} = r_{13} \sin [(\alpha + \beta)/2] , \tag{29}$$

for mixing beams of ordinary polarization and

$$r_{eff} = \left\{ n_e^4 r_{33} \sin \beta \sin \beta + 2 n_e^2 n_o^2 r_{42} \cos^2 \left[\frac{1}{2}(\alpha + \beta)\right] + n_o^4 r_{13} \cos \alpha \cos \beta \right\} \sin \left[\frac{1}{2}(\alpha + \beta)\right] / n_e n_o^3 , \tag{30}$$

for mixing beams of extraordinary polarization, where α and β are the angles of

the pump beams and phase conjugate beams with respect to the c axis of the crystal, as shown in Fig. 32. The r_{ij} are the electro-optic coefficients, and n_o and n_e are the ordinary and extraordinary refractive indices, respectively.

When two beams intersect in a photorefractive crystal, they write an index grating and, in general, this grating couples power from one beam to the other. We performed such an experiment, coupling beams A_2 and A_3 (Fig. 32 when the other two beams are absent). From the theory of this effect we derived a coupling strength comparable with the value which would produce a phase conjugate reflectivity R equal to one; that is $|\gamma\ell| = 1.762$. This is the threshold for a phase conjugate resonator.

Now, in the case of $BaTiO_3$, high phase conjugate reflectivities were obtained by taking advantage of the large electro-optic coefficient $r_{42} \sim 820 \times 10^{-12}$ mV^{-1}. On inspection of expressions (29) and (30) we see that this necessitated first the use of extraordinarily polarized light and second, $(\alpha + \beta)/2$ could not be a multiple of $\pi/2$. That is, the grating wave vector cannot be parallel to any crystal axis. This, together with the high refractive index of $BaTiO_3$ ($n_e = 2.42$), made it necessary to orient (100) cut crystals at large angles with respect to the incident beams. (100) cut crystals are used because during poling, it is necessary to apply an electric field parallel to the c axis. For SBN, however, the largest electro-optic coefficient is r_{33}, which measured $\sim 200 \times 10^{-12}$ mV^{-1} for the sample in which we observed high reflectivity. The grating wave vector could thus be parallel to the c axis, so that the beams could be incident at near-normal angles to the crystal surface. When we demonstrated the phase conjugate resonator we used $\alpha = 83°$ $\beta = 78°$ because of restrictions imposed by optical inhomogeneities (striae) due to stress in the crystal. These inhomogeneities tended to scatter beams travelling in some directions more than others.

We have reported high phase conjugate reflectivities in $Sr_{1-x}Ba_xNb_2O_6$ for $x = 0.4$. However, we feel that even better results will be obtained for lower values of x. As the concentration of barium decreases, the paraferroelectric phase transition temperature drops to $T_c \sim 56°C$ at $x = 0.25$ which represents the lowest stable concentration of barium obtainable in SBN. The

closer the operating temperature is to T_c the larger the electro-optic coefficient becomes, especially for the case where the low-frequency electric field is along the c axis which is the direction of spontaneous polarization. The electro-optic behavior of oxygen-octahedra ferroelectrics is described by the constants g_{ij}. In terms of them, the electro-optic tensor is given by

$$r_{33} = (2g_{11}/\zeta^3)\epsilon_0(\epsilon_c - 1)P_s \quad ,$$

$$r_{13} = (2g_{12}/\zeta^3)\epsilon_0(\epsilon_c - 1)P_s \quad , \qquad (31)$$

$$r_{42} = (g_{44}/\zeta^3)\epsilon_0(\epsilon_a - 1)P_s \quad ,$$

ϵ_c and ϵ_a are the relative dielectric constants of the crystal parallel and perpendicular to the c axis, respectively. P_s is the spontaneous polarization and the g_{ij} are given by 0.17, 0.04, and 0.12 m^4/C^2 for g_{11}, g_{12}, and g_{44}, respectively. ζ is the packing density of the octahedra normalized to that of perovskites. For tungsten bronzes like SBN, it is 1.06. Thus, the r_{ij} increases with the ϵP_s as the phase transition temperature is approached.

In SBN with x = 0.25, the electro-optic coefficient r_{33} is about 1330×10^{-12} mV^{-1} at room temperatures.(5) We tested a crystal of SBN with this barium concentration and failed to obtain high phase conjugate reflectivity, probably because the ionizable charge carrier density was too low. This hypothesis was strengthened when we looked at the absorption in the sample (Table 19). A crystal grown at Rockwell, x = 0.4, did give high phase conjugate reflectivity, in spite of its lower electro-optic coefficient. Its room-temperature half-wave voltage of 300V at wavelength of 632.8 nm indicated an r_{33} of $\sim 200 \times 10^{-12}$ mV^{-1} while the theoretical expression (31) gave $r_{33} \sim 600 \times 10^{-12}$ mV^{-1} based on $P_x = 0.27°C/m^2$(6) and the measured value of $\epsilon_c = 880$. It did, however, absorb more at 476.5 nm than the x = 0.25 sample, as we see in the table. We observed also that neither sample absorbed sufficiently in the red to give high phase conjugate reflectivity at the helium neon laser wavelength at 632.8 nm where our $BaTiO_3$ sample, whose absorption characteristics are given in the table, still excels.

Table 19

Absorption of Several Photorefractive Crystal Samples at Laser Wavelengths

cm^{-1}	$BaTiO_3$	x = 0.4 SBN	x = 0.25 SBN
632.8 nm	0.51 ±0.01	0 ±0.01	0 ±0.01
514.5 nm	1.0 ±0.05	0.16 ±0.04	0 ±0.01
476.5 nm	1.13 ±0.02	0.19 ±0.04	0.04 ±0.04

In conclusion, then, we have demonstrated the photorefractive material SBN in the construction of both a phase conjugate mirror with reflectivity greater than one, and a phase conjugate resonator. We have made some preliminary comparisons of two samples of SBN with differing barium concentrations. More complete studies of the effects of crystal dopants, barium concentration, and operating temperature are in progress.

8.0 PUBLICATIONS AND PRESENTATIONS

8.1 Publications

1. R.R. Neurgaonkar, T.C. Lim, E.J. Staples, and L.E. Cross, "An Exploration of the Limits of Stability of the $LiNbO_3$ Structure Field with A and B Site Cation Substitutions," Ferroelectrics 27-28, 63 (1980).

2. K.L. Keester, R.R. Neurgaonkar, T.C. Lim, and E.J. Staples, "Strontium Metaniobates: Its Crystallogrphy, Polimorphism and Isomorphism," Mat. Res. Bul. 15, 821 (1980).

3. R.R. Neurgaonkar, M.H. Kalisher, T.C. Lim, E.J. Staples, and K.L. Keester, "Czochralski Single Crystal Growth of $Sr_{0.61}Ba_{0.39}Nb_2O_6$ for Surface Acoustic Wave Devices," Mat. Res. Bull. 15, 1235 (1980).

4. L.E. Cross, R. Betch, H. McKinstry, T. Shrout, and R.R. Neurgaonkar, "A New Method for Predicting the Temperature Dependence of Elastic Compliance in Simple Proper Ferroelectrics," Proceedings of Frequency Control Symposium, 25-33 (1980).

5. R.R. Neurgaonkar and W.K. Cory, "Structural and Dielectric Properties of $Ba_6Ti_2Nb_8O_{30}$-Type Tungsten Bronze Compositions," (in preparation).

6. R.R. Neurgaonkar, T.C. Lim, E.J. Staples, and L.E. Cross, "Crystal Chemistry of Ferroelectric Materials for SAW Devices," Proceedings of Ultrasonics, 410 (1980).

7. T.R. Shrout, L.E. Cross, P. Moses, H.A. McKinstry and R.R. Neurgaonkar, "A Phenomenological Theory for Predicting the Temperature Dependence of Elastic, Dielectric and Piezoelectric Properties in Simple Proper Ferroelectric Crystals," Proceedings of Ultrasonics, 414 (1980).

8. R.R. Neurgaonkar, W.K. Cory, W.W. Ho, W.F. Hall and L.E. Cross, "Tungsten Bronze Family Crystals for Acoustical and Dielectric Applications," Ferroelectrics 38, 857 (1981).

9. E.J. Staples and R.R. Neurgaonkar, "SAW Transduction and Poling in Ferroelectric Strontium Barium Niobate," Ferroelectrics 38, 882 (1981).

10. T.R. Shrout, L.E. Cross, P. Moses, H.A. McKinstry and R.R. Neurgaonkar, "Higher Order Electrostriction in Ferroelectric Tungsten Bronzes," Ferroelectrics 38, 881 (1981).

11. W. Ho, W.F. Hall, R.R. Neurgaonkar, R.E. DeWames, and T.C. Lim, "Microwave Dielectric Properties of $Sr_{0.61}Ba_{0.39}Nb_2O_6$ Single Crystals," Ferroelectrics 38, 833 (1981).

12. R.R. Neurgaonkar, J.R. Oliver, W.K. Cory and L.E. Cross, "Structural and Ferroelectric Properties of the Phase $Pb_{1-2x}K_xM^{3+}_xNb_2O_6$, M = La or Bi," to be submitted to Mat. Res. Bull.

8.2 Presentations

1. R.R. Neurgaonkar, T.C. Lim, E.J. Staples and L.E. Cross, "An Exploration of the Limits of Stability of the $LiNbO_3$ Structural Field with A and B Site Cation Substitutions," presented at the IEEE Int. Symposium on Ferroelectrics, Minneapolis, MN, June 13-15, 1979.

2. K.L. Keester, R.R. Neurgaonkar, T.C. Lim, and E.J. Staples, "Conoscopic Characterization of Czochralski Grown Strontium-Barium Niobate Boules," presented at the 4th Conference on Crystal Growth, Stanford Sierra Camp, Fallen Leaf, California, May 16-18, 1979.

3. L.E. Cross, R. Betch, H. McKinstry, T. Shrout and R.R. Neurgaonkar, "A New Method for Predicting the Temperature Dependence of Elastic Compliance in Simple Proper Ferroelectrics," presented at the 34th Annual Symposium on Frequency Control, Philadelphia, PA, May 28-30, 1980.

4. R.R. Neurgaonkar, T.C. Lim, E.J. Staples, and L.E. Cross, "Crystal Chemistry of Ferroelectric Materials for SAW Devices," presented at the Annual Ultrasonic Symposium, Boston, MA, Nov. 1980.

5. T.R. Shrout, L.E. Cross, P. Moses, H.A. McKinstry and R.R. Neurgaonkar, "A Phenomenological Theory for Predicting the Temperature Dependence of Elastic, Dielectric and Piezoelectric Properties in Simple Proper Ferroelectric Crystals," Presented at the Annual Ultrasonic Symposium, Boston, MA, Nov. 1980.

6. R.R. Neurgaonkar, W.K. Cory, W.W. Ho, W.F. Hall, and L.E. Cross, "Tungsten Bronze Family Crystals for Acoustical and Dielectric Applications," presented at the 5th International Meeting on Ferroelectricity, State College, PA, August 17-21, 1981.

7. R.R. Neurgaonkar, W.K. Cory, T.C. Lim, and L.E. Cross, "Solid Solution Based on Ferroelectric $Pb_{1-2x}K_xLa_xNb_2O_6$," Presented at the 83rd Annual Conference of the American Ceramic Society, Washington, D.C., May 4-6, 1981.

8. E.J. Staples and R.R. Neurgaonkar, "SAW Transduction and Poling in Ferroelectric Strontium Barium Niobate," presented at the 5th International Meeting on Ferroelectricity, State College, PA, August 17-21, 1981.

9. T.R. Shrout, L.E. Cross, P. Moses, H.A. McKinstry, and R.R. Neurgaonkar, "Higher Order Electrostriction in Ferroelectric Tungsten Bronzes," presented at the 5th International Meeting on Ferroelectricity, State College, PA, August 17-21, 1981.

9.0 REFERENCES

1. R.R. Neurgaonkar, M.H. Kalisher, T.C. Lim, E.J. Staples, and K.L. Keester, Mat. Res. Bull. 15, 1235 (1980).

2. R.R. Neurgaonkar, W.K. Corly, W.W. Ho, W.F. Hall and L.E. Cross, Ferroelectrics 38, 857 (1981).

3. E.J. Staples and R.R. Neurgaonkar, Ferroelectrics 38, 882 (1981).

4. W.W. Ho, W.F. Hall, R.R. Neurgaonkar, R.E. DeWames, and T.L. Lim, Ferroelectrics 38, 833 (1981).

5. P.L. Lenzo, E.G. Spencer, and A.A. Ballman, Appl. Phys. Lett. 11, 23 (1967).

6. A.M. Glass, J. Appl. Phys. 40, 4699 (1969).

7. K. Megumi, N. Nagatsuma, Y. Kashiwasda, and Y. Furuhata, J. Mat. Sci. 11, 1583 (1976).

8. N. Uchica and Niizeki, Proc. IEEE 61, 1073 (1973).

9. P.H. Carr, Proc. of Ultrasonics Symposium, 286 (1974).

10. R. Whatmore, J. Crys. Growth 48, 530 (1980).

11. T. Yamada, J. Appl. Phys. 41, 4141 (1970).

12. M. Adachi and A. Kawabata, Jap. J. Appl. Phys. 17, 1969 (1978).

13. A.A. Ballman and H. Brown, J. Crdys. Growth 1, 311 (1967).

14. G. Goodman, Am. Ceram. Bull. 31, 113 (1952).

15. G. Goodman, J. Am. Ceram. Soc. 36, 368 (1953).

16. R.V. Coates and H.F. Kay, Phil. Mag. 8, 1449 (1958).

17. E.C. Subbarao, J. Am. Ceram. Soc. 44, 92 (1961).

18. E.C. Subbarao and J. Hrizo, J. Am. Ceram. Soc. 45, 528 (1962).

19. P. Baxter and N.J. Hellicar, J. Am. Ceram. Soc. 43, 578 (1960).

20. M.H. Francombe and B. Lewis, Acta Cryst. 11, 696 (1958).

21. L.V. Soboleva and F.I. Dmitrieva, Inorg. Mat. 6, 1761 (1970).

22. J. Feinberg and R.W. Hellworth, Opt. Lett. 5, 519 (1980).

23. J.O. White, M. Cronin-Golomb, B. Fischer and A. Yariv, Appl. Phys. Lett. 40, 450 (1982).

24. J.B. Thaxter and M. Kestigian, Appl. Opt. 13, 913 (1974).

25. K. Megumi, H. Kozuka, M. Kobayashi, and Y. Furuhata, Appl. Phys. Lett. 30, 631 (1977).

26. B. Fischer, M. Cronin-Golomb, J.O. White, and A. Yariv, Opt. Lett. 6, 519 (1981).